

Публікуються результати експериментальних і теоретичних досліджень у галузях фізичної електроніки, фізики плазми, фізики поверхні твердого тіла, емісійної електроніки, криогенної та мікроелектроніки, нанофізики та наноелектроніки, високотемпературної надпровідності, квантової радіофізики, функціональної електроніки, твердотільної електроніки, мобільного зв'язку, медичної радіофізики, методів отримання діагностичної інформації та її комп'ютерної обробки.

Для науковців, викладачів вищої школи, студентів.

Experimental and theoretical contributions are published in the following fields: physical electronics, plasma physics, solid-state surface physics, emission electronics, cryogenic electronics, microelectronics, nanophysics and nanoelectronics, high-temperature superconductive electronics, solid-state electronics, functional electronics, microwave electronics, quantum electronics, mobile communication, medical radio-physics, methods of receipt and computer processing of diagnosis information.

Designed for researches, university teachers, students.

ВІДПОВІДАЛЬНИЙ РЕДАКТОР	І.О.Анісімов, д-р фіз.-мат. наук, проф.
РЕДАКЦІЙНА КОЛЕГІЯ	С.М.Левитський, д-р фіз.-мат наук, проф. (заст. відп. ред.); В.І.Григорук, д-р фіз.-мат наук, проф. (наук. ред.); Т.В.Родіонова, канд. фіз.-мат. наук, ст. наук. співроб. (відп. секр.); Ю.В.Бойко, канд. фіз.-мат. наук, доц.; В.І.Висоцький, д-р фіз.-мат. наук, проф.; В.В.Данилов, д-р фіз.-мат. наук, проф.; В.В.Ільченко, д-р фіз.-мат. наук, проф.; В.І.Кисленко, канд. фіз.-мат. наук, доц.; В.Ф.Коваленко, д-р фіз.-мат. наук, проф.; І.П.Коваль, канд. фіз.-мат. наук, доц.; М.В.Кононов, канд. фіз.-мат. наук, доц.; В.Г.Литовченко, д-р фіз.-мат. наук, проф.; Г.А.Мелков, д-р фіз.-мат. наук, проф.; В.А. Скришевський, д-р фіз.-мат. наук, проф.
Адреса редколегії	03127, м. Київ-127, просп. акад. Глушкова, 2, корп. 5, радіофізичний факультет, ☎ 526 05 60
Затверджено	Вченою радою радіофізичного факультету 12 жовтня 2009 року (протокол № 3)
Атестовано	Вищою атестаційною комісією України. Постанова Президії ВАК України № 3-05/11 від 15.12.04
Зареєстровано	Зареєстровано Міністерством юстиції України. Свідоцтво про державну реєстрацію серія КВ № 15797-4269Р від 02.10.09
Засновник та видавець	Київський національний університет імені Тараса Шевченка, Видавничо-поліграфічний центр "Київський університет". Свідоцтво внесено до Державного реєстру ДК № 1103 від 31.10.02
Адреса видавця	01601, Київ-601, 6-р Т.Шевченка, 14, кімн. 43 ☎ (38044) 239 31 72, 239 32 22; факс 239 31 28

ЗМІСТ

Анісімов І., Соловійова М. Еволюція модульованого електронного пучка в неоднорідному плазмовому бар'єрі для різних густин струму пучка: одновимірне моделювання	4
Бех І., Вербицька О., Ільченко В., Лушкін О., Нагула П., В. Щербан В. Вплив електричного поля на емісійні властивості Sc-Ba металевопористих емітерів з W матрицею	7
Борзаниця Д., Лушкін О. Вплив електричного поля на склад поверхні електронегативного z-зрізу кристалу ніобату літію	9
Вакалюк О., Гребень К., Каленюк О., Пан В., Прокопенко О. Методика визначення нелінійного імпедансу плівок високотемпературних надпровідників за допомогою комбінованого мікросмужкового резонатора	12
Великанець Д., Анісімов І., Літошенко Т. Вплив нагрівної нелінійності на деформацію профілю концентрації в неоднорідних плазмово-пучкових системах	19
Голобородько А. Модель матеріалу з від'ємним показником заломлення	21
Голобородько Н., Поданчук Д., Данько В., Голобородько А., Котов М. Сканер хвильового фронту для детектування неоднорідностей поверхні	24
Горячко А., Коваленко А., Курашов В., Щирба А. Експериментальне дослідження поверхневої шорсткості безоболонкових оптичних волокон	28
Григорук В., Сидоренко В., Мельник Б. Ближньопольова резонансна синхронізація диполів	31
Дудко А., Лушкін О. Вплив температури на емісійну здатність скандат-барієвих МПЕ з вольфрамовою матрицею	34
Духлій А., Ільченко В., Телега В., Кравченко О., Затишний Д. Дослідження елементного складу плівок SnO ₂ легованих Pt гетероструктури SnO ₂ /Si	37
Ісаєнко О., Іванісік А. Модифікація методу динамічного розсіяння світла для вимірювання розмірів наночастинок	39
Клешич М., Борецький В., Веклич А. Система керування монохроматорами МДР 12/23	41
Кнуренко А., Мартиш Е. Порівняльний аналіз процесів в планетарних магнітосферах	46
Кобеляцький В., Мелков Г., Мойсєєнко В., Прокопенко О. Кореляційний приймач з оберненням хвильового фронту магнітостатичних хвиль	49
Кравченко О., Марущак І. Двовимірне моделювання пилового згустку в приелектродному шарі	52
Кравченко О., П'янкова О. Моделювання формування уніполярної дуги в приелектродному шарі між плазмою та ізолюваною стінкою	54
Лушкін О., Щербан В., Тесленко С. Розробка блоку спряження для автоматизації оже-спектрометра 0910С-3	57
Маслюк Л., Мацішин М., Петричук М., Коваленко В. Особливості взаємодії магнітних наночастинок на малих відстанях	60

CONTENTS

Anisimov I., Soloviova M. Evolution of the modulated electron beam in the inhomogeneous plasma barrier for various beam current densities: 1d simulation	4
Bekh I., Verbytska O., Il'chenko V., Lushkin A., P. Nagula P., Shcherban V. The influence of the electric field on the emissions properties of the Sc-Ba dispensed emitters with the W matrix	7
Borzanytsya D., Lushkin O. The influence of an electric field on composition of a surface of a negatively poled z-cut of lithium niobate.....	9
Vakaliuk A., Greben K., Kalenyuk A., Pan V., Prokopenko O. Method of high-temperature superconductor film nonlinear impedance determination using combined microstrip resonator.....	12
Velykanets' D., Anisimov I., Litoshenko T. Influence of the heating non-linearity on the plasma density profile deformation in the inhomogeneous beam-plasma systems	19
Goloborodko A. The model of the material with negative refraction index.....	21
Goloborodko N., Podanchuk D., Dan'ko V., Goloborodko A., Kotov M. Wavefront scanner for detecting surface inhomogeneities	24
Goriachko A., Kovalenko A., Kurashov V., Shchyrba A. Experimental investigations of intrinsic roughness at the surface of air-clad optical fibers	28
Grygoruk V., Sidorenko V., Melnik B. Near-field resonance synchronization of dipoles	31
Dudko A., Lushkin O. The temperature influence on the emission properties of the Sc-Ba dispensed emitters with the W matrix	34
Duhliy A., Il'chenko V., Telega V., Kravchenko A., Zatishniy D. Investigation of the elemental structure of SnO ₂ films doped with Pt heterostructure SnO ₂ /Si.....	37
Isaienko O., Ivanisik A. Modification of the dynamic light scattering for nanoparticles size measurement.....	39
Kleshich M., Boretskij V., Veklich A. Control system of monochromators MDR 12/23	41
Knurenko A., Martysh E. Comparison of planetary magnetospheres	46
Kobeliatskyi V., Melkov G., Moiseienko V., Prokopenko O. Correlation Receiver with Wave Front Reversal of Magnetostatic Waves	49
Kravchenko O., Marushchak I. Two-dimensional simulation of dust clouds in the electrostatic sheath	52
Kravchenko O., Pyankova O. Simulation of unipolar arc formation in sheath between plasma and isolated walls.....	54
Lushkin O., Shcherban V., Teslenko S. Development of an automated measuring unit for auger spectrometer 09IOS-3.....	57
Masluk L., Matsishin M., Petrychuk M., Kovalenko V. Features of magnetic nanoparticles interaction on small distances	60

**EVOLUTION OF THE MODULATED ELECTRON BEAM
IN THE INHOMOGENEOUS PLASMA BARRIER
FOR VARIOUS BEAM CURRENT DENSITIES: 1D SIMULATION**

Evolution of the non-relativistic modulated electron beam moving through the inhomogeneous plasma barrier was studied via computer simulation using PIC method. Dynamics of the modulated electron beam in barrier was analyzed depending on beam-plasma instability increment determined by electron beam current density. Results are discussed in the context of the experimental works in this field.

Key words: Inhomogeneous plasma, modulated electron beam, computer simulation, beam-plasma instability.

Методом комп'ютерного моделювання досліджено еволюцію нерелятивістського модульованого електронного пучка, що рухається крізь бар'єр неоднорідної плазми. Динаміку модульованого електронного пучка в бар'єрі було проаналізовано в залежності від інкременту плазмово-пучкової нестійкості, що визначається густиною електронного пучка. Отримані результати обговорюються у контексті експериментальних робіт в цій області.

Ключові слова: неоднорідна плазма, модульований електронний пучок, комп'ютерне моделювання, плазмово-пучкова нестійкість.

Introduction. Beam-plasma interaction has been studied during several decades (see, e.g., [14, 15]). In the last works devoted to this problem computer simulation is widely used along with laboratory experiments. But in the most cases non-modulated electron beams are treated. At the same time modulated beam's evolution in plasma is important for such problems as electron beams' using as emitters of electromagnetic waves in ionosphere [1, 16, 19, 20], transillumination of the dense plasma barriers for electromagnetic waves using electron beams [2, 3, 7, 18], inhomogeneous plasma diagnostics via transition radiation of electron beams and electron bunches [8, 9] etc.

Evolution of the modulated electron beam in supercritical plasma barrier was studied experimentally in [3, 7, 18]. It was demonstrated that signal at the modulation frequency reached its maximum inside the barrier, and magnitude of this maximum was directly proportional to the initial beam modulation depth. These results were explained in [4] by the concurrence between non-resonant (signal) and resonant (noise) modes of the beam-plasma system. But calculations presented in [4] correspond to the initial problem, and results of experiments [3, 7, 18] correspond to the initial-boundary problem. As a result it was impossible to compare experiments and simulation.

In our previous work [6] evolution of the modulated electron beam in plasma for the initial-boundary problem was studied via computer simulation using PIC method [10, 13]. But homogeneous plasma barrier in [6] doesn't correspond to the experimental one that is close to Gaussian shape [3, 7, 18]. Dynamics of the modulated electron beam in such a barrier was studied in [11, 12] for the conditions of the experiment [3, 7, 18]. It was found earlier [5] that behavior of signal at the resonant frequency and at the modulation frequency depended significantly on the value of electron beam current density. So, this article is devoted to study of dynamics of the modulated electron beam moving through inhomogeneous plasma barrier (with the Gaussian profile of plasma density) dependent on the value of electron beam current density. Initial-boundary problem is solved.

Model description and simulation parameters.

Warm isotropic collisionless plasma with initial inhomogeneous density profile is studied. Simulation was carried out via PIC method using modified program package PDP1 [10, 13]. Since this package uses electrostatic simulation, non-relativistic electron beams were studied.

1D region between two electrodes is simulated. Inter-electrode space is filled with fully ionized hydrogen plasma. Initial plasma density profile is obtained by the approximation of experimental axial plasma density profile [3, 7, 18]

by the Gaussian function. So initial electron and ion plasma density is set as

$$n(x) = n_0 + n_m \exp \left[- \left(\frac{x - x_0}{2\Delta} \right)^2 \right], \quad (1)$$

where n_0 is the plasma density for $x \rightarrow \pm\infty$, $n_0 + n_m$ is the peak plasma density inside the barrier at $x = x_0$, and Δ is a half-width of the plasma barrier. Other simulation parameters are presented in table 1.

Table 1. Simulation parameters

n_0	$5.5 \cdot 10^{10} \text{ cm}^{-3}$
n_m	$2.04 \cdot 10^{11} \text{ cm}^{-3}$
x_0	10 cm
Δ	3.87 cm
Simulation region length	20 cm
Plasma electrons thermal velocity	$6 \cdot 10^7 \text{ cm/s}$
Plasma ions thermal velocity	$2,33 \cdot 10^6 \text{ cm/s}$
Beam electrons velocity	$2 \cdot 10^9 \text{ cm/s}$
Electron beam modulation frequency	2.77 GHz
Electron beam modulation depth	0.01 – 0.3
Simulation time step	10^{-13} s
Electron beam current density	50, 200, 600, 2000, 6000 A/m ²

Electron beam is injected into plasma barrier from the left electrode. It moves to the right one. Electrodes absorb both plasma and beam particles. Initially electron beam is density-modulated:

$$\rho(t) = \rho_0(1 + m \cos \omega t), \quad (2)$$

where m is the modulation depth.

Modulation frequency was selected in the range

$$\omega_p(n_0) < \omega < \omega_p(n_0 + n_m), \quad (3)$$

where $\omega_p(n) = (4\pi n e^2 / m)^{1/2}$ – electron plasma frequency.

Two local plasma resonance regions are located inside the barrier at the modulation frequency.

Simulation was carried out during the time interval of approximately 200 electron plasma periods or 5 ion plasma periods. During this time electron beam reached the opposite electrode, and quasi-stationary regime was settled.

Since it's rather difficult to divide different turbulence modes in the inhomogeneous plasma barrier [5], modes dependent on the beam-plasma instability increment were analysed. This increment is defined by electron beam current density (for the fixed beam velocity). Such electron beam current densities were selected for exploration: 50 A/m², 200 A/m², 600 A/m², 2000 A/m² and 6000 A/m².

Simulation results. For the beam current density 50 A/m² beam-plasma instability doesn't reach the non-linear stage on the simulation interval. This result can be explained by the influence of plasma inhomogeneity on the beam-plasma interaction. This mode can be conventionally referred as the small increments' mode.

For beam current densities 200 A/m² and 600 A/m² the signal magnitude at the modulation frequency reaches its maximum inside the barrier. At the same time influence of the plasma inhomogeneity on the dynamics of modulated beam remains considerable. So this mode can be referred as the moderate increments' mode.

At last, for the beam current densities 2000 A/m² and 6000 A/m², the influence of plasma inhomogeneity on the beam dynamics becomes negligible due to essential growth of beam-plasma instability increment. This mode can be referred as the large increments' mode.

Let's consider simulation results for these modes.

Small increments' mode. For this mode parameters fulfil a condition

$$\gamma L \leq a, \quad (4)$$

where γ is the average spatial instability increment, L is simulation region length, and parameter $a = \ln(A_{\max} / A_{\min})$ has a value of several units.

Hydrodynamic increment for the simulation parameters

$$\gamma_H = \frac{\sqrt{3}}{2^{4/3}} \omega_p \left(\frac{n_B \cdot v_0}{n \cdot v_g} \right)^{1/3} \quad (5)$$

has a value 1.75 cm⁻¹, simulation region length is equal to 20 cm (see table 1). That's why condition (4) isn't fulfilled even for the homogeneous plasma barrier. But maximal increment obtained from the spectrum (fig. 1) is about 0.1 cm⁻¹. Such value is much less than obtained from (5). Maximal increment, calculated from spectrum, meets the condition (4). Such difference between increments obtained from simulation results and calculated from equation (5) can be explained by plasma inhomogeneity influence.

Condition of strong influence of plasma inhomogeneity on the beam-plasma instability is

$$\gamma \Delta x \leq a, \quad (6)$$

where Δx is characteristic inhomogeneity length of the plasma density profile. This influence causes to violation of the synchronism between electron beam and the beam excited wave on the distance less or close to instability development length [20]. As a result, the instability increment decreases essentially. Minimal inhomogeneity length is about $\Delta x = 4 \text{ cm}$. Consequently condition (6) is fulfilled both for increments calculated from (5) and obtained from the simulation results.

Moderate increments' mode. For the moderate increments' mode beam-plasma instability develops and reaches the non-linear stage in the simulation region. In this case the condition reverse to (4) is fulfilled. Maximal increment obtained from the spectrum is about 0.28 cm⁻¹. Although this value is much less than calculated from hydrodynamics us-

ing equation (5), i.e. 2.9 cm⁻¹, but still it doesn't fulfill inequality (4) as it was for the previous mode. Since condition (6) isn't fulfilled, plasma inhomogeneity still has strong influence on the instability. That's why so considerable difference between two values of the increment is observed. Similar situation takes place for the beam current density 600 A/m². The increment obtained from the spectrum is 0.63 cm⁻¹, and the value calculated from (5) is 4 cm⁻¹.

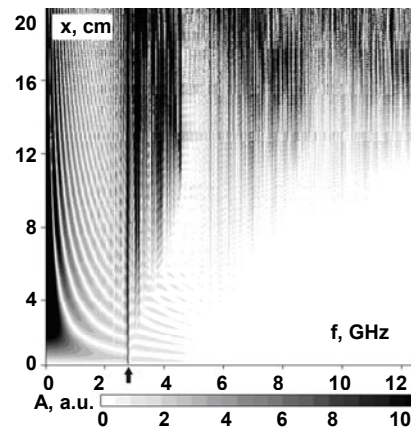


Fig. 1. Spatial evolution of spectrum of the electron beam density. Arrow marks the initial modulation frequency. Beam current density $j=50 \text{ A/m}^2$, initial modulation depth $m=0.05$

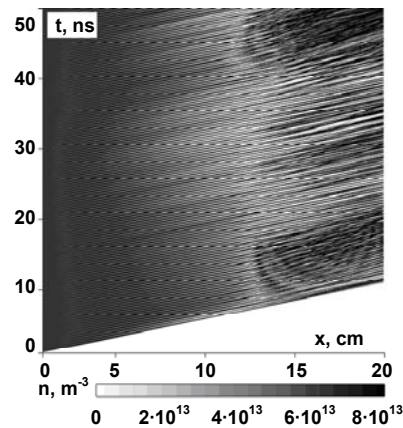


Fig. 2. Space-time distribution of the electron beam density. Beam current density $j=200 \text{ A/m}^2$, initial modulation depth $m=0.05$

At the space-time distribution of electron beam density perturbations (fig. 2) one can see that modulation depth increases during the beam propagation inside the barrier (strip contrast becomes more noticeable). Just after the barrier centre (10-12 cm from injector) the beam's over-modulation takes place (new strips appear between the previous ones, so the temporal period changes).

Space-time distributions of electric field strength (a) and deformation of the ion concentration profile (b) are plotted on fig. 3 for the beam current density $j=200 \text{ A/m}^2$ and initial modulation depth $m=0.05$.

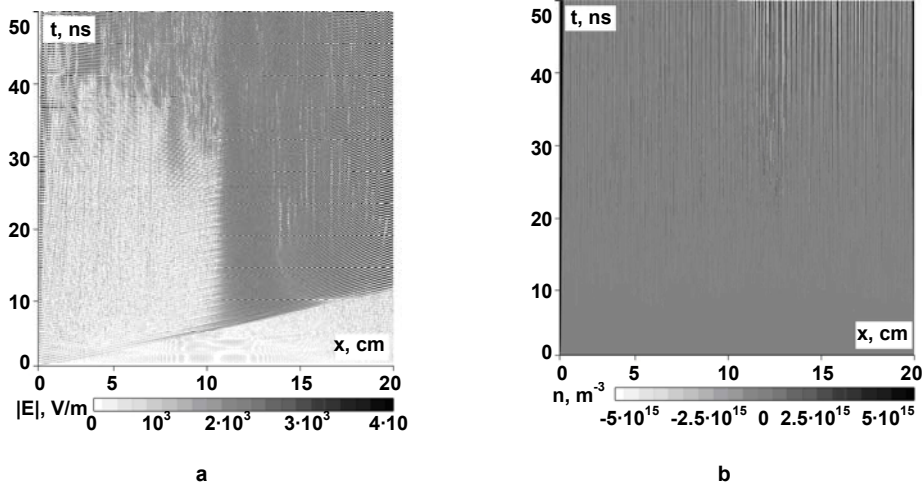


Fig. 3. Space-time distribution of electric field strength (a) deformation of the ion concentration profile (b). Beam current density $j=200 \text{ A/m}^2$, initial modulation depth $m=0.05$

Temporal period's change just after the barrier centre is also observed on the space-time distribution of electric field (fig. 3 a). One can see that parallel lines with the initial period corresponding to modulation frequency bend to the top on both images (fig. 2, fig.3 a). Some separate lines on fig.2 bend more than others. These lines correspond to the formation of slow electron bunches.

On the right part of fig. 2 one can see the set of bright lines that are non-parallel to initial direction. Some part of electrons slows down, and some part is accelerated. So the focusing of electron bunches occurs.

Considerable density perturbations are visible on the space-time distribution of ion density (fig. 3 b). This effect is connected with the large beam current density. Thus high-frequency electric field magnitudes excited by the beam are large as well.

Increment of ion perturbations, calculated from fig. 3 b, is about $2 \cdot 10^8 \text{ s}^{-1}$.

At the same time theoretically calculated increment of the modulation instability [17]

$$\gamma_{Md}(W) = \omega_{pe} \left(\frac{W}{3nT_e} \right)^{1/2} = \omega_{pi} \sqrt{\frac{W}{3nT_e}} \quad (7)$$

is equal to $6 \cdot 10^8 \text{ s}^{-1}$.

These values are of the same order, so modulation instability development can be postulated. That's why the current mode can be compared with the strong turbulence mode for homogeneous barrier [5].

Large increments' mode. In the large increments' mode beam-plasma instability at the simulation region reaches the non-linear stage earlier than in previous case. As well as for the moderate increments' mode, condition (4) is not fulfilled: maximal increment, obtained from spectrum, is about 5 cm^{-1} . Condition (6) isn't fulfilled as well, so the plasma inhomogeneity influence becomes insignificant. This conclusion can be confirmed by the equality of increments calculated theoretically from (5) – 5.9 cm^{-1} , and obtained from spectrum.

For large beam current density (2000 A/m^2) the maximal signal magnitude is reached before barrier centre. For the beam current density of 6000 A/m^2 maximum of electric field amplitude is located just near the injector. In that case the barrier inhomogeneity doesn't affect on the modulated beam evolution. So the signal amplitude restriction is caused by non-linear processes in the beam. Herewith the region where all magnitudes (electric field strength, density perturbations) gain their maximums, doesn't depend on the barrier profile (precisely, coordinate of the maximum density). Posi-

tion of this region is determined by the moment where instability magnitude reaches its non-linear threshold.

Conclusions. Dynamics of the modulated electron beam in the inhomogeneous plasma barrier is determined by ratio of simulation region length L , characteristic inhomogeneity length Δx and length of beam-plasma instability development a/γ . Small, moderate and strong increments' modes correspond to the conditions: $a/\gamma > L > \Delta x$, $L > a/\gamma > \Delta x$ and $L > \Delta x > a/\gamma$ respectively.

In the small increments' mode the barrier inhomogeneity influence on the beam-plasma instability development is significant. Herewith instability doesn't reach its maximum.

In the moderate increments' mode the barrier inhomogeneity influence on the beam-plasma instability development is still significant. Essential electric field growth just after the barrier centre causes the modulation instability development.

In the large increments' mode the barrier inhomogeneity influence on the beam-plasma instability development becomes insignificant. This effect causes the fast growth of beam-plasma instability increment with the beam current density increase. As a result, the initial beam modulation becomes almost noteless. Modulation instability in this mode can appear just near the injector.

Simulation results are consistent with the conclusion about impossibility of the plasma barrier transillumination using electron beams with large current densities that was obtained from the laboratory experiments [18].

1. Anisimov I.A., Levitsky S.M. On the possibility to observe the transitional radiation in the active beam-plasma experiments in the upper atmosphere and space // *Fizika plazmy*. – 1994. – Vol. 20, № 9.
2. Anisimov I.A., Levitsky S.M., Opanasenko O.V. et al. Experimental observation of the plasma wave barrier transillumination by means of electron beam // *Zhurnal tekhnicheskoi fiziki*. – 1991. – Vol. 61, № 3.
3. Anisimov I.O., Bojko N.O., Dovbakh S.V. et al. The influence of the initial modulation depth of the electron beam on its evolution in plasma // *Ukrainsky fizichny zhurnal*. – 2000. – Vol. 45, № 11.
4. Anisimov I.O., Dovbakh S.V., Levitsky S.M et al. Signals Transport through the Plasma Wave Barriers Using Electron Beams: Modes Concurrence // *Bulletin of Kyiv National University. Radiophysics and Electronics*. – 2000. – № 2.
5. Anisimov I.O., Kiyanchuk M.J. Evolution of a Modulated Electron Beam in Plasma for Different Modes of Beam-plasma Turbulence // *Ukrainsky fizichny zhurnal*. – 2008. – Vol. 53, № 4.
6. Anisimov I.O., Kiyanchuk M.J. Evolution of the modulated electron beam in supercritical plasma: simulation of initial-boundary problem // *Problems of atomic science and technology. Plasma electronics and new acceleration methods*. – 2006. – Vol. 5, № 5.
7. Anisimov I.O., Kotlyarov I.Yu., Levitsky S.M. et al. Study of the plasma barriers transillumination for electromagnetic waves using electron beams. 2. Space charge waves evolution in the barrier // *Ukrainsky fizichny zhurnal*. – 1996. – Vol. 41, № 3.
8. Anisimov I.O., Lyubich K.I. Plasma objects diagnostics using transitional radiation of the charged bunch // *Ukrainsky fizichny zhurnal*. – 1997. – Vol. 42, № 8.
9. Anisimov I.O., Lyubich K.I. Plasma-object diagnostics via resonant transitional radiation from an electron bunch // *Journal of Plasma Physics*. – 2001. – Vol. 66, № 3.
10. Anisimov I.O., Sasyuk D.V., Siversky T.V. Modified pack-

age PDP1 for beam-plasma systems' simulation // Dynamical system modelling and stability investigation. Thesis of conference reports, Kyiv, 2003. 11. Anisimov I.O., Soloviova M.J. Dynamics of the modulated electron beam in the inhomogeneous plasma barrier: kinetic effects. // Problems of atomic science and technology. Plasma physics. – 2008. – Vol. 14, № 6. 12. Anisimov I.O., Soloviova M.J. Dynamics of the modulated electron beam in the inhomogeneous plasma barrier: one-dimensional simulation using PIC method. // Problems of atomic science and technology. Plasma electronics and new acceleration methods. – 2008. – Vol. 6, № 4. 13. Birdsall Ch.K., Langdon A.B. Plasma Physics via Computer Simulation. – McGraw-Hill Book Company, 1985. 14. Kondratenko A.N., Kuklin V.M. Foundations of Plasma Electronics. – M, 1988. 15. Kuzelov M.V., Rukhadze A.A., Strelkov P.S. Plasma Relativistic SHF Electronics – M, 2002. 16. Lavergnat J., Pellat R. High-frequency spontaneous emission of an electron beam injected into the ionospheric plasma // Journal of Geophysical Research. – 1979. –

Vol. 84. 17. Mishin E.V., Ruzhin Yu.Ya., Telegin V.A. Interaction of Electron Beams with Ionospheric Plasma. – L, 1989. 18. Opanasenko O.V., Palets D.B., Romanyuk L.I. Study of the plasma barriers transillumination for electromagnetic waves using electron beams. 3. Influence of the eigenmodes of the beam-plasma system inside the barrier on the space charge wave excited in the beam // Ukrainsky fizichny zhurnal. – 1996. – Vol. 41, № 9. 19. Starodubtsev M., Krafft C. Whistler emission through transition radiation by a modulated electron beam spiralling in a magneto-plasma // Journal of Plasma Physics. – 2000. – Vol. 63, № 3. 20. Starodubtsev M., Krafft C., Thevenet P. et al. Whistler wave emission by a modulated electron beam through transition radiation // Physics of Plasmas. – 1999. – Vol. 6, № 5.

Submitted on 22.06.09

УДК 621.039.6

I. Bekh, Ph.D., O. Verbytska, stud.,
V. Il'chenko, Dr. of Sci., A. Lushkin, Ph.D.,
P. Nagula, engineer, V. Shcherban, stud.

THE INFLUENCE OF THE ELECTRIC FIELD ON THE EMISSIONS PROPERTIES OF THE SC-BA DISPENSED EMITTERS WITH THE W MATRIX

Вплив електричного поля на емісійні властивості Sc-Ба металевопористих емітерів з W матрицею було досліджено у високому вакуумі. Показано, що на відміну від попередніх результатів [3], зростання напруженості електричного поля, прикладеного до металевопористого емітера з W матрицею при постійній температурі, не призводить до суттєвої зміни хімічного складу емісійно-активної речовини.

Ключові слова: термоемісія, автоемісія, металевопористий, скандій.

The influence of the electric field on the emission properties of the Sc-Ba dispensed emitters with the W matrix is studied in a high vacuum. It is shown, that in contrast with previous results [3], the increasing of electric field intensity, applied to emitter with W matrix at constant temperature, don't cause to substantial alteration chemical composition of emission-active matter.

Key Words: thermo emission, field emission, dispenser, scandium.

Introduction. To add scandium as the monoxides to dispensed emitters is one of the ways to increase their emissive properties [4]. The researches of such type emitters are very important because today they have the most attractive operational parameters in comparison with oxide-coated and ordinary dispensed emitters. Investigation of the Sc-Ba emitters with Re-W matrix performed in our laboratory in partic ular showed, that in the temperature range 1100 K – 1500 K the influence of electric field on the emission properties of such emitters is very strong [3]. The mechanism of influence of the electric field on the emission properties of the Sc-Ba emitters is unknown and requires detailed study.

This paper presents the results of investigations of the influence of electric field on the emission properties of Sc-Ba dispensed emitters with the W matrix. Also, our paper includes results of the numerical calculations of the energy of displacement position of the maximum of electrons concentration in the emitters depends on electric field intensity for the case of a triangular potential barrier with the absence of image forces.

Experimental. The researches were carried out in UHV chamber and the pressure of residual gases did not exceed $5 \cdot 10^{-9}$ torr. The measurement of the emission properties was made in a flat diode system at a pulse mode. Pulse duration of the anodic voltage is 7 μ s. The amplitude of anodic voltage can change up to 600 V. The anode was the molybdenum plate (2x2x0.2 sm.), which was heating to the high temperature by the electron impact. The emitter-anode spacing interval d was equal to 1,2 mm, 1 mm, 0,8 mm and 0,6 mm and has been carefully controlled. Such set of distances allowed us to study influence of the electric field on the emissions properties of samples in the wide interval of field intensity.

For the numerical analysis based on the formula was taken evaluation of character depends of the energy position of the maximum of electrons concentration in the emitters depends on electric field intensity for the case of a

triangular potential barrier with the absence of image forces, as in [1].

$$F(\varepsilon) = \exp \left\{ -A(\varepsilon\varphi - \varepsilon)^{3/2} - \left(\frac{\varepsilon - \varepsilon\varphi}{kT} \right) \right\}, \quad A = \frac{8\pi\sqrt{2m}}{3} \frac{1}{h} \frac{1}{eE}, \quad (1)$$

here ε – kinetic energy carriers, $\varepsilon\varphi$ – work out, T – temperature, E – the electric field intensity. This first addendum in the exponential rate reflects the potential barrier transparency on the verge solid – vacuum in the case of a triangular barrier without the image force, and the second considers the dependence of electron concentration on temperature.

The function was investigated in the extreme for the position of maximum energy concentration of electrons in emitter. The result was obtained following the dependence of the energy of displacement position of the maximum of electrons concentration in the emitters depends on electric field intensity:

$$\Delta\varepsilon(E, T) = - \frac{1}{q} \left\{ E \cdot \frac{h \cdot q}{4\pi\sqrt{2m} \cdot k_B T} \right\}^2. \quad (2)$$

Using this dependence and calculated results were obtained, which for comparative analysis were imposed on the emission characteristics, measured for emitters with tungsten and rhenium-tungsten matrix. For the calculations was chosen interval of electric field intensity from $8 \cdot 10^4$ V/m to $5 \cdot 10^5$ V/m, step $0,5 \cdot 10^4$ V/m. In experiment was taken values of slopes of voltage-current characteristics of emitters with W and Re-W matrix.

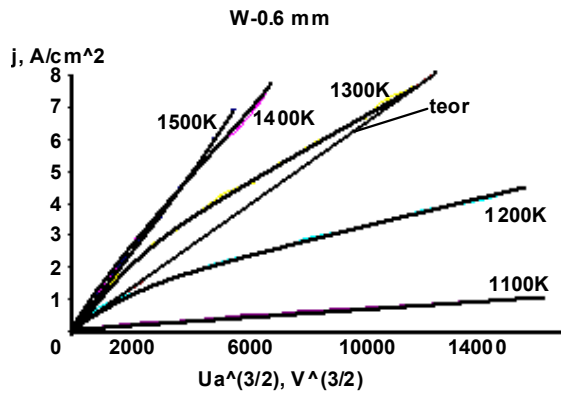


Fig. 1. Voltage-current characteristics for the sample with the W matrix, measured at different temperatures for distance between emitter and anode in 0,6 mm

From the fig. 1 one can see complete discrepancy between experimental curves and theoretical dependence, named "low 3/2". Remarkable, that with temperatures 1100 K and 1200 K curves lays below the theoretical dependence. With the temperature growth the opposite effect was observed: curves, corresponding to 1300 K, 1400 K and 1500 K lay above the "law 3/2".

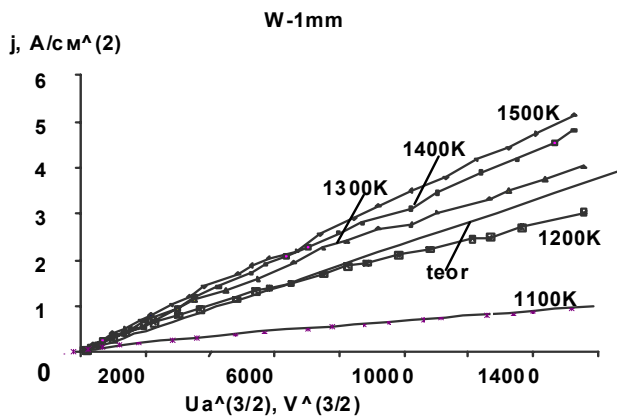


Fig. 2. Voltage-current characteristics for the sample with the W matrix, measured at different temperatures for distance between emitter and anode in 1 mm

With the increasing of distance between emitter and anode to 1mm, experimental curves approach to theoretical dependence, as it shown on the fig. 2.

As it was concluded from fig. 2, there were quite good correspondence between experimental and theoretical characteristics in the wide range of the anodic voltage for the temperature in 1300 K. So, decreasing of electrical field intensity cause decreasing of slope of the experimental volt-current curves in comparison with curves, measured for distance between emitter and anode in 0,6 mm.

This tendency keeps up fixed at the increasing of distance between emitter and anode up to 1,2 mm.

For detailed analysis of the influence of electric field on the emission properties of Sc-Ba dispensed emitters with the W matrix and for comparison with the previous results for the emitters with Re-W matrix [3], it was made numerical calculation of the energy of displacement position of the maximum of electrons concentration in the emitters depends on electric field intensity for the case of a triangular potential barrier with the absence of image forces.

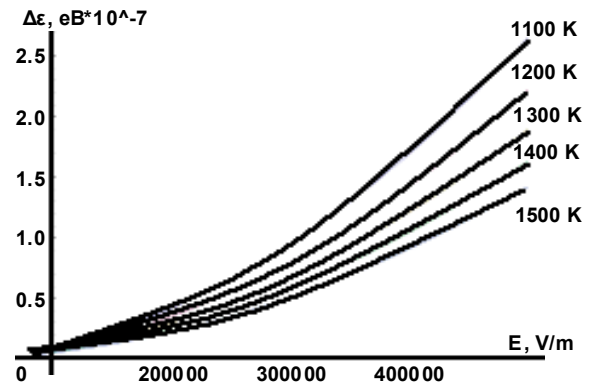


Fig. 3. Dependencies of changes of the displacement of energy position of the maximum of electrons concentration in the emitters depend on electric field intensity

The comparative analysis between experimental results and obtained calculated dependencies was made. Results of such comparison are shown on following figure.

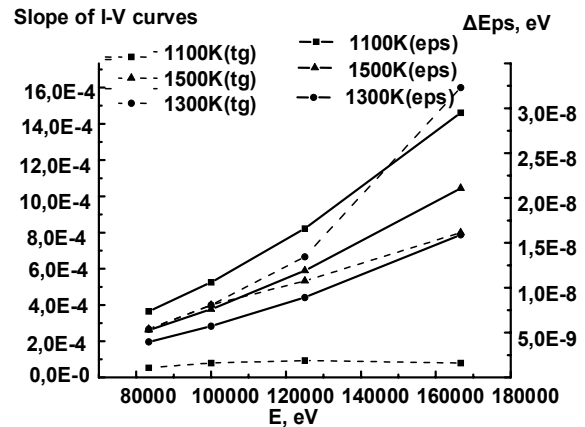


Fig. 4. Numerical calculations results and slope of voltage-current characteristics of emitters with W matrix (dashed lines) depends on the electric field intensity

Results of numerical calculation of the energy of displacement position of the maximum of electrons concentration and slope of voltage-current characteristics of emitters with W matrix depends on the electric field for temperatures of 1100 K, 1300 K and 1500 K are shown on the fig. 3. Shown dependencies are in good qualitative agreement to each other. What about experimental curve, measured at T=1100 K, the behavior of their slope could be explained thus: chemical composition and microstructure of the surface of emitter is not optimal yet, that's why emission probability of sample is low.

Results of numerical calculation of the energy of displacement position of the maximum of electrons concentration and slope of voltage-current characteristics of emitters with Re-W matrix depends on the electric field for temperatures of 1100 K, 1300 K and 1500 K are shown on the fig. 4. In contrast to fig. 3, there is no any coincidence between dependencies. More over, at relatively low temperatures (1100 K – 1300 K) the slope of voltage-current characteristic doesn't increase with growth of the electric field intensity and it even demonstrate some tendency to decreasing.

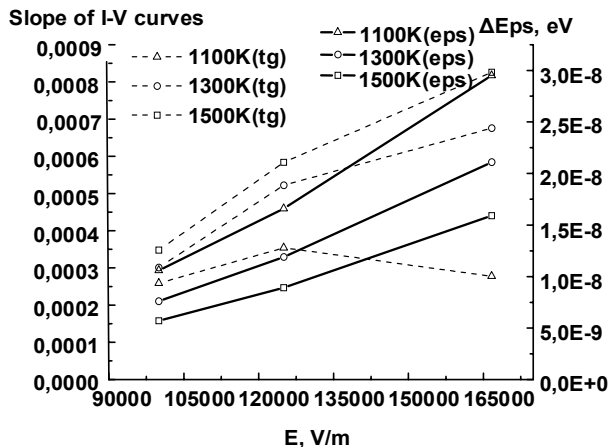


Fig. 5. Numerical calculations results and slope of voltage-current characteristics of emitters with Re-W matrix (dashed lines) depends on the electric field intensity

Results and discussion. Obtained results shows, that presence of qualitative agreement between numerically calculated dependencies and experimental data for emitter with W matrix and absence of such agreement between numerically calculated dependencies and experimental data for emitter with Re-W matrix can be presented as one more argument that processes of forming of emitter's work surface with different material of matrices are substantial different.

As one can see from figure 3, with the increase of the electric field intensity for the sample with W matrix at constant temperature clear tendency for growing of slope of its voltage-current characteristic is presents. The only exception is characteristic, measured at the 1100 K. Such temperature is not sufficient to optimize chemical composition and microstructure of the emitter's surface.

УДК 544.227

For emitters with the Re-W matrix, there is opposite tendency for behavior of the slope of their voltage-current characteristic with growth of the electric field intensity. Such difference can be explained with different mechanisms of the electric field influence on the emission properties for such type samples.

The absence coincidence between results of numerically calculated dependencies and experimental data for emitters with Re-W matrix can be explained in following way. The electric field modifies chemical composition of emission active matter and, as result, changes the depth of electric field penetration. So, the field emission part of the total anodic current decreased.

Conclusion. The increasing of the electric field intensity, applied to emitters with W matrix at constant temperature don't cause to substantial alteration chemical composition of emission-active matter in contrast to emitters with the Re-W matrix, where such difference is significant. It can be explained thus, the surface area of the emitters with the W matrix covered the emission-active matter considerably less, then emitters with the Re-W matrix [2].

Thus in the case of emitters with the W matrix the main factor of field emission is geometrical dimensions of crystallites and geometrical coefficient of the field amplification. In the case of emitters with Re-W matrix this factor is the penetration depth of electric field inside the emission-active matter. This factor is very sensitive to chemical composition of the emission-active matter [2].

1. Bekh I.I., Dmytryshyn O.A., Il'chenko V.V. et al. // Bulletin of the University of Kiev, Series: Physics & Mathematics. – 2005. – V. 4. 2. Bekh I.I., Getman O.I., Il'chenko V.V., et al. // Ukr. J. Phys. 2009. V. 54, №3. 3. Bekh I.I., Verbytska O.V., Getman O.I. et al. // Bulletin of the University of Kiev, Series: Physics & Mathematics. – 2008. – V. 4. 4. Haiqing Yuan, Kexin Pan, Xin Gu et al. // Appl. Surf. Sci. – 2005. – V. 251.

Submitted 23.10.09

D. Borzanytsya, stud.,
O. Lushkin, Ph. D.

THE INFLUENCE OF AN ELECTRIC FIELD ON COMPOSITION OF A SURFACE OF A NEGATIVELY POLED Z-CUT OF LITHIUM NIOBATE

The changes in Auger electron spectra that characterize the composition of the surface of a negatively poled z-cut of lithium niobate due to action potential relative to the crystal at different temperatures were received and analyzed. It was shown that applying of an external electric field opposite in a direction with the internal always causes rapid long-term surface changes, and the impact of an electric field coinciding in a direction with the internal one is appears only after preliminary action of positive potential.

Key words: lithium niobate, influence of an electric field, Auger spectroscopy, surface.

Було досліджено зміни Оже-електронних спектрів, що характеризують склад поверхні електронегативного z-зрізу кристалу ніобату літію, в залежності від прикладеного до кристалу потенціалу при різних температурах. Показано, що прикладання зовнішнього електричного поля, протилежного за напрямком до внутрішнього, завжди викликає швидкі довготривалі зміни складу поверхні, а вплив поля, напрямком якого співпадає з напрямком внутрішнього, відчувається лише після попередньої дії позитивного потенціалу.

Ключові слова: ніобат літію, вплив електричного поля, Оже – спектроскопія, поверхня.

Introduction. Lithium niobate (LN) – is one of the most widely used materials in modern solid state devices, processing and transmission of optical and acoustic information. Knowledge of optical and electrical properties of crystals and the possibility of their controlled change is very important for such LN applications. The electric field impact during the crystal growth can help to control a stoichiometry of its composition that is very important nowadays.

Experimental. Research was conducted in a vacuum chamber at a pressure that did not exceed 10^{-9} mmHg. There was an Auger analyzer type "cylindrical mirror" in the chamber to analyze the surface of the crystal. Target sample was a plate which had been cut out from the grown from

congruent melt by the Chohralsky method monodomain deliberately not doped LN crystal with size $5 \times 5 \times 0.5$ mm³. To the anode placed at a distance of 3 mm from the sample during different time periods applied potential at ± 500 V relative to the crystal. Recording of Auger spectra occurred immediately after exposure field and after some time afterwards. Before the exploration the sample was cleaned from surface contamination by heating to a temperature of 1200 K. The influence of different potential polarity investigated at temperatures of 300 K and 900 K.

Sample preparation. The experiment showed that the surface of the LN crystal at room temperature ($T=300$ K) consists of the carbon in large quantities (peak energy at

272 eV) and oxygen (peak energy at 510 eV) (Fig. 1a). Therefore for the further research it is necessary to warm up a sample for the gas pollution desorption.

The growing of the sample temperature leads to significant changes in Auger spectrum: decreases the amplitude of the peak of carbon and there are new peaks, which characterize the true composition of the surface, characterized this sample at a temperature $T=900$ K (Fig. 1b). At a temperature $T=1200$ K (Fig. 1c) there are more clearly presented Auger peaks that characterize the composition of the investigated crystals. To warm up the crystal to the higher temperatures to remove impurities is irrational, because it's causes the major changes in the crystal when $T>1200$ K (it is shown by mass spectrometric studies [4, 5]).

Resulted state of the crystal has a typical Auger spectrum (Fig. 1c) with the following values of energy of peaks: peaks with the energy at 32 eV and 43 eV related to lithium components, with the energy at 105 eV, 134 eV, 163 eV, 167 eV, 197 eV – is the Auger transitions involving niobium atoms. Analysis of the literature [2] indicates that the peak at energy 163 eV – interatomic Auger transition of Nb(M2, 3, M4, 5) O(V), and peak at energy 167 eV related to Auger transition in the niobium atoms involving peripheral electrons of Nb(M4, 5, N2, 3, V). With the oxidization of Nb decreases the amplitude of the energy peak at 167 eV and increases the amplitude of energy peak at 163 eV.

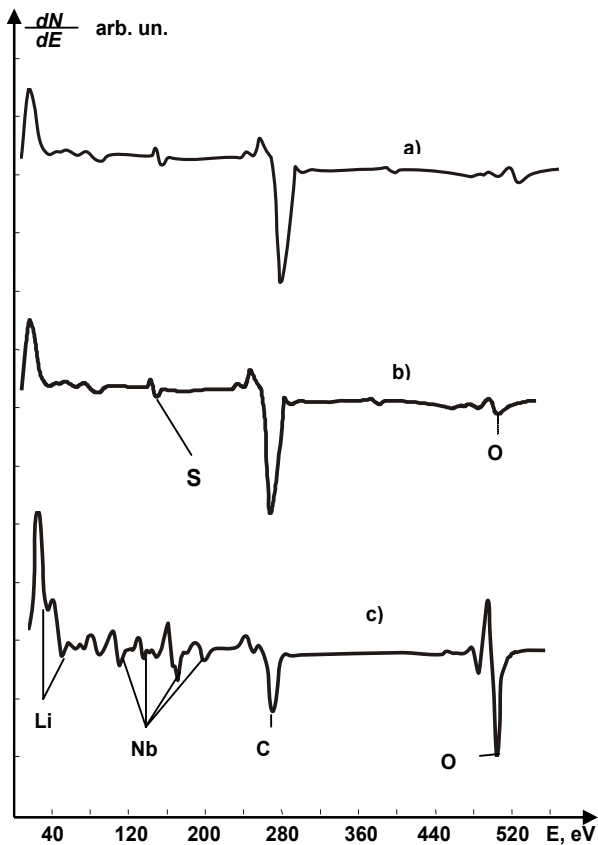


Fig. 1. Auger spectra of LN sample: a) before warming-up; b) at the temperature of $T=900$ K; c) resulted at $T=1200$ K

Nature of the appearance of an Auger peak with energy 85 eV most likely associated with the presence of impurities in a crystal in the form of Pb. The peak at 151 eV of energy is a contamination in the form of sulfur.

Results and discussion. Due to the fact that LiNbO_3 has pyroelectric and ferroelectric properties it is logically to begin the experiment on effects of the electric field on the composition of the sample surface at room temperature ($T=300$ K).

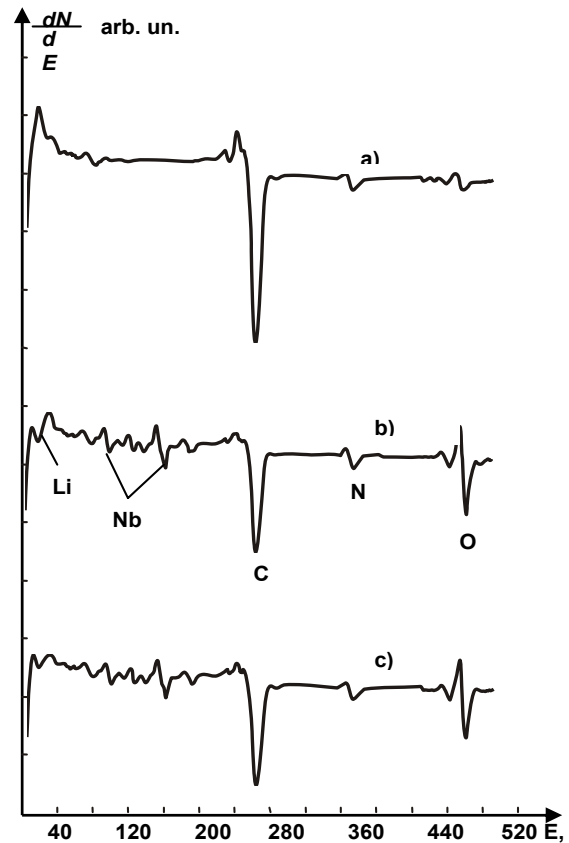


Fig. 2. Auger spectra of LN after field influence (+500 V on the anode) at $T=300$ K: a) before the impact; b) time of influence 1 min; c) time of influence 2 min

There are considerable changes of the surface composition of LN caused by the impact of potential difference in 500 V ("+" on anode relative to the crystal) during 1 min (Fig. 2b). Significantly reduced peak corresponds to Auger transition of carbon and emerged peaks, typical for LiNbO_3 . Additional influence of this field within 1 min. does not cause noticeable changes in the surface (Fig. 2c), which indicates a rapid and almost without inertia reaction of LN to the impact of the positive towards the crystal potential.

The further excerpt of the sample during several hours at $T=300$ K without external influences revealed that the surface remains unchanged. So the effects caused by the impact of the positive potential on the anode relative to the crystal at room temperature are long term and correlates well with existing data [3].

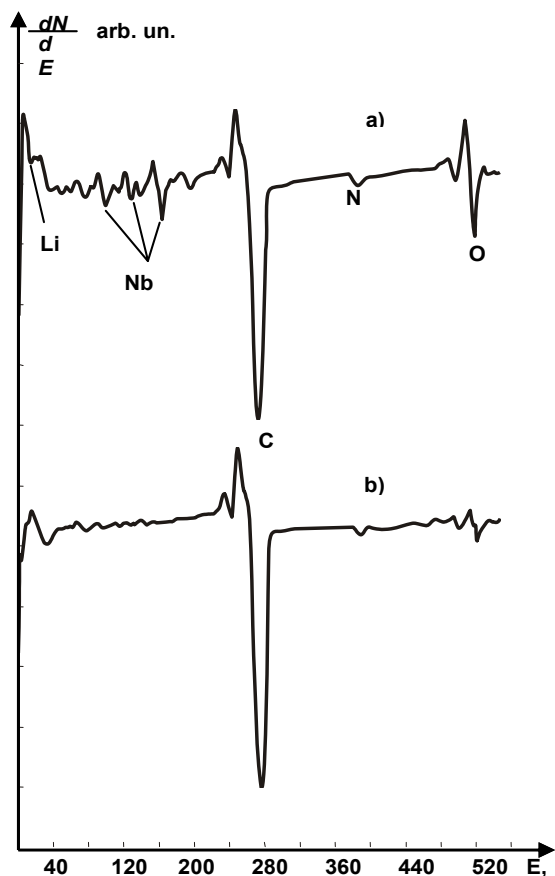


Fig. 3. Auger spectra of LN at T = 900 K:
a) at the initial state; b) after the influence of the potential of +500 V on the anode during t=1 min

When the sample temperature is increased to 900 K, the application of the positive potential on the anode relative to the sample causes changes, opposite to the previous ones (Fig. 3). Surface rebuilds by means of significant reducing or disappearing of the Auger peaks, which were typical for the investigated sample at T=900 K (Fig. 3b). Explanation of such behavior of the surface requires more research, because at this stage the mechanism of such impact is not entirely clear.

The experiments showed that the positive potential of the anode significantly influences the composition of the surface of a LiNbO_3 at room temperature or at higher temperatures. Moreover, changes occur regardless of the composition of the surface at the starting point. The composition of the surface totally changes in time about 1 min. and in the future remains unchanged for a long time. Long-term warming-up of the sample after field agency has shown that the composition of the surface transformed back to the condition typical for this temperature. Thus, all the effects of the field action disappear, but the relaxation time significantly depends on the temperature increase and lasts for hours. There are diffusion-migration processes and evaporation of atoms and molecules which occur during relaxation of the surface.

The experiment has proved that the electric field of reverse polarity (-500 V to the anode relative to the sample) does not affect the composition of the surface of LiNbO_3 when it is at room temperature. Similar results are obtained for T = 1200 K.

Another (Fig. 4) situation occurs when applying a negative potential after the previous impact of the positive field. These Auger spectra show that the consequences of actions field (+500 V to the anode) on the composition of the surface

of LN can be compensated, if applied to the anode a potential of -500 V relative to the sample. It results in reducing the amplitude of Auger peaks, which characterize niobium and lithium components of the investigated crystal, and also significantly reduced Auger peak of oxygen (Fig. 4b).

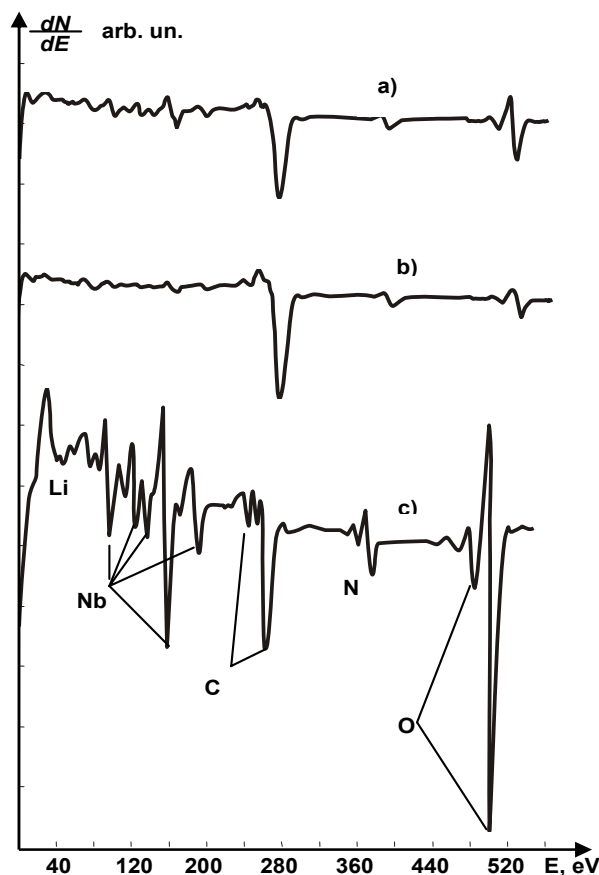


Fig. 4. Auger spectra of LN at T = 300 K:
a) after the influence of the potential of +500 V on the anode during t=1 min.; b) after the next influence of -500V for t=2 min.; c) in 10 hours without influence

In addition to rapid changes that occurred within 1 min., they were slower, but more significant, than changes in the surface (Fig. 4c). This allows saying about the inertial reaction of the surface of the negatively poled z-cut of LN to the influence of a negative potential after the previous impact of the positive field.

Fig. 4c shows that over a considerable period of time after the direct impact of the electric field significantly increased the amplitudes of the Auger peaks corresponds to transitions in niobium and involving niobium, carbon and oxygen peaks. In the same time disappeared the Auger peak of lithium oxide. The warm-up of the crystal to a temperature of 900 K qualitatively changes the old surface (Fig. 5a). There are surface chemical reactions as a conversion of carbon originally located on the surface in the form of graphite [1] (Fig. 4a) to the form of carbide – the niobium carbide formation (Fig. 4c), which is not destroyed even at T=900 K.

However, this condition can be quickly changed by the application of an electric field. For example, the niobium carbide can be transformed by the impact of positive potential to the crystal (Fig. 5b).

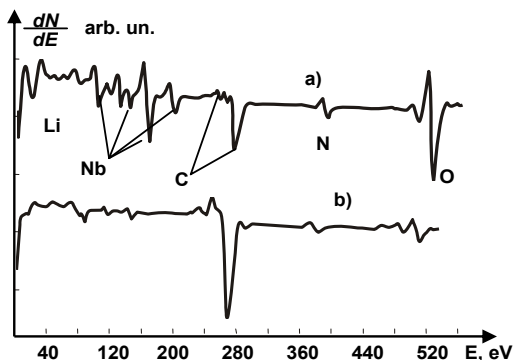


Fig. 5. Auger spectra of LN after the impact of electric field coinciding in a direction with the internal after previous action of positive potential: a) after the warming-up to T=900 K; b) after the influence of +500V during t = 1 min

Conclusions. The analysis of experimental results shows that the external electric field applied to the LiNbO₃ significantly alters the composition of its surface in the hot condition, and at room temperature. The character of changes depends on the field direction. The impact of the

positive potential of anode relative to the crystal for several minutes always leads to rapid long-term changes in the surface. Negative potential changes the composition of the surface only after preliminary action of positive potential, but such changes are sustained over a long time. In addition, surface alterations are not instantaneous as in the case of positive potential, and last for several hours. The only way to return the surface in the initial state is to repeat an impact of positive potential. This fact indicates that such changes include not only diffusion-migration processes but also chemical reactions.

1. Davis L.E., MacDonald N.C., Palmberg P.W. et al. Handbook of Auger electron spectroscopy // Physical electronics. Eden Prairie, MN. – 1976.
2. Ritz V.H., Bermudez V.M. Electron-spectroscopic of LiNbO₃ and LiTaO₃ surface. // Phys.Rev.B. – 1981. – v. 24, №10.
3. Ройтберг М.Б., Новик В.К., Гаврилова Н.Д. Особенности пирозлектрического эффекта и электропроводности в монокристаллах LiNbO₃ в области 20-250°С. // Кристаллография. – 1969. – т. 14, в. 5.
4. Шнюков В.Ф., Лушкін О.Є., Зиков Г.О., Назаренко В.Б. Вплив високотемпературного відпалу на випаровування кристалів ніобату літію // Вісник Київського університету. Радіофізика та електроніка. – 2000. – Вип. 1.
5. Шнюков В.Ф., Лушкін О.Є., Зиков Г.О., Назаренко В.Б. Особливості випаровування оксиду літію // Вісник Київського університету. Сер. Фіз. мат. науки. – 1997. – Вип. 4.

Submitted 26.10.09

UDC 537/539

A. Vakaliuk, B. stud., K. Greben, B. stud.,
A. Kalenyuk, Ph. D., V. Pan, D. Sci.,
O. Prokopenko, Ph. D.

METHOD OF HIGH-TEMPERATURE SUPERCONDUCTOR FILM NONLINEAR IMPEDANCE DETERMINATION USING COMBINED MICROSTRIP RESONATOR

У роботі представлено оригінальний варіант методики визначення нелінійного імпедансу ВТНП плівок за допомогою комбінованого мікросмужкового резонатора (МСР). Суттєвою перевагою методики є можливість дослідження властивостей ВТНП плівок у зовнішньому постійному магнітному полі. Дано загальний опис методики визначення імпедансу ВТНП плівок, проведено теоретичний аналіз комбінованого МСР за допомогою методу Бубнова – Гальоркіна – Рітца (модифікованого метода моментів) та визначено геометричний фактор комбінованого МСР. Проілюстровано застосування методики для дослідження властивостей ВТНП плівок у зовнішньому постійному магнітному полі.

Ключові слова: високотемпературний надпровідник, нелінійний імпеданс, мікросмужковий резонатор, геометричний фактор.

An original variant of high-temperature superconductor (HTS) film impedance determination using combined microstrip resonator (MSR) is presented. The significant advantage of the method is a possibility of HTS film properties investigation in applied external magnetic field. The general review of HTS film impedance determination has been made. The theoretical analysis of combined MSR has been carried out using Bubnov – Galerkin – Ritz method (modified momentum method) and the geometry factor of combined MSR has been estimated. The method application for the HTS film properties investigation in an applied external magnetic field is illustrated.

Key words: high-temperature superconductor, microstrip resonator, geometry factor.

Introduction. The discovery of high-temperature superconductivity in 1986 [1] and obtaining the high-temperature superconductors (HTS) with critical temperature T_C greater than the nitrogen boiling temperature in the next year gave a stimulus to the large-scale investigations of microwave properties of such materials and also made good starting conditions for further HTS applications in various areas of science and technology [2–5]. The HTS materials show considerable promise for the applications in the long-wave part of microwave band due to their low value of surface resistance at the nitrogen temperature in comparison with a surface resistance of pure metals like gold, silver, and copper and also due to the low level of temperature noise [2–5, 6]. Both these properties are very important for the creation of various microwave devices. The HTS devices have advantages before the similar devices made of traditional materials, because the HTS devices are characterized by a very high sensitivity, selectivity and ultra low losses [4].

HTS surface impedance $Z_S = R_S - iX_S$ is one of the most important parameter that defines the effectiveness of

HTS device application in a microwave band. HTS surface resistance R_S defines the level of losses and, consequently, the Q-factor of HTS device, and HTS inductance is characterized by a HTS surface reactance X_S . There are more than 20 various methods of HTS surface impedance determination at the present time [15]. The resonance method of HTS surface impedance determination is well known and commonly used amongst them due to its simplicity, good reproducibility, high enough sensitivity. This method unlike the other well known method (transport current method) allows determining real R_S and imaginary X_S parts of surface impedance. This method can be used in many variants and may be applied for the HTS film systems made by a planar technology. The interest for such systems is caused, first of all, by the existing of Meissner effect in HTS materials; due to that an electromagnetic field (EMF) penetrates only near-surface region of HTS sample [21] (and consequently, there is no sense to use bulk samples). Secondly, the interest is caused by the barest necessity of using HTS based integral schemes for the real applications. The microstrip systems have some advan-

tages amongst such systems [4, 21]. They can be easily fabricated by the existing planar technology, may operate in wide frequency range, and allow to easily realize the separation between dc and rf circuits of the system.

The aim of the paper is the presentation and approbation of the new variant of the HTS film impedance resonance determination method based on application of combined microstrip resonator (MSR). Significant disadvantage of common HTS MSR with strip and bottom plane made of HTS is the shielding effect that prevents carrying out complex physical experiments concerned with the action of an external magnetic field on HTS, for instance, the investigation of vortex dynamics, in such systems. This disadvantage can be neglected if combined MSR with strip made of HTS and bottom plate made of transparent to magnetic field material is used; magnetic field can penetrate the bottom pane and dielectric substrate and make influence on the HTS film (fig. 1). In comparison with other resonators (cavity, dielectric resonators), that are widely used for study the response of the mixed state, MSR have small sizes for low resonance frequencies. Only coplanar resonators can rival with the MSR, but the magnetic field in the coplanar resonators penetrates not only in the central strip but also penetrates the ground strips. That is lead to the additional losses difficult to take into account.

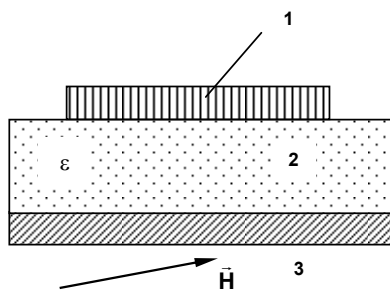


Fig. 1. Combined microstrip resonator (MSR) consists of HTS strip (1) on a dielectric substrate (2) and a metal plate (3).

The applied to the MSR an external magnetic field \vec{H} can penetrate the bottom plate and the substrate and can made an influence on the HTS strip

The basics of the proposed variant of the HTS film impedance determination is set out in the second part of the paper entitled "Method of HTS film impedance determination". The method is based on the standard resonance method of HTS film impedance determination [15]. The estimated by this method impedance value substantially depend on the geometry factor Γ of combined MSR. Taking this into account in the next part of the paper entitled "Geometry factor of combined MSR" the theoretical analysis of combined MSR is presented, the geometry factor is determined and several borderline cases of considered problem are analyzed. The fourth part of the paper entitled "Experiment" contains the description of the samples used during the experiment and the description of the experimental setup and experimental procedure. This part of the paper also contains the description of microwave response determination for the combined HTS MSR. In the last part of the paper, entitled "Results and discussion" the major experimental results are presented, the qualitative and quantitative analysis of the results is made. Also the advantages and disadvantages of the proposed method of HTS film impedance determination are analyzed in this section of the paper.

Method of HTS film impedance determination. The proposed method of HTS film impedance determination is based on the standard resonance method of HTS

impedance determination [12, 21]. The essence of the method is written further. The MSR with strip and bottom plate made of copper or other normal metal is placed in the experimental section and cooled to the temperature $T < T_C$, where T_C is the critical temperature of the HTS.

After that the resonance frequency $f'_0 = \omega'_0 / 2\pi$ is measured and unloaded Q-factor Q'_0 is determined for the fundamental mode of the MSR. The unloaded Q-factor Q'_0 can be easily calculated if the loaded Q-factor Q'_{load} for the fundamental mode of the MSR is measured and coupling coefficient β' between the MSR and the transmission line is known. For instance, it can be done in such way: $Q'_0 = Q'_{load} (1 + \beta')$. The combined MSR consists of top strip made of HTS (the strip is HTS film) and bottom plate made of copper (or other normal metal transparent to the dc magnetic field). The mandatory requirement is the high-precision HTS film impedance determination is the identity of all geometric sizes and substrate properties for the metal and combined MSR.

The combined MSR with top strip in the form of HTS film must be placed in the experimental section exactly as it was done for the metal MSR. After that the resonance frequency of the fundamental MSR mode $f_0 = \omega_0 / 2\pi$ is measured and unloaded Q-factor Q_0 of the MSR for the fundamental mode is determined: $Q_0 = Q_{load} (1 + \beta)$, where Q_{load} is the loaded Q-factor of the combined MSR, β is the coupling coefficient between the combined MSR and the transmission line.

The real R_S and imaginary X_S parts of HTS film impedance can be calculated using a set of experimental data $(\omega'_0; Q'_0)$, $(\omega_0; Q_0)$ in the absence of dc magnetic field (zero-field cooling regime).

Finite unloaded Q-factor of the metal MSR is defined by the losses in the top strip and bottom plate, losses in the dielectric substrate and radiation losses. Taking this into account, the inverse value of Q'_0 can be written in the form:

$$\frac{1}{Q'_0} = \frac{1}{Q'_{top}} + \frac{1}{Q'_{bottom}} + \frac{1}{Q'_d} + \frac{1}{Q'_r}, \quad (1)$$

where Q'_{top} is the Q-factor defined by losses in the top strip, Q'_{bottom} is the Q-factor defined by losses in the bottom plate, Q'_d is the Q-factor due to losses in the dielectric substrate, and Q'_r is the Q-factor defined by radiation losses. In the case of combined MSR the value inverse to the unloaded Q-factor Q_0 can be written in the form similar to (1):

$$\frac{1}{Q_0} = \frac{1}{Q_{top}} + \frac{1}{Q_{bottom}} + \frac{1}{Q_d} + \frac{1}{Q_r}, \quad (2)$$

where all not primed values have the same meanings as the corresponded primed values.

The first important circumstance for the further analysis is the fact that metal and combined MSR have identical geometry sizes and fabricated on the identical dielectric substrates. Taking into account the smallness of HTS film surface resistance R_S and the aforesaid circumstance allow us to assume that the field distribution for the metal and combined MSR is the same. As it was shown in [7, 9], this assumption is correct if the HTS film surface resistance R_S is substantially smaller than the metal surface resistance R'_S (metal used for the MSR fabrication):

$R_S \ll R'_S$. In the case when this condition is not fulfilled the proposed method may be used but the analysis of an experimental data became complex enough.

The second important circumstance is the fulfillment of conditions:

$$Q_d, Q_r \gg Q_{top}, Q_{bottom} \text{ and } Q'_d, Q'_r \gg Q'_{top}, Q'_{bottom},$$

that are typical for the common experiments. In order to fulfill these conditions the dielectric substrate should be made of the dielectric with high permittivity $\epsilon \gg 1$ and low loss tangent $\text{tg} \delta \ll 1$ for the temperature T at which the Q-factors Q_0 and Q'_0 are determined. The condition $\epsilon \gg 1$ allow to substantially increase the radiation Q-factor Q_r , and condition $\text{tg} \delta \ll 1$ guarantee the smallness of losses in the dielectric substrate, because $Q_d, Q'_d \sim \text{tg}^{-1} \delta$. Eventually, the EMF energy distribution aside the geometrical sizes of the MSR can be changed by varying the thickness of the dielectric substrate. This gives the possibility to additional control on the values Q_d, Q_r, Q'_d, Q'_r in the experiment. In practice, the dielectric substrates with thickness from several hundreds of nanometers and up to several hundreds of micrometers, and permittivity $\epsilon \sim 10$ and loss tangent $\text{tg} \delta \sim 10^4 \div 10^5$ at frequency $f \sim f_0, f'_0$ and temperature T are used. Under such conditions, the relations $Q_d, Q_r \gg Q_{top}, Q_{bottom}$ and $Q'_d, Q'_r \gg Q'_{top}, Q'_{bottom}$ are typically fulfilled with precise enough for practical applications. In that case the method can be used even if $R_S \sim R'_S$ or $R_S \gg R'_S$.

Thus, taking into account made remarks, from the Ex. (1)–(2) in the case $Q'_{bottom} \approx Q_{bottom}$, $Q'_d \approx Q_d$, $Q'_r \approx Q_r$ one can obtain:

$$\frac{1}{Q'_0} - \frac{1}{Q_0} \approx \frac{1}{Q'_{top}} - \frac{1}{Q_{top}} = \frac{Q_{top} - Q'_{top}}{Q'_{top} Q_{top}}. \quad (3)$$

Let's underline, that obtained expression follows from the Ex. (1)–(2) at once, even if conditions $Q'_d \approx Q_d$, $Q'_r \approx Q_r$ are not fulfilled, but if assumptions $Q_d, Q_r \gg Q_{top}, Q_{bottom}$ and $Q'_d, Q'_r \gg Q'_{top}, Q'_{bottom}$ are made. This means that Ex. (3) can be used even if the field perturbations are large when changing the top metal strip of the MSR to the HTS strip, but the radiation and dielectric Q-factors remain substantially greater than the Q-factors defined by losses in the top strip and bottom plate.

The Q-factor defined by the losses in the top metal strip of the MSR Q'_{top} and Q-factor defined by the losses in the HTS film Q_{top} are inverse proportional to the surface resistance of the metal R'_S and HTS film R_S , respectively [7, 9]:

$$Q'_{top} = \frac{\Gamma'}{R'_S}, \quad Q_{top} = \frac{\Gamma}{R_S}, \quad (4)$$

where $\Gamma' = \omega_0 \mu_0 \frac{\int (H')^2 dV}{\oint (H')^2 dS}$, $\Gamma = \omega_0 \mu_0 \frac{\int H^2 dV}{\oint H^2 dS}$ are the

geometrical factors, depend on the magnetic field H, H' distribution in the MSR, μ_0 is the vacuum permeability, V is the "resonator volume" (volume, where the field exists), S is the surface that bounds the volume V . Assuming that field distribution is not changed when top metal strip is exchanged with HTS film and taking into account aforesaid

remarks, the expression for the surface resistance of HTS film can be written from (3) and (4) in the case $\Gamma = \Gamma'$:

$$R_S = R'_S - \Gamma \frac{Q_0 - Q'_0}{Q'_0 Q_0}. \quad (5)$$

If we take into account that geometry factor of the MSR can be determined in the experiments with metal MSR and metal surface resistance R'_S can be easily estimated using the formula of microwave electrodynamics [22], we can rewrite Ex. (5) in the final form:

$$R_S = R'_S \left(1 - \frac{Q_0 - Q'_0}{Q_0} \right). \quad (6)$$

In that variant of the method, the HTS film surface resistance is determined if the value of metal surface resistance R'_S is known.

The disadvantage of presented method is neglecting the fact that the Q-factors Q_{bottom} and Q_{top} may substantially differ by value in the experiment, that may lead to the precision loss during the estimation of surface resistance R_S by Ex. (6). In order to avoid this, Ex. (2) may be written in the form (where we neglect the items Q_d^{-1} and Q_r^{-1}):

$$\frac{1}{Q_0} = \frac{1}{Q_{top}} + \frac{1}{Q_{bottom}} = \frac{\Gamma}{R}, \quad (7)$$

where R is the average value of surface resistance depend on HTS film surface resistance R_S and metal surface resistance R'_S . If we assume the geometry factor Γ of the system is known (it can be determined in the experiment for metal MSR with estimated value of metal surface resistance R'_S , or it can be estimated theoretically during the solution of corresponding electromagnetic problem – see further), then the average value of surface resistance R can be obtained from the Ex. (7). It is obvious, that $R \rightarrow R'_S$ for the temperature $T < T_C$ and low frequency f_0 , when $R_S \ll R'_S$. On the contrary, if the frequency f_0 is high enough, and $R_S \gg R'_S$, then $R \rightarrow R_S$. Considering such asymptotic behavior, it is convenient to write the quantity R as function of quantities R_S and R'_S in the form:

$$R = \alpha R_S + (1 - \alpha) R'_S, \quad (8)$$

where α is dimensionless parameter, that can vary from zero to one unit ($0 \leq \alpha \leq 1$). Parameter α can be determined during the analysis of experimental data series, for instance, the dependence of unloaded Q-factor of combined MSR on frequency or temperature. It is difficult to estimate the parameter theoretically; but even in this case obtained results are not always having one meaning. However, the following artificial method can be used for rough estimation of α value. Let's assume, that $R_S \ll R'_S$, i.e., in fact, assume $R_S = 0$. Let Γ_{bottom} is the geometry factor in this case (obtained in the experiment or calculated theoretically), then one can see that $\alpha_{bottom} = 1 - \Gamma / \Gamma_{bottom}$ from Ex. (7)–(8). And on contrary, if we consider the case $R_S \gg R'_S$, i.e., in fact, assume $R'_S = 0$, then we obtain $\alpha_{top} = \Gamma / \Gamma_{top}$ from Ex. (7)–(8), where Γ_{top} is the geometry factor for that case. Both approximations must lead to the same average value of parameter α , that can be estimated as follows:

$$\alpha \approx \sqrt{\alpha_{top} \alpha_{bottom}} = \sqrt{\frac{\Gamma}{\Gamma_{top}} \left(1 - \frac{\Gamma}{\Gamma_{bottom}} \right)}. \quad (9)$$

Using this expression an approximate calculation of parameter α can be made. After that the obtained value can be defined more precisely by analyzing experimental data and further can be used for determination of HTS film surface resistance:

$$R_S = \frac{1}{\alpha} \left[\frac{\Gamma}{Q_0} - (1-\alpha)R'_S \right]. \quad (10)$$

Imaginary part X_S of HTS film impedance is defined by the geometrical capacitance C_g and inductance L_g , and also by the kinetic inductance L_k (exist due to Cooper pair movement and vortex creep) in the case of combined MSR:

$$X_S(\omega) = \frac{1}{i\omega C_g} + i\omega(L_g + L_k). \quad (11)$$

The natural resonance frequency of combined MSR is defined by the inductance of the system $L = L_g + L_k$ and capacitance C_g :

$$\omega_0 = \frac{1}{\sqrt{(L_g + L_k)C_g}}. \quad (12)$$

In most cases, it is correct to assume that capacitance C_g and inductance L_g does not depend on temperature T and magnetic field induction B . Thus, the dependence of quantities $X_S(T, B)$ and $\omega_0(T, B)$ on T and B is defined by the kinetic inductance $L_k(T, B)$ of the system.

The eigen resonance frequency of the fundamental mode of the combined MSR is vary while the temperature or magnetic field induction is varying, and

$$\begin{aligned} \Delta\omega_0(T, T', B, B') &= \omega'_0(T', B') - \omega_0(T, B) = \\ &= \frac{1}{\sqrt{(L_g + L_k(T', B'))C_g}} - \frac{1}{\sqrt{(L_g + L_k(T, B))C_g}} \end{aligned} \quad (13)$$

It is obvious, the approximation function for $L_k(T, B)$ can be achieved while analyzing the experimental dependence of $\Delta\omega_0(T, T', B, B')$. This enables the opportunity to determine the values of L_g and C_g for some frequency ω_0 from a set of experimental data and dependence of $L_k(T, B)$, if $|\Delta\omega_0| \ll \omega_0$.

The most simple realization of this method is based on the application of idea of geometry factor Γ . It was shown in paper [9] that

$$\frac{\Delta\omega_0(T, T', B, B')}{\omega_0(T, B)} = -\frac{\Delta X_S(T, T', B, B')}{2\Gamma}. \quad (14)$$

If the geometry factor of the system Γ is known, it is possible to determine the change of HTS film reactance caused by the changes of temperature and magnetic field induction using Ex. (14). It is possible to achieve approximate dependence of $\Delta L_k(T, T', B, B')$ and, further, make approximation for the absolute value of $L_k(T, B)$ by analyzing dependence (14) in a wide range of temperatures and magnetic field inductions.

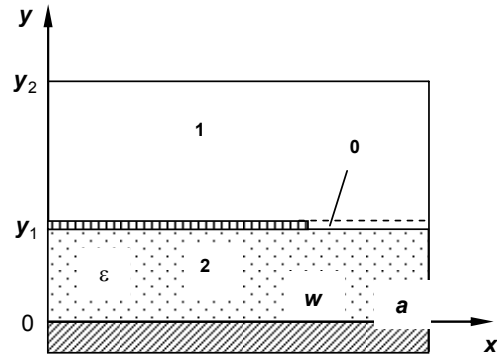


Fig. 2. Model of elementary cell, used during the theoretical analysis of combined microstrip line: 0, 1, 2 – partial areas

When surface resistance R_S and reactance X_S of HTS film is determined for the case of zero external dc magnetic field, the dc magnetic field can be applied to the structure. The field should penetrate bottom plate and dielectric substrate and make an influence on the HTS film. Thus, proposed method of combined MSR allows investigating the dependence of HTS film surface impedance $Z_S = R_S - iX_S$ on magnitude and direction of the magnetic field.

Geometry factor of combined MSR. In order to determine the geometry factor of combined MSR, the EMF of combined MSR natural oscillations has been determined. During the analysis a monochromatic approximation was used; the media assumed to be linear, homogeneous, and isotropic. Also there was made an assumption that losses in the system are small, thus, an ideal boundary condition of electric wall was used on the surface of metal and HTS.

First of all, an intermediate electromagnetic problem of determining an eigen EMF of combined microstrip line (MSL) was solved. In order to do that a model of combined MSL in the form of two elementary cells was analyzed (fig. 2). Also it was made an assumption that the top strip of the MSL (HTS film) is infinitely thin.

Theoretical analysis of the combined MSL was carried out by the partial wave synthesis with edge condition [10–12]. The elementary cell was divided by three partial areas (see fig. 2):

Area 1: $0 \leq x \leq a, y_1 \leq y \leq y_2, \forall z$;

Area 2: $0 \leq x \leq a, 0 \leq y \leq y_1, \forall z$;

Area 0: $w \leq x \leq a, y = y_1, \forall z$.

We assume the area 2 is filled by dielectric of permittivity ϵ , other areas are filled by vacuum.

The following boundary conditions for the EMF components were used on the boundaries between different media:

$$\begin{aligned} E_{x1}(0 \leq x \leq w, y_1, z) &= E_{z1}(0 \leq x \leq w, y_1, z) = 0, \\ E_{x2}(0 \leq x \leq w, y_1, z) &= E_{z2}(0 \leq x \leq w, y_1, z) = 0, \\ E_{x1}(w \leq x \leq a, y_1, z) &= E_{x0}(w \leq x \leq a, y_1, z), \\ E_{z1}(w \leq x \leq a, y_1, z) &= E_{z0}(w \leq x \leq a, y_1, z), \\ H_{x1}(w \leq x \leq a, y_1, z) &= H_{x0}(w \leq x \leq a, y_1, z), \\ H_{z1}(w \leq x \leq a, y_1, z) &= H_{z0}(w \leq x \leq a, y_1, z), \\ E_{x2}(w \leq x \leq a, y_1, z) &= E_{x0}(w \leq x \leq a, y_1, z), \\ E_{z2}(w \leq x \leq a, y_1, z) &= E_{z0}(w \leq x \leq a, y_1, z), \\ H_{x2}(w \leq x \leq a, y_1, z) &= H_{x0}(w \leq x \leq a, y_1, z), \\ H_{z2}(w \leq x \leq a, y_1, z) &= H_{z0}(w \leq x \leq a, y_1, z), \\ E_{x2}(x, 0, z) &= E_{z2}(x, 0, z) = 0. \end{aligned} \quad (15)$$

Moreover, the electric or magnetic wall condition was written on the joint side plane of two elementary cells at the plane $x=0$ (in the symmetry plane of the system). The electric wall conditions were also written for the external boundary planes of the elementary cells, located in the planes $x=a$, and $y=y_2$.

Using boundary conditions for inner boundaries (boundaries that belong to only one area) the eigen functions of Helmholtz' equation were obtained in areas 1 and 2. The longitudinal components of EMF E_z and H_z in areas 1 and 2 can be written using the basis based on obtained eigen functions:

$$E_{zj}(x, y, z) = \sum_{m,n=1}^{\infty} k_{jmn}^2 A_{jmn} \Phi_{jm}(x) F_{jmn}(y) e^{-i\beta_{mn}z},$$

$$H_{zj}(x, y, z) = \sum_{\substack{m,n=0 \\ m+n>0}}^{\infty} k_{jmn}^2 B_{jmn} \Psi_{jm}(x) G_{jmn}(y) e^{-i\beta_{mn}z}, \quad (16)$$

where k_{jmn} is the critical wave number, $\Phi_{jm}(x)$, $\Psi_{jm}(x)$, $F_{jmn}(y)$, $G_{jmn}(y)$ are the eigen functions in the area j , β_{mn} is the propagation constant of eigen TE_{mn} or TM_{mn} wave, A_{jmn} is the magnitude of TM_{mn} -wave, B_{jmn} is the magnitude of TE_{mn} -wave.

The EMF in area 0 was written using the edge conditions near infinitely thin conductor at $x=w$, $y=y_1$:

$$E_{z0}(x, y, z) = \sum_{m,n=1}^{\infty} k_{0mn}^2 A_{0mn} \Phi_{0m}(x) e^{-i\beta_{mn}z},$$

$$H_{z0}(x, y, z) = \sum_{\substack{m,n=0 \\ m+n>0}}^{\infty} k_{0mn}^2 B_{0mn} \Psi_{0m}(x) e^{-i\beta_{mn}z}, \quad (17)$$

where k_{0mn} is the critical wave number, $\Phi_{0m}(x)$, $\Psi_{0m}(x)$ are the eigen function that satisfy edge conditions. Taking into account the recommendations made in papers [9, 14, 17], the functions $\Phi_{0m}(x)$, $\Psi_{0m}(x)$ were chosen in the class of Chebyshev's polynomials.

Substituting the Ex. (16)–(17) in the boundary conditions and taking into account the eigen function orthogonality relations, one can obtain the system of linear algebraic equations (SLAE) for the unknown magnitudes A_{jmn} , B_{jmn} , $j=0,1,2$.

First of all, it was made an assumption that the frequency f (wave number) of the eigen waves is known. Taking this into account a set of propagation constants β_{mn} can be evaluated from the condition of SLAE determinant equal to zero. Generalizing these results it is was calculated the dependence $\beta_{mn}(f)$ for the combined MSL when frequency f is varied from 100 MHz to 1 GHz with step 100 kHz.

Elementary cell only approximately correspond to the cross-section of real MSR. The major factor important for the optimizing solving technique (but deleterious from a point of physics view) is a conducting screen around the cell. In order to neglect the screen influence on the MSR properties from the one hand and take into account the radiation from the structure, from the other hand, several cases with the different screen sizes were a , y_2 were analyzed. It was achieved that the precision loss during the estimation of MSL microwave properties due to the influence of the screen is less than 1% for the case of $a \geq 10w$, $y_2 \geq 10y_1$. This precision loss is acceptable, so in further

analysis only the case of $a = 10w$, $y_2 = 10y_1$ is analyzed.

The relations between the amplitudes A_{jmn} , B_{jmn} were obtained for the case of $A_{111} = 1$ or $B_{110} = 1$ in the frequency range from 100 MHz to 1 GHz. After that the normalized EMF distribution was obtained for the combined MSL.

In the next stage a theoretical analysis of combined MSR has been made. The MSR was considered as a MSL section of finite length l . To simplify the task, we assume the combined MSR is excited by the eigen waves of rectangular waveguide with sizes equal to the sizes of conducting screen. Also the assumption has been made that waves traversed the structure fall to the output rectangular waveguide with the same sizes as input waveguide. Thus, the problem of combined MSR excitation was analyzed for the model of shielded MSR, placed in the endless rectangular waveguide with the sizes of cross-section equal to the size of the conducting screen.

Taking into account the symmetry of the system relatively to the center of combined MSR, electromagnetic problem was solved only in half-space $z > 0$. To do that a boundary condition of electric or magnetic wall was written in the symmetry plane $z=0$. The boundary continuity conditions for the tangential components E_x , E_y , H_x , H_y of EMF was written in the plane $z=l/2$. The fields of combined MSR were written using the eigen fields of the combined MSL. The fields outside the combined MSR area were written using the eigen fields of rectangular waveguide. As a result of this, taking into account the eigen function orthogonality relations, the SLAE for unknown oscillation amplitudes was obtained using Bubnov – Galerkin – Ritz method (modified momentum method).

The MSR eigen frequencies were estimated using the condition of SLAE determinant equal to zero. Further, the case of system excitation by the unit signal of eigen MSR frequency has been considered. The amplitudes of reflection and transmission waves were determined and the reflection and transmission coefficients were calculated.

Using obtained results for the lossless system a geometry factor for the fundamental mode of the combined MSR was estimated. The estimation was performed using the formula:

$$\Gamma = \omega_0 \mu_0 \frac{\int V H^2 dV}{\oint S H^2 dS} \quad (18)$$

at the angular frequency $\omega_0 / 2\pi = 850$ MHz for three different cases. In the first case only losses in the top strip (HTS film) were taken into account and the estimated value of geometry factor was $\Gamma_{top} \cdot \frac{2\pi}{\omega_0} = 0.83 \Omega / \text{GHz}$. In the

second case considering only losses in the bottom plate (the surface resistance of the copper was $R_S = 3.25 \text{ m}\Omega$) the estimated value of geometry factor was substantially greater than in the first case: $\Gamma_{bottom} \cdot \frac{2\pi}{\omega_0} = 14.1 \Omega / \text{GHz}$. In

the third case the losses in the top strip and the bottom plate were considered. In that case the estimated value of geometry factor was approximately equal to the geometry factor obtained for the top strip: $\Gamma \cong \Gamma_{top}$.

Thus, the geometry factor for the fundamental mode of combined MSR was estimated using Bubnov – Galerkin – Ritz method (modified momentum method).

Experiment. The experimental study of HTS film surface impedance was carried out for the thin $\text{YBa}_2\text{Cu}_3\text{O}_{7.6}$ films (YBCO) with thickness ~ 500 nm and the critical temperature of the transition origin $T_C \approx 90$ K.

The films were fabricated using laser pulse deposition from YBCO target [5] on a monocrystal LaAlO_3 substrate. Similar films were investigated by the methods of high-resolution electron microscopy, atomic force microscopy, and low frequency magnetic methods, in which a dynamic magnetic susceptibility were studied in the low frequency magnetic field [18]. Analogous films have been also investigated in microwave band [19, 20]. The results of investigations have shown the high perfection and structural homogeneity of the YBCO films, obtained for the same deposition parameters.

The single-sided HTS MSR were made using the methods of photolithography and further etching of the YBCO films in the 1% solution of orthophosphoric acid. The length of the top strip was ~ 62 mm and its width was 0.5 mm. The bottom plate was made of copper.

A cryostat was used for cooling the system. It allows changing temperature from the room temperature to the nitrogen boiling temperature (~ 78 K).

An external rotating magnet allows creation of dc magnetic field with induction $B = 0 \div 1$ T.

The investigation of MSR microwave response was carried out using symmetric two-port measurement scheme [9] and vector network analyzer [20].

As a results of measurements, the temperature magnetic induction dependencies of resonator loaded Q-factor $Q_{load}(T, B)$, eigen resonance frequency $f_0(T, B)$, and also insertion losses $IL(T, B)$ at $f = f_0$ were obtained.

The value of the insertion was equal or less than -40 dB in the whole range of temperature and magnetic field induction used in the experiment. Taking this into account, it is possible to consider that the equality $Q_{load}(T, B) = Q_0(T, B)$ is fulfilled with a high precision. Therefore, the temperature and field dependence of unloaded Q-factor $Q_0(T, B)$ has been obtained in the experiment, in fact.

The using of weak coupling and low probe microwave power ($P_{in} = -10$ dBm) allow to realize the linear regime of resonator microwave response measurement [19]. This is necessary to avoid various nonlinear effects [19, 20], appear in planar HTS structures. The existing of the effects can be proved by observation the existing of impedance dependence on microwave power: $Z_S = Z_S(P_{in})$.

Results and discussion. As a result of measurements, temperature dependencies of unloaded Q-factor were obtained for the first four modes of combined MSR. In contrast to the HTS MSR with unloaded Q-factor of 10^4 and more, the unloaded Q-factor of the combined MSR was near 4500 at the temperature $T = 78$ K and frequency $f_0 = 0.85$ GHz (MSR fundamental mode). So it means that all losses exist mainly in the normal bottom plate for the nitrogen temperatures and less temperatures. The method sensitivity is lesser in that temperature – magnetic field range than the method sensitivity at higher sensitivity or in stronger fields.

The surface resistance of the copper was estimated using the measurements results for analogous copper resonators (the unloaded Q-factor was $Q_{Cu}(78 \text{ K}) = 260$) and Ex. (4). The obtained surface resistance was

$R_{S,Cu}(78 \text{ K}, 0.85 \text{ GHz}) = 4.5 \text{ m}\Omega$. This value is close to the values obtained by other methods [11]. The surface resistance of the copper practically did not changed in the measurement temperature range.

Using the obtained value of $R_{S,Cu}$, Ex. (10), and taking into account that surface resistance of normal metals is proportional to the $\sqrt{f_0}$, the temperature dependency of YBCO strip surface resistance was obtained for the combined MSR (fig. 3). The surface resistance of the sample R_S at temperature 78 K and frequency $f_0 = 0.85$ GHz was $20 \mu\Omega$. The frequency dependence of R_S at low temperatures is approximately close to the square dependence ($R_S(f_0) \sim f_0^2$). This result is in good agreement with two-fluid model of superconductivity.

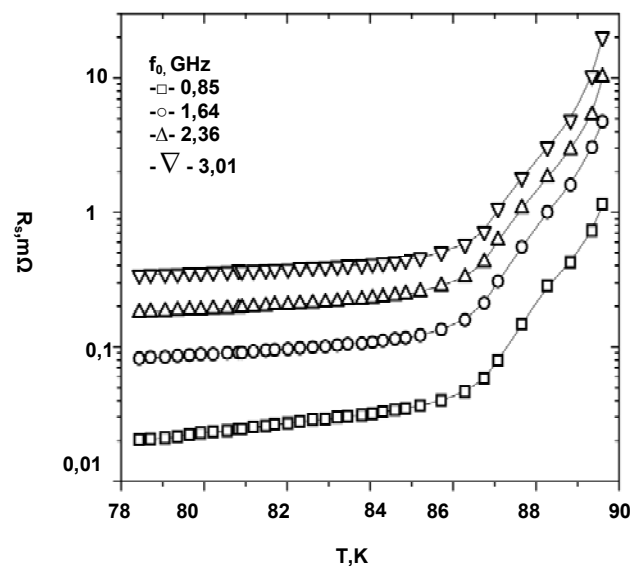


Fig. 3. Temperature dependence of HTS strip surface resistance

Further, a dc magnetic field was applied to the resonator. The estimation procedure for field dependence of surface resistance was the same as the procedure for temperature dependence. As result of this estimation, the field dependencies of the YBCO film surface resistance $R_S(B)$ were obtained for different direction of magnetic field relative to the axis c (fig. 4). The field was always perpendicular to the direction of microwave current and, therefore, the geometry of constant Lorentz force was realized [8]. The field dependencies are different for the perpendicular and parallel cases (see fig. 4). The existing of angular dependence of YBCO surface resistance is the consequence of YBCO anisotropy, to be exactly, the anisotropy of viscosity factor η . The absence of this dependence indicates the existing of large quantity of intergranular coupling in the film [8].

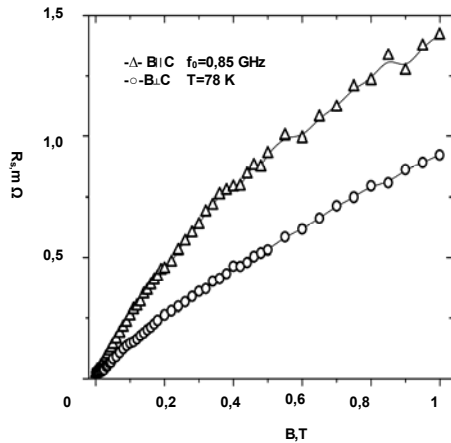


Fig. 4. The dependence of surface resistance $R_s(B)$ on the induction magnitude of dc magnetic field for the cases of parallel and perpendicular field direction relative to the crystallographic axis c of HTS film

The field dependence of surface resistance looks linear for high enough fields ($B > 0.3$ T). Similar situation can be observed on the field dependencies of surface reactance change $\Delta X_s(B)$ (fig. 5).

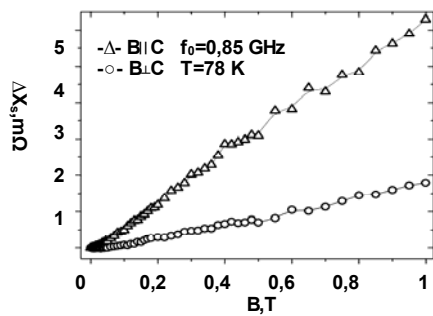


Fig. 5. Dependence of surface reactance change $\Delta X_s(B)$ on magnetic field induction, obtained from the field dependence of resonance frequency change $\Delta f_0(B)$ using Ex. (12)

Linear field dependencies are the evidence of realization of the individual pinning mechanism [7]; in the simplest case this effect can be described by Gittleman – Rosenblum model [6].

The realization of individual pinning mechanism is possible in the case of effective pinning center superiority under the total vortex quantity (each vortex is pinned at one pinning center). The vortex quantity can be estimated as:

$$n = \frac{B}{\Phi_0}, \quad (19)$$

where Φ_0 is the magnetic flux quantum.

The vortex concentration was $n \cong 10^{10} \text{ cm}^{-2}$ for magnetic field induction of 1 T.

The investigation of similar films by the high-resolution electron microscopy method, have shown an existence of large quantity of linear defects in the field (the concentration of defects is 10^{10} cm^{-2}) [18]. These defects are the effective pinning centers. Therefore, the pinning is realized on the lengthy defects in the case of parallel field ($B \parallel c$). In the case of perpendicular field ($B \perp c$) the pinning on point defects [7] and on film boundary [13] looks to be dominant.

Conclusion. The application of combined (superconductor + metal) microstrip resonator for investigation of HTS film microwave response in dc magnetic field is demonstrated.

As a result of investigation it was proved that in the case of surface resistance equality for top strip and bottom plate in the microstrip resonator, the Q-factor of the system mainly depends on the losses in the resonator top strip. The influence of bottom plate can be registered in the case:

$$\frac{R_{S,bottom}}{R_{S,top}} \geq \frac{\Gamma_{bottom}}{\Gamma_{top}}. \quad (20)$$

For the considered microstrip resonators this ratio is $\frac{\Gamma_{bottom}}{\Gamma_{top}} \cong (15 - 20)$, and therefore, the proposed method has high enough sensitivity in the temperature range from the nitrogen temperature and up.

The disadvantage of the proposed method includes the difficulty of surface resistance estimation for the bottom plate. But it can be avoided by the application of identical metal resonator or by the temperature decrease down to the temperature level, when the contribution of top strip to the system Q-factor can be ignored.

The authors are appreciated to Flis V.S., Moskalyuk V.O. for HTSC films and Valeriy F. Tarasov for fruitful discussions.

1. Bednorz J.G., Müller K.A. Possible high T_c superconductivity in the Ba-La-Cu-O system // Z. Phys. B. – 1986. – Vol. 64, № 2. 2. Braginski A.I. Superconducting Electronics: a Dream, or Reality? // Bulletin of the Polish Academy of Sciences. Technical Sciences. – 1997. – Vol. 45, № 1. 3. Chernoplekov N.A. Superconducting technologies: current state and perspectives of practical applications // Bulletin of Academy of Sciences of Russia. – 2001. – T.71, № 4. – С.303-319. (in Russian) 4. Emelianov V. Microelectronic microwave components based on high-temperature superconductors // Bulletin of Academy of Sciences of Russia. – 2002. – T. 77, № 6 (in Russian) 5. Flis V.S., Pan V.M., Komashko V.A., Moskalyuk V.O., Peshko I.I. Basis of physico-technology deposition of thin HTSC films $\text{YBa}_2\text{Cu}_3\text{O}_{7-x}$ // Progress in Physics of Metal. – 2006. – V. 7, № 4. 6. Ginzburg V.L. Superconductivity: the day before yesterday – yesterday – today – tomorrow // Uspekhi Fizicheskikh Nauk. – 2000. – T.170, № 6. 4. 7. Gittleman J.I. and Rosenblum B. // Phys. Rev. Lett. – 1966. – Vol. 16. 8. Golosovsky M., Tsindlekht M., Chayot H., Davidov D., Bontemps N., Chocron S., Iskevitch E., Brodskii B., and Contour J.P. Anisotropic magnetic-field-dependent surface resistance of $\text{YBa}_2\text{Cu}_3\text{O}_{7-x}$ epitaxial films by the parallel-plate resonator technique // Physica C. 9. Golosovsky M., Tsindlekht M., and Davidov D. High-frequency vortex dynamics in $\text{YBa}_2\text{Cu}_3\text{O}_7$ // Supercond. Sci. Technol. – 1996. – № 9. 10. Hurd R.A. The edge condition in electromagnetics // IEEE Trans. on Antennas and Propagation. – 1976. – Vol. 24, №1. 11. Kalenyuk A.A. Nonlinear microwave response of a superconducting $\text{YBa}_2\text{Cu}_3\text{O}_{7-x}$ microstrip transmission line with a constriction // Low Temperature Physics. – 2009. – Vol. 35, № 2. 12. Kutovoj V.A., Nikolaenko A.A., Stoev P.I. Investigation of superficial resistance of different purity copper at boiling nitrogen temperature depending on treatment of current-conducting layer // Problems of atomic science and technology. Series: vacuum, pure materials, superconductivity (16). – 2007. – № 4. 13. Lancaster M.J. Passive Microwave Device Applications of High-Temperature Superconductors. – Cambridge, U.K. – 1997. 14. Luzhbin D.A., Kasatkina A.L., Pan V. M. The surface impedance of a thin superconducting film in a parallel magnetic field // Fizika Nizhnikh Temperatur. – 2001. – T. 27, № 5 (in Russian) 15. Meixner J. The Behavior of Electromagnetic Fields at Edges // IEEE Trans. on Antennas and Propagation. – 1972. – Vol. 20, №4. 16. Mende F.F., Spitsyn A.I. Surface impedance of superconductors. – K., 1985. (in Russian) 17. Microelectronic microwave devices / G.I. Veselov, E.N. Egorov, Yu.N. Alekhin et al. / Ed. by G.I. Veselov. – M., 1988. (in Russian) 18. Mitra R., Lee S.W. Analytical techniques in the theory of guided waves. – N.-Y., 1971. 19. Pan V.M., Cherpak Yu.V., Komashko V.A., Pozigun S.A., Tretiachenko C.G., Semenov A.V., Pashitskii E.A., and Pan A.V. Supercurrent transport in $\text{YBa}_2\text{Cu}_3\text{O}_{7-x}$ epitaxial thin films in a dc magnetic field // Phys. Rev. B. – 2006. 20. Pan V.M., Kalenyuk A.A., Kasatkina A.L., Ivanyuta O.M., and Melkov G.A. Microwave Response of Perfect $\text{YBa}_2\text{Cu}_3\text{O}_{7-x}$ Thin Films Deposited on CeO_2 -Buffered Sapphire: A Probe for Pairing Symmetry // Journal of Superconductivity and Novel Magnetism. – 2007. – Vol. 20, № 1. 21. Pan V.M., Luzhbin D.A., Kalenyuk A.A., Kasatkina A.L., and Komashko V.A., Velichko A.V. and Lancaster M. Microwave impedance of $\text{YBa}_2\text{Cu}_3\text{O}_{7-x}$ high-temperature superconductor films in a magnetic field // Low temperature physics. – 2005. – Vol. 31, № 3-4. 22. Shmidt V.V. Introduction to the physics of superconductors. – M., 2000. (in Russian) 23. Vainshtein L.A. Electromagnetic waves. – M., 1988. (in Russian) 24. Waveguides with complex shape of cross-section / Ed. by V.M. Sedukh. – X., 1979. (in Russian) 25. Zargano G.F., Lerer A.M., Lyapin V.P., Sinyavsky G.P. Transmission lines with complex cross-section. – Rostov, 1983.

Received by editorial board on 20.07.09

UDC 533.951

D. Velykanets', PhD student, I. Anisimov, Dr. Sc.,
T. Litoshenko, PhD

INFLUENCE OF THE HEATING NON-LINEARITY ON THE PLASMA DENSITY PROFILE DEFORMATION IN THE INHOMOGENEOUS BEAM-PLASMA SYSTEMS

Методом макрочастинок досліджено роль нагрівної нелінійності в процесі деформації профілю концентрації плазми в області локального плазмового резонансу, збуджуваній модульованим електронним пучком. Нагрівна не лінійність помітна, коли ВЧ поле, що збуджується в області локального плазмового резонансу, досягає максимального значення. Розрахунки показують, що нагрівна нелінійність грає помітну роль в деформації профілю концентрації.

Ключові слова: плазма, електронний пучок, нагрівна не лінійність.

The influence of heating non-linearity on plasma density profile deformation in local plasma resonance region excited by the modulated electron beam is studied via computer simulation using PIC method. Heating non-linearity is noticeable when the HF electric field, excited in local plasma resonance region reaches its maximal value. The estimations show that heating non-linearity plays the significant role in plasma density profile deformation.

Key words: plasma, electron beam, heating non-linearity.

Introduction. Interaction of the modulated electron beam with inhomogeneous plasma is interesting for various problems of plasma electronics. The deformation of plasma density profile in the local plasma resonance region (LPRR) [7] affects the effectiveness of the linear beam modes' conversion into electromagnetic and Langmuir waves [1], that is important for the construction of the beam-plasma amplifiers and generators of direct radioemission, for interpretation of experiments in the upper atmosphere and outer space, etc.

During the propagation of the modulated electron beam in the inhomogeneous plasma the most intensive HF electric field is excited in LPRR. This field causes the plasma density profile deformation, and the mechanism of this process is traditionally associated with the ponderomotive force caused by the spatially inhomogeneous HF field. Meanwhile, the attention of the researchers still wasn't attracted by the heating non-linearity [6] caused by the plasma electrons' heating by electric field excited in LPRR. This field transmits its energy to plasma electrons, and some of them are accelerated to velocities that substantially exceed the thermal velocity [5-4]. Kinetic energy of electrons' ordered motion partially turns to electrons' thermal motion energy, and plasma gas-kinetic pressure in LPRR increases. As the result, plasma is pressed out from this region. Then one can expect that the heating non-linearity also makes the contribution to the plasma density profile deformation in addition to the striction non-linearity.

The aim of this work is to study the influence of heating non-linearity on plasma density profile deformation in LPRR excited by the modulated electron beam. The study was carried out via computer simulation using PIC method.

Model description and simulation parameters. Worm isotropic planarly-stratified plasma with initially linear density profile was studied. Thin ribbon electron beam with initial density modulation moved parallel to the plasma density gradient. Beam's modulation frequency was equal to local plasma frequency in the center of the system, initial modulation depth was 100%.

The simulation was carried out using the modified PDP2 code [2]. Plasma density varied in the range $(1,6 \div 4,8) \cdot 10^8 \text{ cm}^{-3}$ at the length of 60cm, simulation region had the width 10cm, beam's width was 1cm. Plasma electrons temperature was 2eV, plasma ions – 0.15eV, beam's density and velocity were $2 \cdot 10^6 \text{ cm}^{-3}$ and $3 \cdot 10^9 \text{ cm/s}$, respectively, frequency of the beam modulation was 0.16GHz.

Simulation results and discussion. In order to study the influence of heating non-linearity on the plasma density profile deformation two-dimensional spatial distributions of plasma electrons' temperature were obtained for three different time points. Temperature was measured via total kinetic energy of

plasma electrons located in the spatial interval $(\Delta x, \Delta y)$, without taking into account the average velocity:

$$W_{\Delta x, \Delta y} = \frac{m}{2} \left(\sum_i^{\Delta N} (v_{xi} - \langle v_x \rangle)^2 + \sum_i^{\Delta N} (v_{yi} - \langle v_y \rangle)^2 \right), \quad (1)$$

where ΔN is the number of plasma electrons in the spatial interval $(\Delta x, \Delta y)$. The heating non-linearity is significant when the temperature of plasma electrons in LPRR exceeds the temperature of plasma electrons in other regions at least in two times [6].

Figs 1-3 present the temperature spatial distributions $W(x, y, t)$ for three sequent time points, normalized by initial temperature magnitude, and corresponding spatial distributions of the electric field, plasma electrons' and ions' density perturbations.

At the initial time point ($t = 150\text{ns}$) HF electric field excited in LPRR by the beam, only rises (fig. 1b), but the process of plasma electrons heating starts: electrons' temperature in LPRR is noticeably larger than in other regions (fig. 1a). The ratio of the maximal electrons' temperature in LPRR to the averaged plasma electrons' temperature W_m/W_{av} is equal to 1.8. Thus, the magnitude of electric field in LPRR is not enough for the considerable heating of plasma electrons, so in the initial stages of beam-plasma interaction heating non-linearity is not noticeable. Plasma electrons' and ions' density perturbations caused by ponderomotive force in LPRR are also inessential (fig. 1c-d).

By the time point $t = 250\text{ns}$ the electric field in LPRR increases (fig. 2b), and plasma electrons become more heated. The ratio of the maximal electrons' temperature in LPRR to the averaged plasma electrons' temperature is equal to 3.2 (fig. 2a), so the heating non-linearity is noticeable on this stage of beam-plasma interaction. One can see from fig. 2c, that plasma electrons leave LPRR, and the density cavity appears on the plasma electrons' density profile. Under the influence of the ambipolar field, caused by the electro-neutrality violation in LPRR [3], the ions' density profile is also perturbed (fig. 2d). At the late stage of interaction the configuration of electric field in LPRR changes, but its magnitude reaches the maximal value (fig. 3 b). The temperature of plasma electrons in LPRR becomes even greater ($W_m/W_{av} = 3.33$ – see fig. 3 a), and the cavities on electrons' and ions' density profiles become deeper (fig. 3 c-d).

As one can see, at every stage of beam-plasma interaction the heated plasma electrons are observed only from the left of local plasma resonance point (from the side of subcritical plasma), because in this region the electric field, excited by the modulated electron beam, reaches its maximal magnitude.

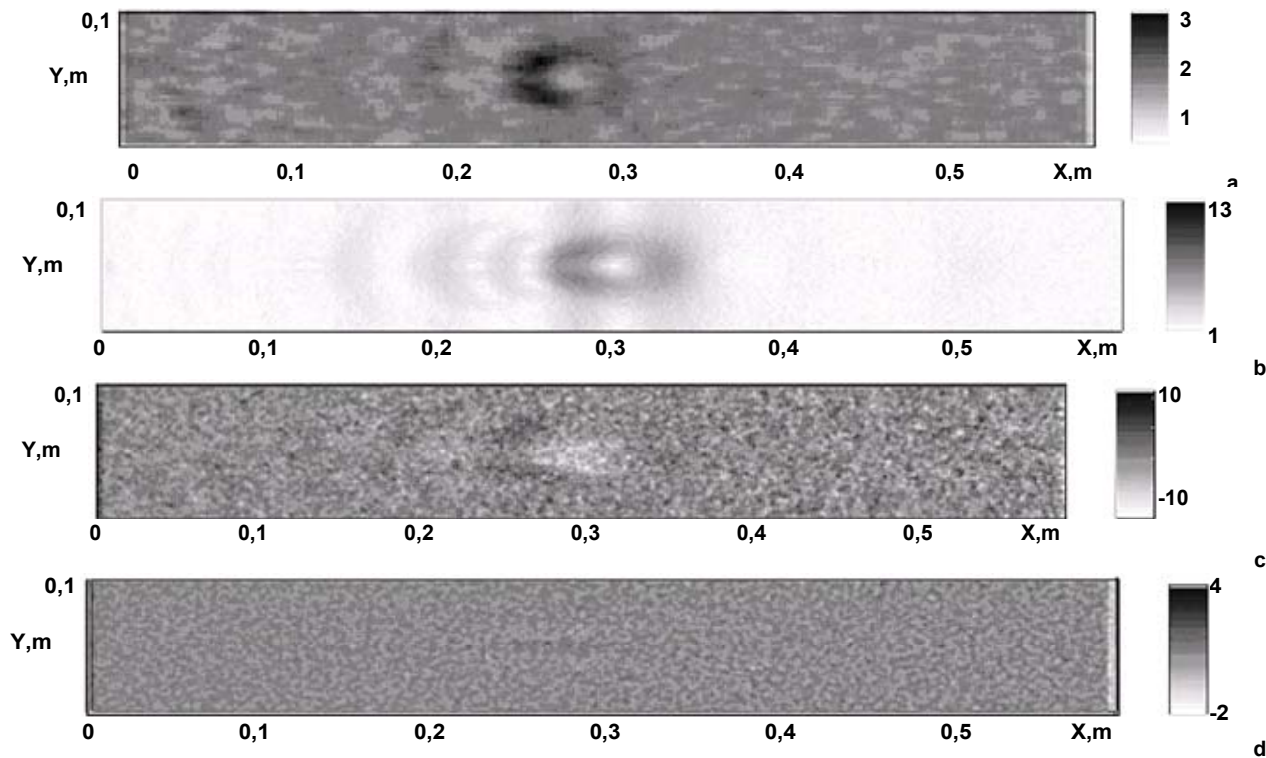


Fig. 1. Spatial distributions of plasma electrons temperature (a), electric field (b), plasma electrons (c) and ions (d) density perturbations in the moment of time $t=150\text{ns}$

As it is known [6], the ratio of the amplitude of the HF electric field E_m to the threshold magnitude E_p of the heating non-linearity can be estimated from the relation

$$\frac{E_m^2}{E_p^2} = \frac{T_e}{T_0} - 1. \quad (2)$$

Thus, in the region of the maximal heating of plasma electrons $E_m^2/E_p^2 = 2,3$.

The threshold magnitude of the electric field, that defines the striction non-linearity in the collisionless plasma, can be estimated from formula [6]

$$E_s^2 = \frac{8mk_B T_0 \omega^2}{e^2}. \quad (3)$$

From the simulation results $E_m = 1300\text{kV/cm}$, so according to the formula (3) considering the simulation parameters $E_s = 9.6\text{kV/cm}$, thus $E_m^2/E_p^2 = 1,8$.

The estimations carried out above show that contributions of the heating and striction non-linearities to plasma density profile deformation in LPRR have the equal order of magnitude.

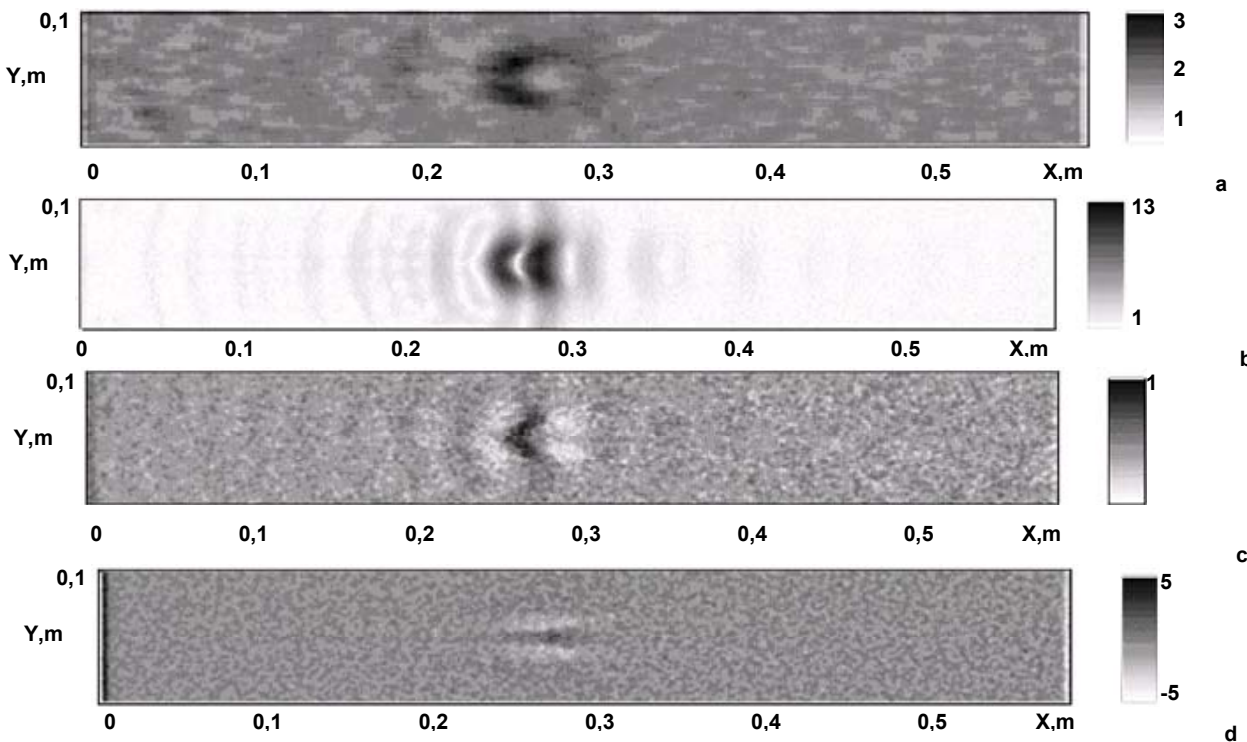


Fig. 2. The same as on the Fig. 1 in the moment of time $t=250\text{ns}$

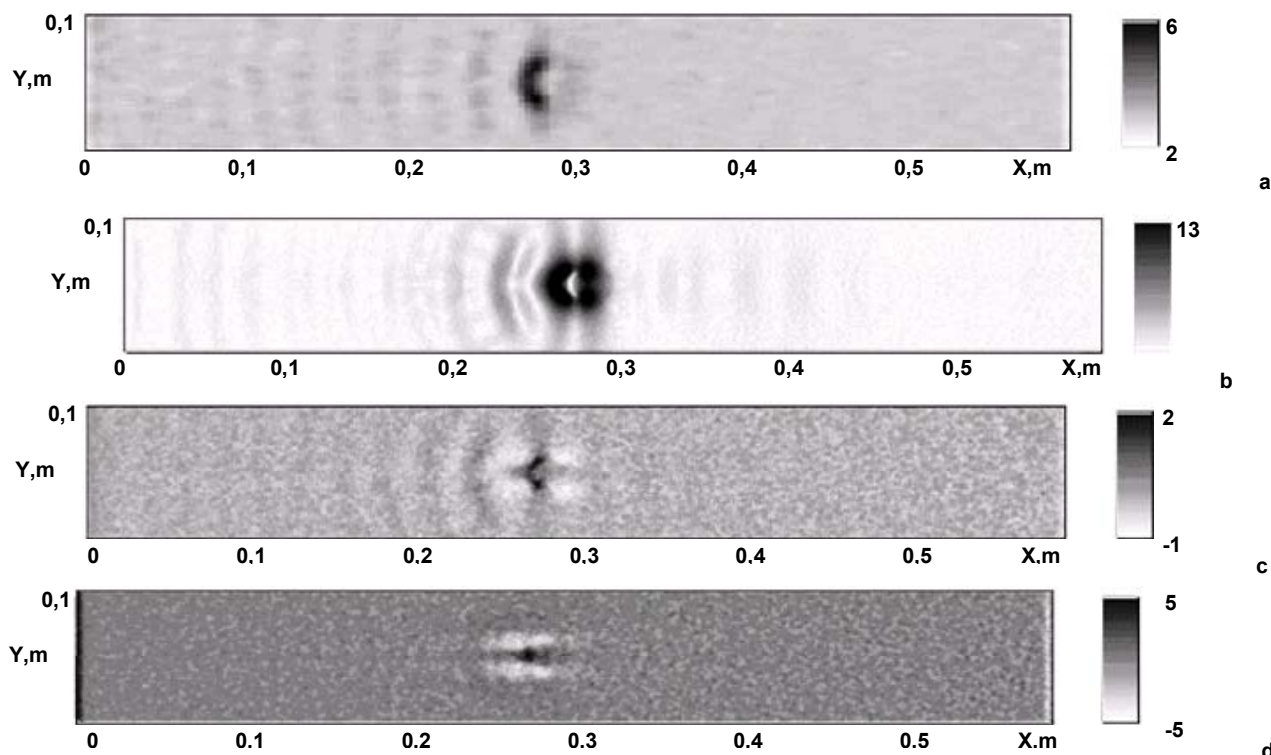


Fig. 3. The same as on the Fig. 1 in the moment of time $t=300\text{ns}$

Conclusions. The heating of plasma electrons in LPRR takes place at each stage of beam-plasma interaction. Heating non-linearity is noticeable when the electric field, excited in LPRR by the modulated electron beam, is saturated. Formation of the density cavity takes place in the same time. The estimations show that heating non-linearity plays the significant role in plasma density profile deformation.

1. Anisimov I.O., Kelnyk O.I., Soroka S.V. Interaction of the modulated electron beam with inhomogeneous plasma: Langmuir waves excitation. // Proc. of the 4th Intern. Young Scientists' Conf. on Appl. Phys. – Kyiv, 2004.
2. Anisimov I.O., Litoshenko T.Eu.. 2D electrostatic simulation of the modulated electron beam interaction with inhomogeneous plasma. // Problems of

- Atomic Science and Technology. Series: Plasma Physics (12). 2006. №6.
3. Anisimov I.O., Litoshenko T.Eu.. Non-linear interaction of the modulated electron beam with the local plasma resonance region: 2D simulation // Kyiv University Bulletin. Phys.&Math, 2006, 4, 251-256. (In Ukrainian).
4. Anisimov I.O., Litoshenko T.Eu., Velykanets, D.M.. Kinetic effects in the local plasma resonance region excited by modulated electron beam: 2D simulation // Problems of Atomic Science and Technology. Series: Plasma Physics (14). 2008. №6.
5. Anisimov I.O., Soroka S.V., Velykanets' D.M.. Electrons' acceleration in inhomogeneous plasma excited by the modulated electron beam. // Kyiv University Bulletin. Phys.&Math, 2007.
6. Gurevich A.V., Shwarzburg A.B.. Non-linear theory of the wave propagation in ionosphere. – M., Nauka, 1973.
7. Kovrizhnykh L.M., Sakharov A.S. Generation of cavity in local plasma resonance region // Fizika plazmy. 1980, vol. 6, № 1.

Received by editorial board on 21.10.09

UDC 535.4

A. Goloborodko, Ph. D.

THE MODEL OF THE MATERIAL WITH NEGATIVE REFRACTION INDEX

The phenomenon of negative refraction is observed as multiple scattering of electromagnetic wave by the composite two-dimensional periodic structure with layers, which have different indices of refraction. The computer simulation has shown that the 32 layer propagation of the special periodically structures can give another direction of the propagation beam.

Keywords: negative refraction index, multiple scattering, Snell's law.

Ефект утворення негативного показника заломлення розглянуто як послідовне розсіювання електромагнітної хвилі на шаруватій двовимірній періодичній структурі. За допомогою чисельного моделювання показано, що для вказаної структури з 32 шарами можливе виникнення розсіювання у від'ємному напрямку.

Ключові слова: від'ємний показник заломлення, багаторазове розсіювання, закон Снеліуса.

1. Introduction. The refraction index is a commonly used constant of the optical properties of the material, and, for example, the knowledge of two continuous materials refraction indices is sufficient to predict the refraction angle of a beam incident at the interface between these two materials. The real part refraction index of all known materials is positive; however, this is not a fundamental restriction. It is pointed out in early paper by V. G. Veselago [18], that there is a material that could exhibit negative real part of refraction

index. Veselago has discovered the possibility of negative refraction via a theoretical exploration of "left-handed" materials – the materials which electrical permittivity (ϵ) and magnetic permeability (μ) are simultaneously negative.

Since left-handed materials do not exist in nature, the discussion of left-handed materials was not particularly relevant; in fact, the topic was not further pursued until recently, when it was demonstrated that artificially structured left-handed materials could be constructed [17]. Composite ma-

terials can be considered as effectively homogeneous media when the structure varies spatially on a scale much less than the incident radiation. A set of effective response functions ϵ_{eff} and μ_{eff} can then be ascribed to these materials. Such materials have been used to demonstrate negative refraction experimentally at microwave frequencies [4], thus motivating further research into the possibilities that negative index materials might provide. Even the simplest configurations of negative index materials, which can be analyzed by analytical methods, have yielded surprising results [18], indicating there is much to discover in this new field.

Of particular interest are the sign of the refractive index (direction of phase velocity), and the direction of the energy flow. The sign of the refractive index depends on the location of zeros and poles of $\epsilon\mu$ in the complex ω -plane. This indicates that it is possible to obtain negative refractive index without any magnetic resonances, $\mu = 1$, but instead two electric resonances. Indeed, it has been suggested that certain nonmagnetic media, with active and passive dielectric resonances, can exhibit negative refraction [2]. In such right-handed materials the wave vector and Poynting vector both point towards the source [16].

There was proposed a structure made of periodic metal rings and showed that negative permeability can also be achieved [6, 9, 12, 20]. J. B. Pendry and G. Dewar showed that composite materials with negative refraction are the set of local heterogeneities, located in a strict geometrical order and form a structure which reminds a crystal [3, 13, 15]. Such material can be examined as continuous for beams with wavelength much bigger than distance between elements of such structure.

A dielectric crystal which has a periodically modulated positive permittivity and permeability could have properties of left-handed materials [10, 14], which M. Notomi extensively studied in light propagation and the refraction phenomenon in strongly modulated two-dimensional (2D) photonic crystals [8, 11]. Recently, these results have been discussed in the literature [5, 13, 14]. While the conclusions differ, all authors seem to argue that causality must determine the sign of the refractive index.

In this work the theoretical method of the description of coherent light propagation in composite 2D periodic structure is proposed. The proposed model of such specified type is considered in [7], and the results of computer simulation of light scattering by the metamaterial are presented using our approaches.

2. Principles of investigation. To investigate possibilities of negative refraction angles we examined light diffraction on a grating with modulation of dielectric permeability in it (see fig.1). The modulation of dielectric permeability for each grating could be expressed as:

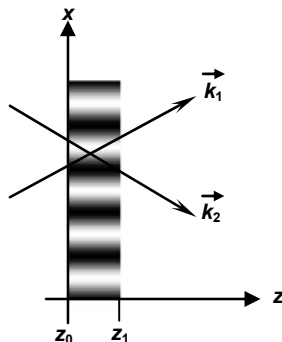


Fig. 1. Dielectric layer with modulated dielectric permeability. k_1 and k_2 are wavevectors of coupled waves

$$\epsilon(x) = \epsilon_c + \Delta_\epsilon(x) = \epsilon_c + \Delta_\epsilon \cos\left(\frac{x}{T} + \varphi\right), \quad (1)$$

where ϵ_c is the average dielectric permeability for the selected layer, Δ_ϵ is permeability modulation depth for layer, T is the period of modulation and φ is initial phase of modulation. We will consider that modulated permeability fills homogeneously each layer, which spatially limited by borders: $z_0 \leq z \leq z_1$. Let the modulation depth of dielectric permeability be much smaller than its average ($\Delta_\epsilon \ll \epsilon_c$), it means that for electric vector of optical wave the next expression is correct:

$$\epsilon \operatorname{div} \vec{E} \approx \operatorname{div}(\epsilon E) = 0. \quad (2)$$

The refracted and deflected light beams may be considered as plane waves, with the angles of refraction (θ_1) and deflection (θ_2):

$$E = A_1(z)e^{j\left(\omega t - \frac{2\pi}{\lambda}(z \cos \theta_1 + x \sin \theta_1)\right)} + A_2(z)e^{j\left(\omega t - \frac{2\pi}{\lambda}(z \cos \theta_2 + x \sin \theta_2)\right)}, \quad (3)$$

where spatial frequencies: $\sin \theta_2 = \sin \theta_1 + \frac{\lambda}{2\pi T}$. Each pair of angles θ_1 and θ_2 corresponds to the pair of coupled waves with the amplitudes A_1 and A_2 . Interaction between these waves is defined by equation of coupled modes [1]:

$$\begin{aligned} \frac{dA_1(z)}{dz} &= -j\kappa A_2(z) \exp(j\eta z) \\ \frac{dA_2(z)}{dz} &= -j\kappa^* A_1(z) \exp(-j\eta z) \end{aligned}, \quad (4)$$

where η is a coefficient of phase synchronism, that can be expressed as:

$$\eta = \frac{2\pi}{\lambda} (\cos \theta_1 - \cos \theta_2), \quad (5)$$

and the complex coupling coefficient: κ is equal to:

$$\kappa = \frac{\omega \Delta_\epsilon}{4c \sqrt{\cos \theta_1 \cos \theta_2}} e^{j\varphi}. \quad (6)$$

The solution of equation (4) can be expressed in the terms of initial amplitudes $A_1(0)$ and $A_2(0)$ in matrix form:

$$\vec{A}(z) \equiv \begin{bmatrix} A_1(z) \\ A_2(z) \end{bmatrix} = \begin{bmatrix} u_{11} & u_{12} \\ u_{21} & u_{22} \end{bmatrix} \cdot \begin{bmatrix} A_1(z_0) \\ A_2(z_0) \end{bmatrix} = \mathbf{U} \vec{A}(z), \quad (7)$$

$$\begin{aligned} u_{11} &= e^{j\frac{\eta}{2}(z-z_0)} \left(\cos(s(z-z_0)) - j\frac{\eta}{2s} \sin(s(z-z_0)) \right) \\ u_{12} &= -j\frac{\kappa}{s} e^{j\frac{\eta}{2}(z+z_0)} \sin(s(z-z_0)) \\ u_{21} &= -j\frac{\kappa^*}{s} e^{-j\frac{\eta}{2}(z+z_0)} \sin(s(z-z_0)) \\ u_{22} &= e^{-j\frac{\eta}{2}(z-z_0)} \left(\cos(s(z-z_0)) + j\frac{\eta}{2s} \sin(s(z-z_0)) \right) \end{aligned}, \quad (8)$$

where parameter s is the displaced absolute value the coefficient of mode coupling:

$$s^2 = \frac{\eta^2}{4} + |\kappa|^2. \quad (9)$$

The matrix \mathbf{U} is regarded as the transfer function, which depends on initial and actual coordinates with cou-

pling coefficient: $\mathbf{U} = \mathbf{U}(z, z_0, \kappa)$. In the finish point $z = z_1$ matrix \mathbf{U} becomes complex transfer function of the layer.

According to (3) and (7) in the area of interaction two waves are propagating and periodically exchange their powers, but their total power stays constant. If initial amplitudes are equal to $A_1(z_0) = 1, A_2(z_0) = 0$ then:

$$\begin{aligned} |A_1(z)|^2 &= \cos^2(s(z-z_0)) + \left(\frac{\eta}{2s}\right)^2 \sin^2(s(z-z_0)) \\ |A_2(z)|^2 &= \frac{|\kappa|^2}{s^2} \sin^2(s(z-z_0)) \\ |A_1(z)|^2 + |A_2(z)|^2 &= 1 \end{aligned} \quad (10)$$

The part of energy which is used for exchanging between modes is determined by the values of mode coupling coefficient and coefficient of phase synchronism [19]:

$$\max \frac{|A_1(z)|^2 - |A_2(z)|^2}{|A_1(z)|^2 + |A_2(z)|^2} = \frac{|\kappa|^2}{s^2} = \left(1 + \frac{\eta^2}{4|\kappa|^2}\right)^{-1} \quad (11)$$

As one can see the full power exchange is limited by conditions when $\eta = 0$. It means that light beam in 2D layer could be deflected without power loose in the direction which defined by the incident beam direction. In [7] showed that in the system of two serial modulated layers the mentioned restrictions could be remove.

Multilayer material (see fig. 2) with the following modulation of dielectric permeability:

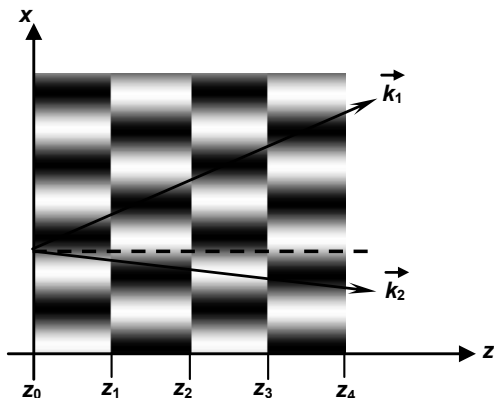


Fig. 2. The scheme of light transformation by the layered structure with modulated dielectric permeability

$$\varepsilon = \begin{cases} \varepsilon_c + \Delta_{\varepsilon,1} \cos\left(\frac{x}{T} + \varphi_1\right), & z_0 < z < z_1 \\ \varepsilon_c + \Delta_{\varepsilon,2} \cos\left(\frac{x}{T} + \varphi_2\right), & z_1 < z < z_2 \\ \dots\dots\dots \\ \varepsilon_c + \Delta_{\varepsilon,n} \cos\left(\frac{x}{T} + \varphi_n\right), & z_{n-1} < z < z_n \end{cases} \quad (12)$$

here φ_i is the initial phase of dielectric permeability modulation. The length of layer interaction is l_i , where i is the number of layer. Such layered structure transforms incident light according to the next equation:

$$\bar{A}_{out} = \mathbf{U}^n \cdot \mathbf{U}^{n-1} \dots \mathbf{U}^1 \cdot \bar{A}(z_0) \equiv \mathbf{W}\bar{A}(z_0), \quad (13)$$

where matrix \mathbf{U}^n corresponds to the layer number i . If the incident beam is described by vector $[A(0), 0]$, the transfer function is defined by nondiagonal element of matrix \mathbf{W} :

$$H = \frac{|A_{out,1}|^2}{|A_{0,1}|^2} = |w_{10}|^2, \quad (14)$$

Transfer function for each two layers (14) in terms of (8) an (13) can be expressed as [7]:

$$H(Q_1, Q_2, \phi; h) = |Q_1 \operatorname{sinc} \xi_1 (\cos \xi_2 + jh \operatorname{sinc} \xi_2)| + e^{j(2h+\phi)} Q_2 \operatorname{sinc} \xi_2 (\cos \xi_1 - jh \operatorname{sinc} \xi_1) \quad (15)$$

where:

$$\begin{aligned} Q_{1,2} &= \frac{\kappa \sqrt{l_1 l_2}}{2} \cos \theta_{2,1} \\ h &= \frac{\eta \sqrt{l_1 l_2}}{2} \\ \xi_{1,2} &= \sqrt{h^2 + Q_{1,2}^2} \end{aligned} \quad (16)$$

ϕ is the phase difference between the layer modulations. Transfer characteristic H is the function of phase difference and coefficients Q_1 and Q_2 determined by the modulation depth. Phase mismatching coefficient h must be thread as the parameter, determined by the deflecting angle θ_1 (5). It was considered that optimal values of Q_1, Q_2 and ϕ giving the maximum of H for each certain value of $h(\theta_1)$.

Using expressions (8), (12) and (3), it is possible to define the components of the field vector of scattered wave in the layered structure and to determine the optimal parameters of layer distance and depth of dielectric permeability modulation is used expressions (15) and (16).

3. Results and discussion. A model of 2D crystal with different layers was used to demonstrate the negative refraction. The model of structure is showed on fig. 2, effective distance between layers is equal to wavelength ($d = \lambda/2$), step of periodicity is $T = \lambda/3$, number of layers is 32. The angle of refraction could be determined by observing the distance between the entry and leaving points, the result of the refraction calculations are shown on fig.3.

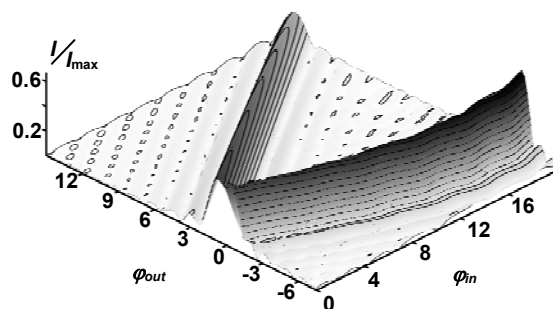


Fig. 3. The dependencies of the refraction angle for the composite structure

As can be seen from these graphs for 32 layers the refraction angle becomes negative (for general intensity of the wave), and according to Snell's law it is possible to show that refraction index is negative too. So if the number of layers is increasing ($n \rightarrow \infty$) the intensity in positive direction is decreasing and material becomes completely left-handed.

This work is done with the partial support of the Ministry of Education and Science of Ukraine (grant M/175-2007).

1. Balakshij V.I., Parygin V.N., Chirkov L.E. Physical properties of acousto-optics / edited by Parygin V.N. – Radio i Sviaz, Moscow, 1985.
 2. Chen Y.-F., Fischer P., Wise F.W. Negative refraction at optical frequencies in nonmagnetic two-component molecular media // Phys. Rev. Lett. – 2005 – Vol. 95, No.6.
 3. Dewar G. Candidates for $\mu < 0$, $\epsilon < 0$ nanostructures // Int. Jour. Of Mod. Phys. B – 2001 – Vol. 15, Nos. 24&25.
 4. Eleftheriades G. V., Iyer A. K., Kremer P. C. Planar negative refractive index media using periodically L-C loaded transmission lines // IEEE Trans. Microwave Theory Tech. – 2002 – Vol. 50, No12.
 5. Hong J., WeiHu X., Liu M.-H., Yan B.-R. Kong L.H. Negative refraction of a double L-shaped metamaterial // J. Opt. A: Pure Appl. Opt. – 2009 – Vol. 11. 6.
 6. Katsarakis N., Konstantinidis G., Kostopoulos A., Penciu R.S., Gundogdu T.F., Koschny Th., Kafesaki M., Economou E.N., Soukoulis C.M. Magnetic response of split-ring resonators in the far infrared frequency regime // Opt. Lett. – 2005 – Vol. 30.
 7. Kisi A.V., Kovalenko A.V., Kurashov V.N. Diffraction efficiency optimization of Bragg deflectors with phased acoustic arrays // SPIE Proc. – 1993 – Vol. 2108.
 8. Kosaka H., Kawashima T., Tomita A., Notomi M., Tamamura T., Sato T., Kawakami S. Superprism phenomena in photonic crystals // Phys. Rev. B – 1998 – Vol. 58.
 9. Linden S., Enkrich C., Wegener M., Zhou J., Koschny T., Soukoulis C.M. Magnetic response of metamaterials at 100 Terahertz // Science – 2004 – Vol. 306.
 10. Notomi M. Theory of light propagation in strongly modulated photonic crystals: Refractionlike behavior in

the vicinity of the photonic band gap // Phys. Rev. B – 2000 – Vol. 62, No. 10.
 11. Notomi M., Tamamura T., Ohtera Y., Hanaizumi O., Kawakami S. Direct visualization of photonic band structure for three-dimensional photonic crystals // Phys. Rev. B – 2000 – Vol. 61, No. 7.
 12. Pendry J.B., Holden A.J., Robbins D.J., Stewart W.J. Magnetism from conductors and enhanced nonlinear phenomena // IEEE Trans. Microw. Theory Techniques. – 1999. – Vol.47. 13.
 13. Pendry J.B., Martin-Moreno L., Garcia-Vidal F.J. Mimicking surface plasmons with structured surfaces // Science – 2004 – Vol. 305.
 14. Ritke S., Kristensson G., Anderson M. Propagation in bianisotropic media – reflection and transmission // IEE Proc. – Microw. Antennas Prop. – 2001 – Vol. 148, No. 1.
 15. Shelby R.A., Smith D.R., Schultz S. Experimental Verification of a Negative Index of Refraction // Science – 2000 – Vol.292.
 16. Skaar J. Fresnel equations and the refractive index of active media // Phys. Rev. E – 2006 – Vol. 73.
 17. Smith D.R., Padilla W.J., Vier D.C., Nemat-Nasser S.C., Schultz S. Composite medium with simultaneously negative permeability and permittivity // Phys. Rev. Lett. – 2000 – Vol. 84, No.18.
 18. Veselago V.G. The electrodynamics of substances with simultaneously negative ϵ and μ // Sov. Phys. Usp. – 1968 – Vol. 10, No.4.
 19. Yariv A., Yeh P. Optical Waves in Crystals: Propagation and Control of Laser Radiation / edited by Yariv A. – John Wiley and Sons, 1984.
 20. Yen T.J., Padilla W.J., Fang N., Vier D.C., Smith D.R., Pendry J.B., Basov D. N., Zhang X. Terahertz magnetic response from artificial materials // Science – 2004 – Vol. 303.

Received by editorial board on 21.10.09

UDC 535.31; 53.082.5; 681.7.08

N. Goloborodko, post graduate, D. Podanchuk, Ph.D.,
 V. Dan'ko, advanced engineer,
 A. Goloborodko, Ph.D., M. Kotov, advanced engineer

WAVEFRONT SCANNER FOR DETECTING SURFACE INHOMOGENEITIES

Безконтактна діагностика поверхні може бути проведена оптичними методами шляхом аналізу хвильового фронту лазерного пучка, відбитого від зразка. Пропонується сканер хвильового фронту, який має чутливість та вимірний діапазон на порядок кращі за сенсор Шека-Хартмана. Представлені результати детектування сканером хвильового фронту тестових поверхонь різної структури.

Ключові слова: сенсор хвильового фронту Шека-Хартмана, сканер хвильового фронту, дослідження поверхні.

Non-contact diagnostics of the surface may be realized with optical methods by analyzing the wave front of laser beam reflected from the sample. Wavefront scanner that provides the sensitivity and measurement range by order of magnitude greater than the Shack-Hartmann sensor is proposed. The results of detecting test surfaces with different structure by the wavefront scanner are presented.

Key words: Shack-Hartmann wavefront sensor, wavefront scanner, surface measurements.

Introduction. Recently the problem of non-contact diagnostics became extremely urgent. The optical methods of investigating the structured objects provide measuring and analyzing the wave front of the laser beam reflected from its surface. The most effective for such kind of investigations is the direct measuring of the wavefront by sensors that are widely used in adaptive optics [6]. This method is used for the lenses and mirrors, for tive control and in ophthalmology [7]. It allows not only the direct measuring of the wavefront but also its adjusting in real time.

Among the wavefront sensors the Shack-Hartmann sensor should be mentioned as the most used. The principle of its work is well known [1]. The lenslet array is situated in the plane conjugated with the tested wavefront plane and each lenslet divides the wavefront in local areas. If the tested wavefront is plane then each lenslet forms the source image in the focus. If the wavefront is nonuniform the tilted wave is incident on lenslet and as a result the image is displaced relatively to the optical axes in the focal plane. The image displacements in the first approximation are directly connected with the wavefront slope angle. The attractive feature of the sensor is the ability to measure slopes in X and Y directions simultaneously. As a matter of fact the Shack-Hartmann sensor requires using the reference plane wave, which is produced by the reference source and is aimed for the accurate calibration of the lenslet arrays focuses positions.

The main obstacle in the sensors application for the precision monitoring of the surface is their insufficient spatial resolution that is determined by lenslet size. One of the

methods for solving this problem is the use of the focused laser beam which after reflection from the tested surface passes through the same optical scheme and gets to the sensor [3]. In this case the signal formed in the sensor plane can be treated as the phase image of the surface subarea and the spatial resolution is determined only by the sensors aperture [2]. Though in the case of measuring with this scheme the tested wavefront is almost plane that requires high spatial sensitivity of the device that can't be always provided by the sensor.

The alternative to this can be the wavefront scanner [4; 5] that differs from the sensor in the fact that the lenslet array is replaced by one lens with longer focal distance and with controlled entrance aperture. Owing to this the angular sensitivity of the scanner can be sufficiently enlarged. This paper is concerned with the comparison analysis of the sensor and scanner and shows experimental results of detecting the tested surface features with the wavefront scanner.

Experimental setup and measurement principles.

The optical scheme of the experimental setup used for the surface investigations is shown on fig. 1. Plane wave from the He-Ne laser ($\lambda=0,63 \mu\text{m}$) after the circular aperture D1 is divided into two beams. The laser beam intensity is adjusted by the polarization attenuator that consists of the P1 and P2 polarizers. The wave reflected from the beam splitter BS1 is incident on the reference mirror, reflects from its surface and goes back to the system and forms the reference beam. The wave that passes through the beam splitter BS1 is focused on the surface of reflective object by the microscope objective L5. The system of L1–L5 lenses and

BS1–BS2 beam splitters transposes the samples plane into the object plane of the microscope M, which is used for visual control of the beam's focusing on the tested surface. The sample is fixed on the table with computer control and can be moved in two orthogonal directions in the plane normal to the beam axis. Though it's able to scan the surface with the step of about $10\ \mu\text{m}$ and several millimeters in aperture. The focused spot size can vary from 5 to $30\ \mu\text{m}$ depending on the D1 aperture size. The beam reflected from the sample after re-passing the microscope objective L5 forms the object wavefront that is transposed into the object plane of the scanner by the 4F system of long-focus lenses L2–L3 and BS1 mirror. Scanner consists of the controlled diaphragm D2 (0,5 mm in diameter), the lens L4 (focal length 200 mm) and the CCD photodetector CCD2.

In addition the object wavefront is transposed into the inlet plane of the wavefront sensor (which consists of the refractive lenslet array RLA and the CCD photodetector CCD1) by the BS3 mirror. The lenslet size is $0.4\times 0.4\ \text{mm}$ and its focal length is 24 mm. Photodetectors CCD1 and

CCD2 are identical (CCD cameras Sanyo VCB-3385P) and their resolution is 752×582 pixels, each pixel is $6.25\times 6.25\ \mu\text{m}$.

The D2 diaphragm can be displaced in the plane normal to the beam and can be controlled by the computer.

For the D2 diaphragm displacement the two-coordinate device with the scan step of 0.19 mm and $15\times 15\ \text{mm}$ aperture was developed (fig.2). It consists of two steel plates 1 and 5 on which the stepping motors 2 and 6 are mounted and with the help of spindles with screw thread they move carriages 4 and 8. The 1 plate is mounted on the experimental setup so that the moving carriage 4 could move horizontally. The 5 plate is fastened on the moving carriage 4 so that the stepping motors axes were orthogonal. Thus the moving carriage 8 can move horizontally (X axis) by the stepping motor 2 and can be moved vertically by the stepping motor 6. The diaphragm holder is mounted on the moving carriage 8. The control of the carriages moving into the initial state is made by optoelectronic sensors 3 and 7.

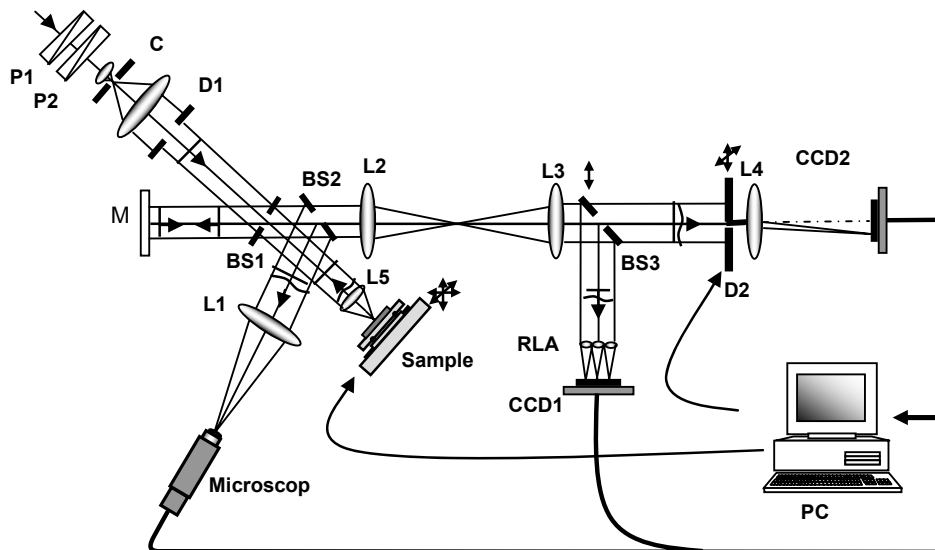


Fig. 1. Optical scheme of the experimental setup

The stepping motors moving control is made via the parallel port of the personal computer (PC) by the developed controller and software.

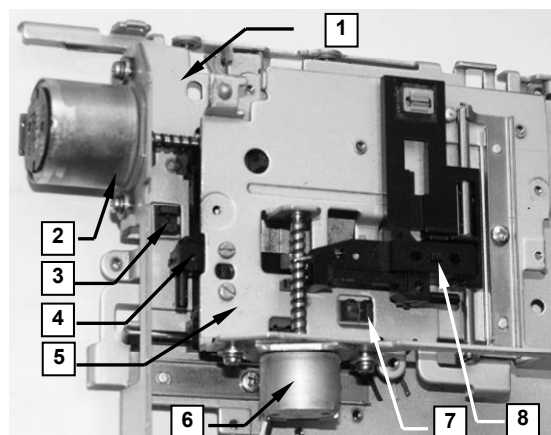


Fig. 2. The appearance of the two-coordinate device for the wavefront scanner aperture controlling (front view)

Results and discussion. For comparison of the sensor and scanner measurement abilities the test wavefronts were measured. The test wavefronts were made by the test plane mirror that is mounted on the table with micrometer

screw instead of the sample. Then the mirrors displacement along the system optical axis leads to generation of the spherical wavefronts with controlled curvature.

The comparison of the sensor and scanner measurement abilities was made by the local slopes values in some wavefront subaperture that was set in the next way.

An additional diaphragm which was placed after the L3 lens picks out a part of the wavefront that corresponds to the lenslet from the sensors lenslet array. Then the wavefront scanner diaphragm is installed in the corresponding subaperture. After that the additional diaphragm is extracted from the system. Thus displacing the table with the micrometer screw the test wave fronts with controlled curvature are achieved.

The local slope measurements started from the minimal displacements of the test mirror (the minimal wavefront curvature that can be sensed by sensor and scanner) and lasted till the maximal displacements (the maximal wavefront curvature that can be measured by sensor and scanner).

The errors analysis of the sensor and scanner measurements was provided the next way. 5 realizations for two local slopes were analyzed. Fig. 4 shows local slopes deviations from the average value for 5 realisations measured by sensor and scanner.

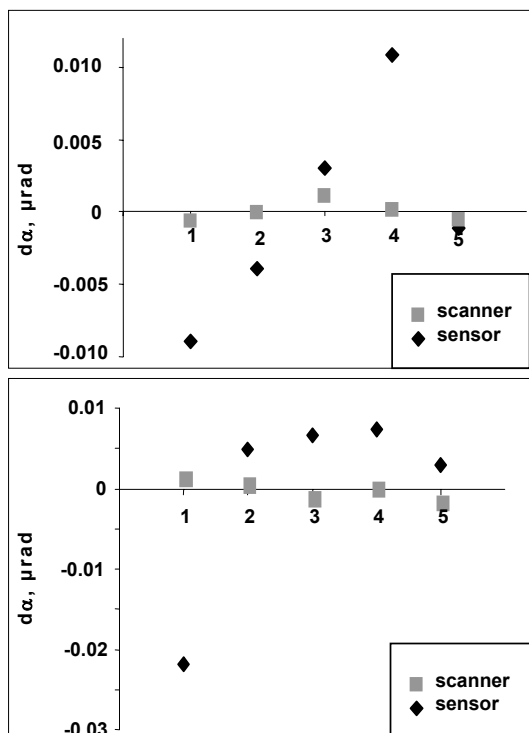


Fig. 4. Local slopes deviations measured by sensor and scanner from the average value of the local slope of $\alpha_1=0.18$ mrad (on top) and $\alpha_2=0.07$ mrad (on the bottom)

The standart deviation of the local slopes measurement was evaluated for two angles – $\alpha_1=0.18$ mrad and $\alpha_2=0.07$ mrad and has a value of:

0.015 mrad for sensor and 0.003 mrad for scanner for the first angle

0.025 mrad for sensor and 0.003 mrad for scanner for the second angle.

The deviation of local slopes values for the sensor is 0.75% and 1.23% for α_1 and α_2 respectively, and 0.07% and 0.12% for the scanner. As one can see the measurement error for scanner is by order of magnitude smaller than for sensor.

For measuring the maximal wavefront local slope the test mirror was displaced at the distance for which the object spot on the hartmanogram and on the working area of the scanner was on the edge of the aperture.

As it was discovered the maximal measured angle for sensor and scanner is almost the same. It is caused by the specific of the experimental setup. For sensor the spot size on the hartmanogram is 10 pixels and the working area is about 30 pixels. For the scanner the working area is 340 pixels, which is sufficiently bigger then for the

sensor, but the spot size is also bigger and has a value of 80 pixels. Since the maximal angle is proportional to the relation of the lenslet focal length to the working area size and for the proposed sensor and scanner $A_{scan}/F_{scan} \sim a_{sens}/f_{sens}$ so the maximal local slope for sensor and scanner is almost the same and has a value of 8 mrad for the sensor and 10 mrad for the scanner.

However the measurement range of the scanner is bigger then for the scanner because the minimal angle is proportional to the measurement accuracy that for the scanner is much bigger (0,003 mrad), than for the sensor (0,022 mrad).

The test object (a glass plate with a photoresist layer with etched computer-generated structures on it) was scanned by the wavefront scanner described above.

For the testing there were chosen the next structures (Fig. 5) with depth of etching of 0.32 μm :

1. stripes with different width (the focused beam lied on the stripe 2.8 μm wide);
2. periodically positioned pits with 2 μm in diameter and 3.2 μm period (size of the structure's square is 50x50 mm).

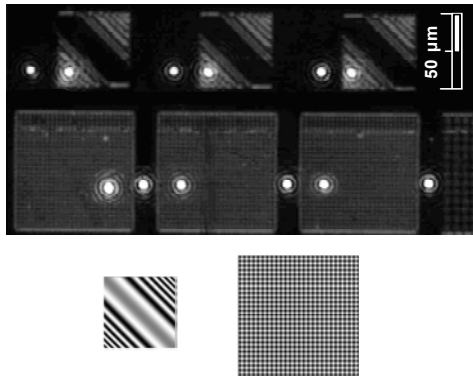


Fig. 5. The tested surface (on top) and computer-generated picture of the structures (on the bottom)

Results of this experiment are represented on fig. 6 which shows the measured local slopes values of the wavefront reflected from clear surface and three spots on the mentioned structures for each subaperture of the wavefront where the measurements were made. The numbers of subapertures are denoted along the x axis.

The tested wavefronts were compared to the plane wavefront reflected from the reference plane mirror M.

As one can see from fig. 6 measured local slopes values for each subaperture for structured and clear surface as a rule differ within the error that is 0,003 mrad for the scanner. It should be mentioned that the scatter of the measured values for the first structure and clear surface has some kind of correlation appearance. And otherwise for the second structure and clear surface this scatter is more random.

Quantitatively the order of difference between the object and reference (plane) wavefronts can be evaluated as the local slopes standard deviation within the tested subaperture. The values of wavefront local slope standard deviations within the overall aperture for the x axis and for two types of test structures are shown on fig.7. As one can see the wavefront local slope standard deviation within the overall aperture for the x axis is 28.2 mrad for the second structure and 11.8 mrad for the clear surface, that is twice smaller than for the structure. For the first structure there is no such a relation and the wavefront local slope standard deviation for the structure is 14.2 mrad and 10.8 mrad for the clear surface.

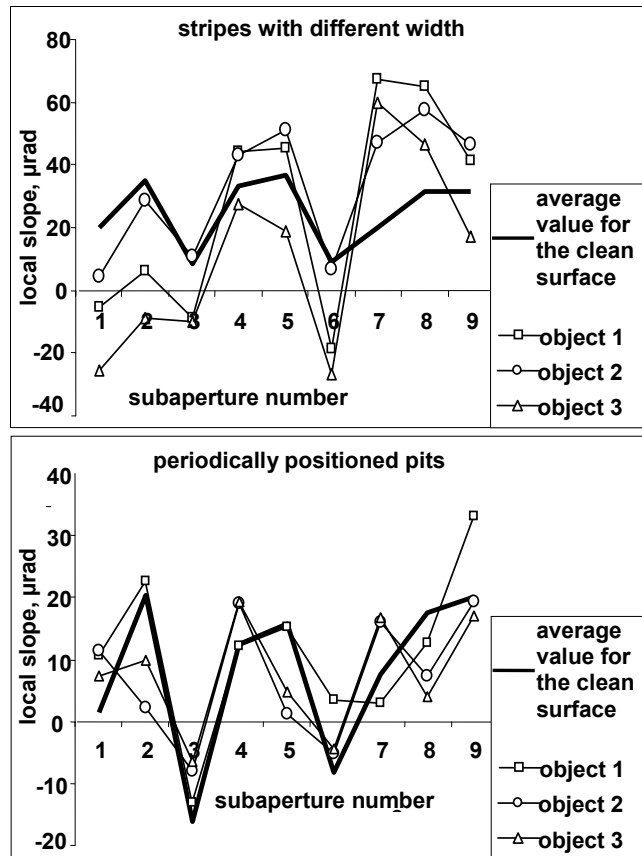


Fig. 6. Wavefront local slopes values, reflected from the clean surface and from three spots on the structures with stripes with different width (on top) and periodically positioned pits (at the bottom)

As one can see even though the average values of standard deviation differ but with bigger certainty one can separate surface types only for the second structure (stripes with different width) since some spots coincide for the first structure (within the mentioned error).

It can be supposed that for the first structure with periodically positioned pits the proposed method don't allow to separate clear surface from structure because the focused spot covers too many elements of structure. Hence there is an additional pseudo noise phase incursion that corresponds

to the wave scattering on mentioned inhomogeneities. So the data for each of three object spots is of a little difference it means that the measurement result slightly depends on the spot position on the structure. And for the second structure the focused spot covers only 1 or 2 stripes and the additional phase incursion that corresponds to the wave scattering is absent. Moreover the data for three spots on the surface differs, i.e. the data depends on the spot position on the surface so one can separate clear surface from the structure on it that is obvious from the represented results.

Conclusions. The wavefront scanner for investigating the structured objects by measuring and analyzing the wave front of the laser beam reflected from its surface is proposed. The developed scanner allows measuring the wavefront local slopes with accidental error of 3 μ rad that is by one order of magnitude smaller than for the wavefront sensor.

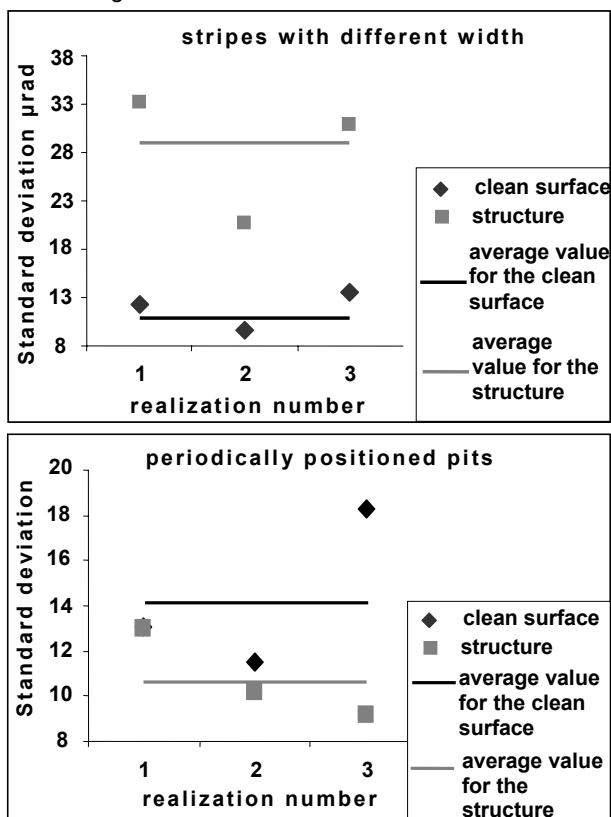


Fig. 7. Values of wavefront local slope standard deviations within the overall aperture for the x axis and for two types of test structures – with stripes with different width (on top) and periodically positioned pits (at the bottom)

UDC 535.621.3

A. Goriachko, assist. prof., A. Kovalenko, assist. prof., V. Kurashov, asoc. prof., A. Shchyrba, stud.

EXPERIMENTAL INVESTIGATIONS OF INTRINSIC ROUGHNESS AT THE SURFACE OF AIR-CLAD OPTICAL FIBERS

In this work, we have investigated losses in the air-clad optical fibers, caused by surface irregularities formed in the process of fiber manufacturing. These irregularities are described by the model of the frozen surface capillary waves. We have verified if the theoretical model of roughness corresponds to the real surface relief of the air-clad optical waveguide. Our experimental results are in good agreement with theoretical calculations, clearly demonstrating that the major mechanism of losses in the air-clad fibers is scattering at frozen surface capillary waves.

Key words: nanofiber, surface scattering, surface capillary waves, atomic force microscopy.

В даній роботі було досліджено втрати в безоболонкових оптичних хвилеводах, обумовлені поверхневими неоднорідностями, що формуються в процесі виготовлення хвилеводів. Ці неоднорідності описуються моделлю заморожених поверхневих капілярних хвиль. Було перевірено відповідність теоретичної моделі шорсткості реальному рельєфу поверхні безоболонкового оптичного хвилеводу. Експериментальні результати добре узгоджуються з теоретичними розрахунками, показано, що основним джерелом втрат є розсіяння на заморожених поверхневих капілярних хвилях.

Ключові слова: нановолокно, поверхнєве розсіяння, поверхневі капілярні хвилі, атомно-силова мікроскопія.

Air-clad optical nanofibers are attracting a great deal of attention [1; 6]. They can be useful in nanoelectronics as interconnects between separate integrated circuits, as building blocks of various photonic devices, and also as environmental sensors based on the distribution of the near-surface field, which is concentrated outside the waveguide, thus effectively interacting with the fiber's environment. One of the tasks to be solved on the way towards

The test objects investigation showed the scanner ability to detect surface inhomogeneities the structure of which is smaller than the focused spot size and has the maximal depth of 0.32 μ m and the appearance of stripes with different spatial frequencies.

This work is done with the partial support of the Ministry of Education and Science of Ukraine (grant M/175-2007).

1. Curatu C., Curatu G., Rolland J. Fundamental and specific steps in Shack-Hartmann wavefront sensor design // Proc. of SPIE. – 2006. – Vol. 6288. – pp. 628801.
2. Goloborodko A.A., Grygoruk V.I., Kotov M.M., et al. Determination of local surface defects using a Shack-Hartmann wavefront sensor // Ukrainian Journal of Physics. – 2008. – Vol.53, N 10. – P.946-951.
3. Kotov M.M., Kurashov V.N., Podanchuk D.V., et al. Surface defective structure detection with Shack-Hartmann wavefront sensor // Bulletin of the University of Kiev. Series: Physics & Mathematics. – 2006. – Vol. 3 – P. 341-348.
4. Kotov M.M., Podanchuk D.V., Sutyagina N.S., et al. Wavefront scanner for testing the surface of optical elements // Proc. of the VIII International Young Scientists' Conference on Applied Physics, Kyiv, June 2008. – P. 192.
5. Laude V., Oliver S., Dirson C., et al. Hartmann wave-front scanner // Optics Letters. – 1999. – Vol. 24, № 24. – P.1796-1798.
6. Rousset G. Wavefront sensing // Adaptive Optics for Astronomy / Ed. by D.M. Alloin and J.-M. Mariotti. – Dordrecht – Boston – London, 1994.
7. Thibos L. Principles of Hartmann-Shack aberrometry // Journal of Refractive Surgery. – 2000. – Vol. 16, September/October. – P. 563-565.

Received by editorial board on 19.06.09

practical applications of these fibers is estimation and reduction of the energy losses in the process of optical signal propagation. It is believed that the limiting source of losses in the optical fibers is formation of the irregularly surface relief forming due to excitation and subsequent freezing of surface capillary waves (SCW) [2; 7; 8] during fiber manufacturing [3]. This is caused by thermodynamics of equilibrium states, thus can not be avoided by technological

means [7]. Therefore, radiation losses on the perturbed surface are of fundamental nature and are inherent to many types of sharply directional optical guides. Theoretical estimates of the losses caused by the arbitrary surface relief [1], are in qualitative agreement with experimental data [7], in particular, displaying typical dependence on the fiber's diameter, but exhibiting an order of magnitude discrepancy in the absolute loss value for single mode light propagation. Therefore, it is interesting to investigate experimentally the statistical characteristics of the arbitrary relief fluctuations, which exist on the surface of the air-clad optical fiber, and to verify their compliance with the SCW model. The atomic force microscopy (AFM) technique is well suited for this task and was applied in this work to study the nanometer scale irregularities of the fiber's surface.

Surface scattering in air-clad optical guides. A theoretical analysis of the light scattering by the rough surface of the optical waveguide is performed within the framework of the Marcuse model, frequently utilizing the equivalent current sources formalism [4]. Maxwell equations for inhomogeneous media in the first approximation of perturbation theory possess solutions in the form of linear relation between the average scattered power and the spectral density of the refraction index fluctuation power. The perturbation of the guide's surface is considered equivalent to refraction index perturbations, having a fragmented function form with fluctuation magnitude as an argument. Since such relation can not be linearized, the power radiated by the arbitrary surface must depend nonlinearly on spectral density of the surface relief's power even in the first approximation of the perturbation theory. Physically this means that the given solution neglects the part of the fluctuation power, proportional to the low frequency components of the arbitrary surface spectrum. If the latter is inverse proportional to spatial frequency [2; 5], then the difference in refraction indexes for the core and the cladding is of the order unity, leading to substantial scattering at low frequencies. This circumstance is the major concern of the recently appeared work [3]. There, a model is developed, describing equivalent fluctuations of refraction index and a relation is obtained between these fluctuations' correlation functions and those of the surface relief.

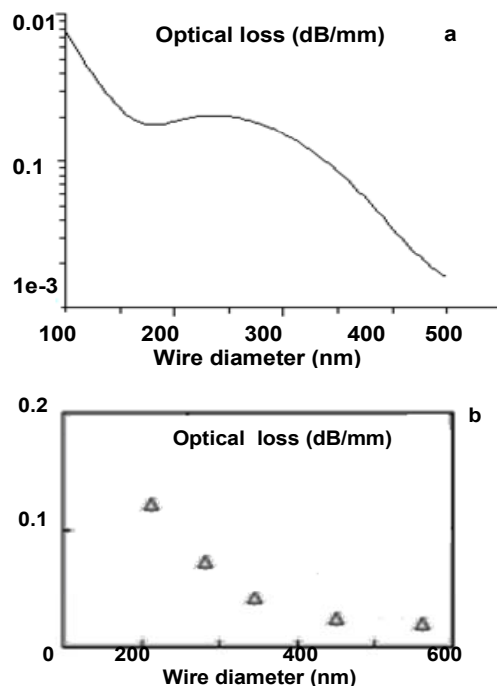


Fig. 1. The loss coefficient for the quartz nanofiber as a function of its diameter. a- theory [3]; b- experiment [7]

The above mentioned relation also takes into account the nonlinear transformation of the surface relief. In a waveguide of high refraction index profile, both linear and nonlinear perturbation components are of similar order and produce two meaningful constituents of the total radiation loss. Within this framework, the major result for quartz nanofibers is given in fig. 1a. Similar experimental results are presented in fig. 1b [7].

Obviously, there exists a substantial discrepancy in the loss coefficients' absolute values, which is hard to explain by experimental errors or drawbacks of theory. We believe that the only probable source of additional losses, which are observed in air-clad nanofibers, is some other mechanism of surface irregularities formation, not taken into account by the SCW theory. The spectral density $S(\nu)$ of such a relief depends on the spatial frequency ν : $S(\nu) \sim 1/\nu$ (for a flat surface) with a dispersion of several Angstrom. The field scattering in the near-surface region of the fiber can be also caused by other factors, in particular, by dust particles deposited at the surface-air interface. In this case, however, the relief's spectrum will most probably have a different dependence on frequency as well as different values of fluctuation parameters, which can be unearthed by direct experimental measurements.

Experimental. The air-clad optical fiber, investigated in our work, was $\sim 50 \mu\text{m}$ in diameter. The fiber was thoroughly cleaned by ultrasound in acetone and carefully fixed to a specially designed sample holder. The AFM investigation was performed in non-contact mode with NT-MDT Integra instrument. We have used the AFM cantilevers with the following typical characteristics: $130 \pm 5 \mu\text{m}$ length, $35 \pm 5 \mu\text{m}$ width, $1.7 - 2.3 \mu\text{m}$ thickness, $10 - 15 \mu\text{m}$ tip height, $\leq 22^\circ$ tip cone angle, 10 nm tip curvature radius, $115 - 190 \text{ kHz}$ resonant frequency. The AFM imaging had certain limitations due to the fiber surface curvature and the conical shape of the tip. Useful data could only be obtained at the fiber's top and with image size substantially smaller than the fiber's diameter. When these conditions are not met, the shank of the AFM tip or even the cantilever itself would contact the fiber's surface, producing imaging artifacts. Fig. 2 shows the largest useful images of the fiber. The image in (a) was obtained for the as-received fiber, one notices an intensive contamination, most probably by dust and grease. The image in (b) was obtained after cleaning in the ultrasonic bath, which has clearly removed contaminations resulting handling.

The images used for statistical analysis were typically much smaller than those in Fig. 2. A small area on the surface was selected and imaged with nanometer precision. A second order background was subtracted for better visual perception of surface topography. An example of the resulting image is shown in Fig. 3a. Ultimately, this is a map of the fiber surface deviation from ideal cylindrical shape. The horizontal line within the image defines the location of the cross-section shown in Fig. 3b. Numerous cross-sections like this one were obtained in different locations on the sample. A total of $N = 35$ cross-sections, each containing 1024 image pixels along the line were used for further statistical averaging.

Results and discussion. The numeric parameters of relief fluctuations were calculated directly from the cross-sections, like the one shown above, by means of averaging over N realizations: $\sigma^2 = \left\langle (x - \langle x \rangle)^2 \right\rangle_{\{N\}}$. The root mean

square deviation obtained in this way was $\sigma = 0.55 \text{ nm}$. A theoretical value for typical quartz fiber manufacturing parameters (temperature of the melt $T \sim 1500\text{K}$, surface tension $\gamma = 0.3 \text{ J/m}^2$) is $\sigma_T = 0.5 \text{ nm}$ [2]. The experimental value is obviously in line with the SCW model.

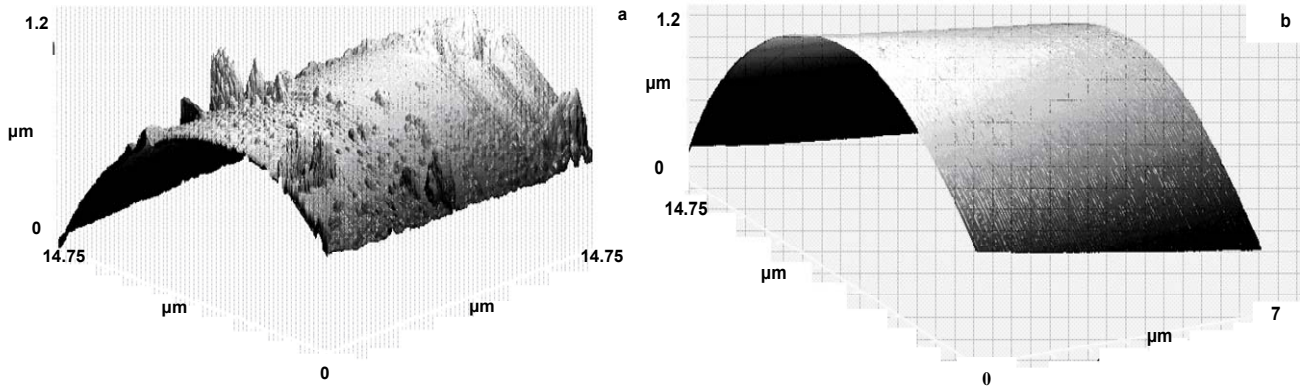


Fig. 2. AFM images of the fiber's surface. a – before cleaning; b – after cleaning

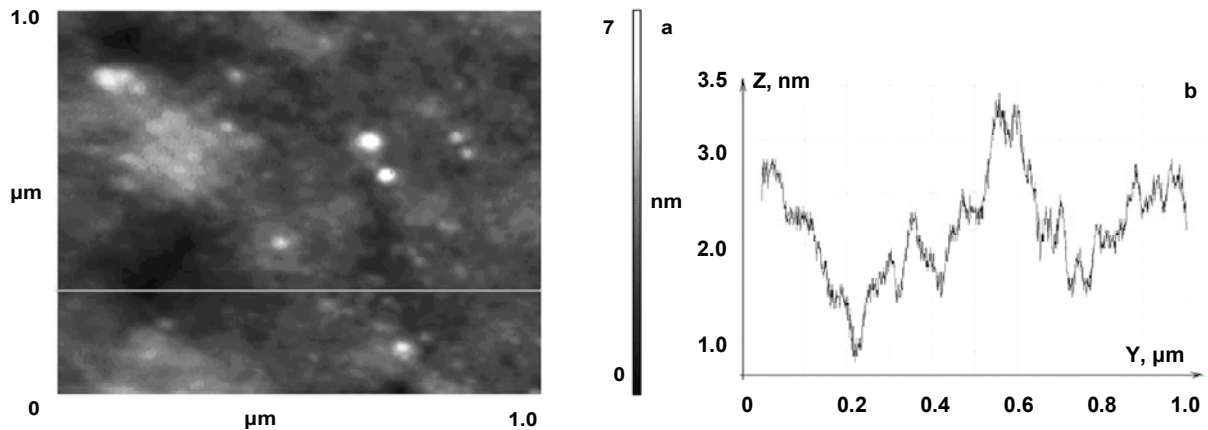


Fig. 3. AFM image of the fiber's surface after second order background subtraction. a – AFM image of the fiber's surface, 1 μm x 1 μm; b – cross-section along the horizontal line, marked in a

A more detailed indication of the SCW model applicability can be obtained from the spectral density of the relief's fluctuations power spectrum $S(\nu)$. To calculate the latter for each selected realization we took the magnitude spectrum and averaged over entire ensemble:

$$\begin{aligned} \tilde{S}(\nu) &= \frac{1}{T} \langle |\tilde{u}(\nu)|^2 \rangle_{\{N\}}; \\ \tilde{u}_r(\nu) &= \frac{1}{\sqrt{2}} \int_{-\frac{T}{2}}^{\frac{T}{2}} u(t) e^{i2\pi\nu t} dt \end{aligned} \quad (1)$$

Since the SCW model assumes the inverse proportional dependence $S(\nu)$, we have linearized the data by representation at the dual logarithmic scale (see Fig. 4). The inhomogeneities of the fiber's surface are just several nm in height. Considering the diameter of the fiber $\sim 50 \mu\text{m}$, one could use the approximation of the flat two-dimensional surface, for which we can write [5]:

$$S(\nu) = \frac{k_b T}{\nu} \quad (2)$$

k_b is the Boltzmann's constant.

To provide a comparison with the expected dependence, the regression line equation was calculated from experimental values using the least squares method:

$$\lg(Y) = -1.21 \lg(X) - 3.00 \quad (3)$$

This is equivalent to the following estimate of the spectral density:

$$\tilde{S}(\nu) \approx \frac{A}{\nu^{1.21}} \quad (4)$$

The determination coefficient of the obtained interpolation is $R=0.97$, indicating a high reliability of the adopted approximation. The obtained dependency (4) is rather close with that expected from the SCW model, yet they differ noticeably. This difference can not be explained by errors of our measurement, since averaging was performed over a significant ($N=35$) number of arbitrary relief realizations. Thus, our arbitrary error should be rather small. Also, this difference can not be explained by the surface curvature. The waveguide's parameters in our case produce a correction, which takes into account the surface curvature, but does not lead to expected changes of the spectrum. Most probably, this difference between theory and experiment can be explained by contribution of point defects and insignificant amounts of dust particles, which remain on the surface even after the ultrasonic cleaning. A widely accepted model for such defects is a stochastic transient uncorrelated Poisson process, with a Lorentzian shaped spectral density:

$$S(\nu) \sim \frac{1}{\nu^2 + \nu_0^2} \quad (5)$$

However, this conclusion clearly requires further experimental and theoretical investigations.

To summarize, our experimental investigations demonstrate that the major contribution into the surface relief's fluctuation of the air-clad optical fiber is indeed governed by the SCW model. However, additional sources of fluctua-

tions can not be excluded. They might change the resulting spectral density and cause an increase of loss coefficient.

This work was supported by the Fundamental Researches State Fund, Project No. Ф29.1/033.

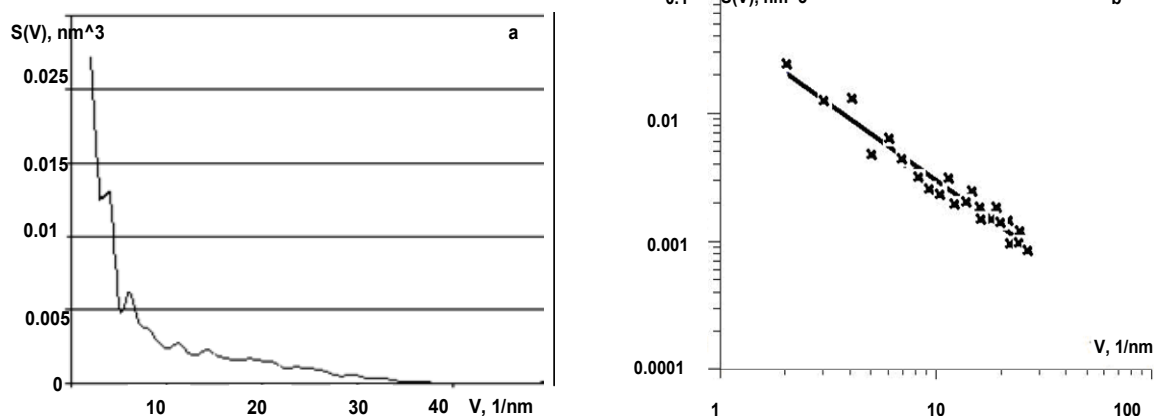


Fig. 4. The spectrum of the fiber's roughness as a function of spatial frequency. a – linear coordinates; b – linearization by the dual logarithmic scale

1. Goriachko A., Atomic force microscopy, to be published. 2. Jackle J. and Kawasaki K. Intrinsic roughness of glass surfaces // J. Phys.: Condens. Matter. – 1995. – Vol. 7. 3. Kovalenko A.V., Kurashov V.N. Kasil A.V. Radiation losses in optical nanofibers with random rough surface // Optics Express. – 2008. – Vol. 16, Issue 8. 4. Markuse D., Optical waveguides: textbook. – M., 1974. 5. Roberts P., Couny F., Sabert H., et.al. Ultimate low loss of hollow-core photonic crystal fibres // Opt. Express. – 2005. –

Vol. 13. 6. Suematsu J., Kataoka C., Kisino K., The fundamentals of optoelectronics: textbook – M., 1988. 7. Tong L., Hu L., Zhang J., et.al. Photonic nanowires directly drawn from bulk glasses // Opt. Express. – 2006. – Vol. 14. 8. Tong L., Lou J., and Mazur E. Single-mode guiding properties of subwavelength-diameter silica and silicon wire waveguides // Opt. Express. – 2004. – Vol. 12.

Received by editorial board on 19.06.09

УДК 535

V. Grygoruk, Dr. Sci., V. Sidorenko, PhD,
B. Melnik, MSc

NEAR-FIELD RESONANCE SYNCHRONIZATION OF DIPOLES

Знайдені відмінності між традиційними рішеннями полів диполя Герца в області $r \gg l_0 \ll \lambda$ та двох осцилюючих зв'язаних зарядів при $r \approx l_0$. Показано складний часовий характер вектора Пойнтинга в цій області, що збільшує взаємодію диполів, що відрізняються. Розрахована ближньопольова резонансна взаємодія диполів, які складаються з двох зв'язаних зарядів, в сильноградієнтних полях. Зроблено висновок, що зовнішнє ближнє поле може бути каталізатором усіх процесів, що розглядаються.

Ключові слова: ближнє поле, диполь Герца, вектор Пойнтинга, резонансна взаємодія диполів.

Differences between traditional solution of dipole Hertz's fields in regions $r \gg l_0 \ll \lambda$ and two oscillated tied charges in $r \approx l_0$ are found. Complex time structure of Pointing vector in this region is shown, that may lead to increase of interaction possibility of different dipoles. Near-field resonance interaction of dipoles, that consists of two tied charges, in external strong gradient field is calculated. Conclusions, that external near-field can be like catalyst of all process, is provided.

Key words: near-field, dipole Hertz's, Pointing vector, resonance interaction of dipoles.

Introduction. The last time one of the most rapidly growing areas of physics are nanophysics. Ability to manage the process of building nanostructure is very urgent task in our time. In the paper [5] experimental carbon deposition has been studied with CCl_4 ionized gas to the surface of fiber (nano-needle). Molecules were in the near field nano-needle that in fact was the catalyst for the process described above.

Theoretical basis for a lot of dedicated work [1, 3, 4, 6, 8]. Our work is one of the possible options for a theoretical explanation of the construction nanostructures in the near field through the near-field resonant interaction of dipoles.

Radiation of two tied charges in $r \approx l_0$. As you know, classical electrodynamics [7] defines dipole as a carrier of basic current, i.e., throughout the dipole length there is a known alternating current, the alternating dipole time. In our problem of this concept is not correct because such geometric scale and gradient external fields and their interaction are significant individual discrete charges that are part of the dipole.

In addition, calculations show that at distances of order dipoles size new near-field effects that can not be obtained within the model dipole Hertz. We know that all radiated

objects can be reduced to the sum of fields of dipole Hertz, which consists quasistatic fields of charges, reactive near-field and field of radiation – photons. Field radiation characters same direction of propagation of energy at any point and the first harmonics instant value vector Pointing.

Near-field characters by second harmonics instant value vector Pointing.

From the picture you can see, when the electromagnetic that when the time shift between E and H is $\pi/2$, instant value of vector Pointing is losing its single direction and 4 times for the period alters the direction of propagation of energy, i.e. the average energy transfer for the period is zero. This field is called evanescence. Thus near field can not be detached from the radiator and become distant. Limit between distant and near field advantage determined by the amplitude of the first or second harmonics.

But dipole Hertz not defined near the boundary, which is restricted to $r \gg l_0 \ll \lambda$. In addition, the condition $r \gg l_0$ – a condition that is similar to near field zone of Fraunhofer for near field, and $l_0 \ll \lambda$ – what in the near-field of dipole Hertz no analogue Fresnel zone for the near-field, the source is considered as spot and not fragmented for different wave zone.

To remove this restriction we had to move to the charge model dipole and this is not dipole Hertz as punctate and homogeneous element of current, a different physical problem. This zone is separated fields of individual charges that are dipole, a division of electrostatic interaction of charges of different signs, the electrostatic force acting on a neighboring charges and dipoles.

Therefore, the zone where we called local zone of dipole is ultra near-field zone. The boundaries between the classic near-field zone of Hertz dipole and local zone of dipole – is the border, starting from where a higher harmonics of Poining vector start to dominate over the second harmonic. Local zone of dipole – the notion of a purely geometric. Limit of local zone of dipole is associated with the size of oscillated object. This border separates charge field and the object begins treated as a single object – dipole Hertz. For an atoms and for large molecules this bound is different. Essentially, this is an area where the static fields of the charges are separated. Our problem is not the single point object – it has its own charge structure and the resulting field is a superposition of fields of each of the charges, creating an analog of Fresnel zone in the near field of local zone of dipole.

To solve the problem of finding the position of carriers in each time moment applicable method of movement recorded for each charge separately

$$m_i \cdot \ddot{r}_i = F_{ext_i} + F_{chg_i} + F_{dip_i} \quad (1)$$

where the index determines the number of discrete charge. In our model there are four – two interacting with each other in an external field of dipoles. The case is the sum of all forces acting on the charge. First – Strength of the external electromagnetic fields, second – the force of the electromagnetic fields arising during rapid movement of charges, and the third, which holds a pair of charges in bound state as a single system – dipoles respectively.

In common case the electromagnetic forces can be written like that:

$$\mathbf{F} = e\mathbf{E} + \frac{e}{c}[\dot{\mathbf{r}} \times \mathbf{H}] \quad (2)$$

Electromagnetic field of external field is known [1]. For the case of induced charge fields we use the relation of Lienar-Vihert and communication of vector and a scalar potential of electromagnetic fields with known Lorentz calibration.

$$\begin{aligned} \phi &= e/r \\ \mathbf{A} &= \frac{e}{c} \cdot \frac{\dot{\mathbf{r}}}{r} \end{aligned} \quad (3)$$

$$\mathbf{F} = -e^2 \left(\text{grad} \frac{1}{r} + \frac{1}{c^2} \frac{\partial \dot{\mathbf{r}}}{\partial t} \right) + \frac{e}{c} \left[\dot{\mathbf{r}} \times \text{rot} \left(\frac{e\dot{\mathbf{r}}}{cr} \right) \right] \quad (4)$$

Radiation calculation of two tied oscillated charges.

As was previously noted for the solution of the problem we are not correct use the classic definition dipole Hertz basic media as current as the current exists in each point dipole, unlike two discrete charges that fluctuate on the same periodic law. In the near zone interactions, i.e., over distances of order lengths dipole, and also in gradient fields this difference can be substantial and sometimes principal.

Also, as you know, near-field component vector Poining of dipole Hertz is a dual frequency, i.e. changing the energy distribution of radiation is four times the period. If you go by considering the average values, we lose this near-filed component, but it created real fields, which actually creates the appropriate strength and can really interact with the charges. It is known to us the process of transforming reactive field in active interaction with objects. Therefore, one of the important areas of research was to determine electromagnetic fields oscillated two related charges at distances of order the largest distance between

the charges and compare the results with well-known for the classical dipole Hertz.

Lastly, what we need to decide – this is the law of relative motion, i.e., fluctuations, our charges.

$$\begin{aligned} x_1(t) &= l_0 - x_0 \cdot \cos(\omega t) \\ x_2(t) &= l_0 + x_0 \cdot \cos(\omega t) \end{aligned} \quad (5)$$

Time latency to detector is

$$\begin{aligned} \Delta t_1(x, y, z, t) &= \frac{\sqrt{(x - x_0 \cdot \cos(\omega t))^2 + y^2 + z^2}}{c} \\ \Delta t_2(x, y, z, t) &= \frac{\sqrt{(x + x_0 \cdot \cos(\omega t))^2 + y^2 + z^2}}{c} \end{aligned} \quad (6)$$

So, resulting field is

$$\mathbf{E}_1(x, y, z, t - \Delta t_1) + \mathbf{E}_2(x, y, z, t - \Delta t_2) = f(\omega) .$$

From there you can see that we will have complex time structure of vector Poining because of non-linear dependence from frequency. The signal will be non-harmonious. Index = 1,2 means the first and second in charge of dipole respectively.

Bring major results. Below is shown the dependence of the components of vector Poining from time (fig. 1). Please note that despite the given law of motion of charges as a cosine, we do not get the appropriate one radiation. Space surveillance – 2 * l₀, where l₀ – dipole length.

At large distances the situation becomes classical, i.e. radiation given harmonic function. This can be explained by rapid extinction of high-frequency components.

The importance of taking into account this fact can demonstrate by taking the Fourier image of these signals. Below is given the dependence of the amplitude of the distance along the S_x axis for the first three harmonics (fig. 2).

However, notes that the second harmonic in the overwhelming majority of distances are the main.

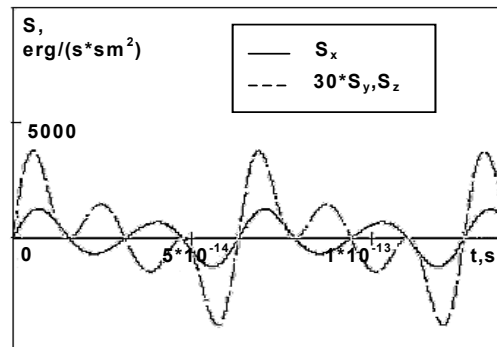


Fig. 1. Components of vector Poining in dependence from time

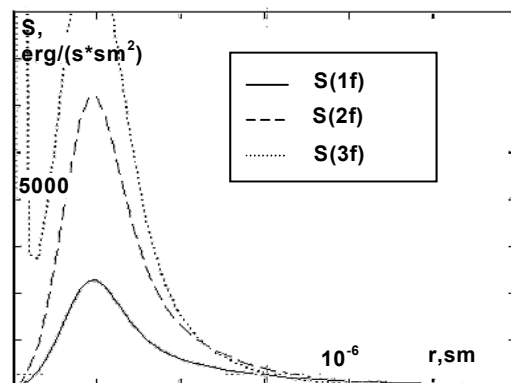


Fig. 2. Fourier components of vector Poining in dependence form Distance

Calculation of resonance dipoles interactions. To simulate [5], and so, to calculate near-field resonances in

dipole-dipole system, we have to solve (1). We have now all necessary information to do it, except the force that makes to charges in dipole to be in tied state. This is like some elastic force. In modern science, the force, that holds electron on atom orbit, currently doesn't known. But for simulation, in our problem, we don't need to know it. It will be enough just to approximate. So, what do we know about that force?

First, this force keeps charges in tied state and counteracts the destroying of tied state. Second, the amount of this force is much bigger the any external fields, also to keep in tied state. The third – it may have dependence from frequency of dipoles own oscillation modes. And we can put it linear because of its great magnitude. So, we can write it like following:

$$F_{dip_i} = -A(\omega) \cdot (r_1 - r_2 - l_0) \quad (7)$$

To simulate interaction with different dipoles put $A(\omega)$ like following:

$$A_1(\omega) = e \frac{-(\omega - \omega_0)^2}{\Omega^2} \quad (8)$$

$$A_2(\omega) = e \frac{-(\omega - \omega_0 - \Delta\omega)^2}{k \cdot \Omega^2}$$

But now this force depends from frequency and system (1) have the time like a variable. So, to complete the task we need to do Fourier transformation with this force. Finally, we can write:

$$F_{dip_i}(t) = -(r_1 - r_2 - l_0) \cdot \frac{2}{T} \cdot \sum_n \int A(\omega) \cdot \cos(n\omega t) d\omega \quad (9)$$

External fields of nano-needle is solved in [8], so we just use this results in numerical simulations

Results. All calculations was done for dipoles with such kind of parameters: $x_0 = 5 \cdot 10^{-10} m$, $2\pi\nu = 10^{13} s^{-1}$.

First, put two dipoles (fig. 3) in external near-field of nano-needle[5]

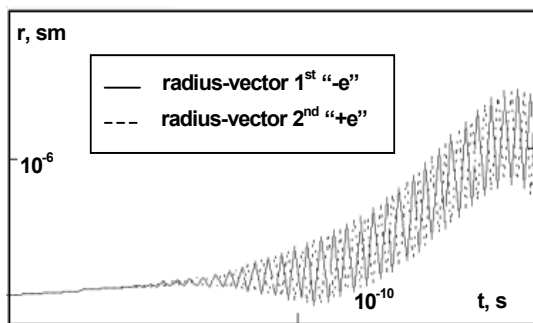


Fig. 3. Near-field resonance interaction of dipoles in external

Near-field

Then, put one of dipole out of gradient external near-field (fig. 4). The result of simulation is:

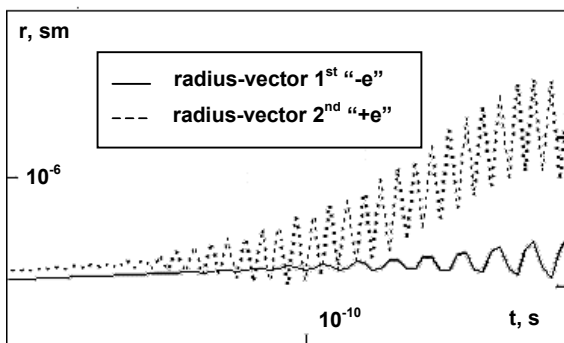


Fig. 4. Independent oscillation, when dipoles are out of gradient external near-field

Here we see that dipole's oscillations are independent and we haven't any interaction between them. Very similar results we'll have when we put two dipoles in weak external near-field (fig. 5).

So, words of explanation about resonance interaction in strong external near-field.

With all the rate will be proportional to magnitude characteristics the same field. And with the use of systems, where a second derivative in time – all this makes these frequency-organized rate (the system of equations for large amplitude will resemble the normal equation of harmonic oscillation) and so is that with increasing amplitudes of the two structures even with a slightly different phase portraits necessarily come in synchronism with each other at frequencies that may not coincide with their own. And once we move to compulsion in relation to a phase one – then the electrostatic force will orient their provision meets the minimum total energy system.

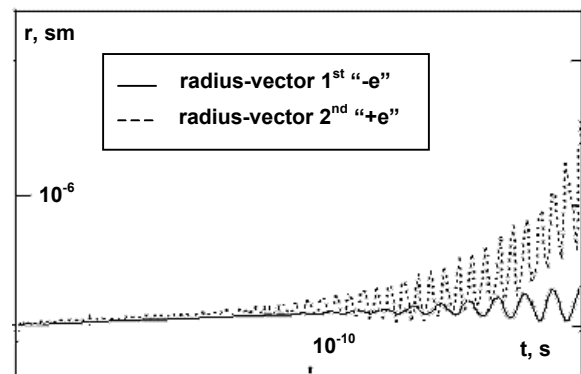


Fig. 5. Two dipoles in weak external field. No interaction

With increasing amplitude of the power of the near field becomes the largest, so it gives the movement two dipole structures. Explain it is: in the linear approximation of force actions by the external field can be pulled in a Taylor series

$$F_{ext}(r_1, r_2) \approx A_0(r_{10}, r_{20}) + A_1(r_{10}, r_{20}) \cdot |r_1 - r_{10}| + A_2(r_{10}, r_{20}) \cdot |r_2 - r_{20}| \quad (10)$$

With all the rate will be proportional to magnitude characteristics the same field. And with the use of systems, where a second derivative in time – all this makes these frequency-organized rate (the system of equations for large amplitude will resemble the normal equation of harmonic oscillation) and so is that with increasing amplitudes of the two structures even with a slightly different phase portraits necessarily come in synchronism with each other at frequencies that may not coincide with their own. And once we move to compulsion in relation to a phase one – then the electrostatic force will orient their provision meets the minimum total energy system.

Conclusions. 1. In small distances from dipole electromagnetic field that created it when fluctuation differs from those described by expressions for the classical dipole Hertz. Features of direction diagram and range are directly related to the formation of ordered structures of these dipoles.

2. Spectral composition of radiation in the same small distances is not monochrome, which makes it possible to effectively influence the dipole structure of even fields, which are non-resonant for this structure.

3. When large amplitude fields due to circumstances not synchronize 2 dipoles fluctuations with different resonant frequencies

4. At small field amplitude excites oscillations that are close to their own, so synchronization oscillations can not occur

5. Building a complex structure with two simple passes in two stages: at first they are synchronized with the second friend, that is, if a stop against another. The second phase of the work included strong electrostatic forces, and deploys compose molecules according to the provisions of minimum total energy.

6. External near field serves as a catalyst for these processes.

7. Given the (10) controls the frequency of vibration may not only with the amplitude of the field, but using that field with strong gradient and decomposition rate depends on the distance a pilot to choose the distance at which interaction takes place most effectively.

1. Арсланов Н.М., Моисеев С.А. Распространение ТМ и ТЕ электромагнитного поля в сужающемся зонде ближнеполевой оптической микроскопии с радиусом отверстия 50 нанометров

UDC 621.3.032.213.13

//http://zhurnal.ape.relarn.ru/articles/2005/237.pdf. 2. Гадо́мский О.Н., Глухов А.Г. Нелинейные резонансы в ближнеполюном взаимодействии атомов. // ЖЕТФ. – 2007. – Т. 130. – Вып. 1(7). 3. Гадо́мский О.Н., Кадо́чкин А.С. Метаструктурные системы из активированных нанослоёв и оптические ближнеполюные резонансы. // Оптика и спектроскопия. – 2005. – Т. 98. – № 2. 4. Гадо́мский О.Н., Харитонов Ю.Я. Квантовый компьютер на основе активированных диэлектрических наночастиц, селективно взаимодействующих с короткими оптическими импульсами // Квантовая электроника. – 2004. – Т. 34. 5. Григору́к В.И., Огенько В.М., Волкови́нская Л.С. та ін. Синтез вуглецевих наноструктур з використанням властивостей ближнього оптичного поля // Вісник КНУ, серія фіз.-мат. наук. Вип. 3. – К., 2006. 4. Евлюхин А.Б. Взаимодействие полупроводников и систем, содержащих наночастицы, с ближним полем. // Владимирский ГУ., канд. дисс. – М. 2007. 7. Саль С. Расчет поля излучения диполя путем непосредственного интегрирования уравнений Максвелла // ГУП НВЦ ГОИ им. Вавилова. – Санкт-Петербург. – 2004. 8. Харитонов Ю.Я. Оптические процессы в структурированных системах из взаимодействующих наночастиц и оптические ближнеполюные резонансы. // канд. дисс. – Ульяновск, 2006.

Submitted on 20.10.09

A. Dudko, stud., O. Lushkin, Ph.D.

THE TEMPERATURE INFLUENCE ON THE EMISSION PROPERTIES OF THE SC-BA DISPENSED EMITTERS WITH THE W MATRIX

Наведено результати експериментальних досліджень, щодо впливу температури на склад поверхні та емісійну здатність скандат-барієвих металевопористих емітерів (МПЕ) з вольфрамисловою матрицею. Були отримані і проаналізовані оже-електронні спектри, які характеризують склад поверхні МПЕ, та його вольт-амперні характеристики (ВАХ) при різних температурах. Показано, що існує чітка кореляція між рівнем емісії досліджуваних зразків та кількістю скандієвої компоненти на їх робочій поверхні. Встановлено також, що у активних скандат-барієвих МПЕ вплив температури на емісію при високих анодних напругах помітно знижується.

Ключові слова: металевопористі емітери, вплив температури, оже – спектроскопія, поверхня.

The results of experimental studies of the effects of temperature on the surface composition and the emission properties of the Sc-Ba dispensed emitters (MDE) with the W matrix are shown. Were obtained and analyzed Auger spectra that characterize the surface composition of MDE and its volt-ampere characteristics (VAC) at different temperatures. It is shown that there is a clear correlation between level of emission of investigated samples and the number of scandium component on their surfaces. It is also established that the influence of temperature on the active scandium-baric MDE emission at high anode voltage had decreased.

Key words: metallic dispensed emitters, influence of a temperature, auger spectroscopy, surface.

Introduction. The researches of thermoemitters are relevant because nowadays they are the main element in the microwave devices used in space communications. The best parameters of these devices are achieved when using exactly Sc MDE. However, up to the present day there is no clear theory for explanation of the mechanism of the emission for such emitters. Despite the fact that a lot of experimental results have already been received [1] there is a series of questions which need to be answered. One of them is the possible dependence of the emission possibility of the emitters from its structure (needle-shaped formation of the active substance or thick layers of this substance on tungsten grains) and the composition of the emitting surfaces. So study of the effects of temperature on these characteristics and their relationship with the emissive power of scandium-baric MDE is relevant.

Experimental. The researches were carried out in ultra high vacuum chamber at pressure that did not exceed $1.33 \cdot 10^{-7}$ Pa. There was an Auger analyzer type cylindrical mirror to analyze the composition of the surface and the molybdenum anode for the pulsed emission measurements. The design of the anode provides possibility of heating it up with the electronic bombardment to the high temperature, allowing to prevent poisoning of cathodes in the measurements due to the so-called anode effect. For conditions of the research are do not affected the final result, samples are installed under anode only for the minimum necessary for the measurement time. Distance anode – cathode before VAC measurements is carefully controlled and installed with an accuracy of $1 \text{ mm} \pm 10 \text{ microns}$. All VAC were obtained using single pulse mode with pulse duration of 7 microseconds. Pulse amplitude was able to change from 0 to 5000 V.

As experimental samples were used MDE with W matrix with emissive active substance which consisted of $3,6\text{BaO} \times 0,4\text{CaO} \times 0,5\text{Sc}_2\text{O}_3 \times 0,5\text{Al}_2\text{O}_3$. That is, scandium

oxide was introduced in the volume of sample. These MDE with a high concentration of BaO compared to concentrations of CaO in active substance were used in electric appliances, where the cathode was operated at elevated pressure of residual gases.

Results and discussion. When small heating up was used, namely when heating up current was 0.55 A and the time up to 10 minutes, recorded Auger spectrum still had Auger peak at energy 273 eV that belongs to carbon. So heating was extended at a higher temperature. Figure 1 shows Auger spectra of MPE at different heating up current. Spectra show that increasing of cathode temperature led to a rise of the sulphur on its surface and to a significant reduction of carbon.

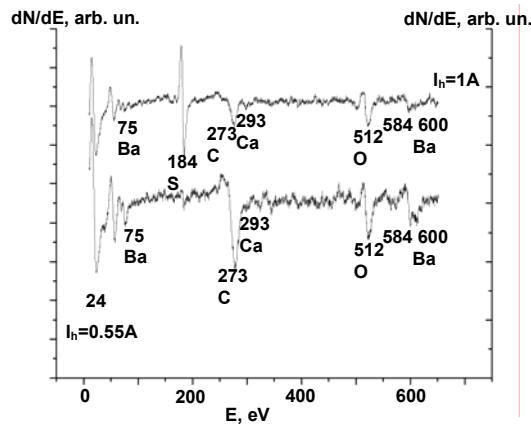


Fig. 1. Auger spectra of MDE obtained with heat up current 1 A (top) and heat up current 0.55 A (bottom)

Sulphur is a harmful impurity in MDE because it adsorbs on the grain of tungsten matrix and blocks the migration process of Ba-components to the working surface of cathodes. That is significantly reducing their emission ability. Indeed, investigations of the sample in this research period showed almost no emissions, though there is significant number of Ba-components on the surface. However, there are also Ca component on the surface. This, according to [3], indicates the absence of the Ba-components crystallites on the grain of tungsten matrix. The basis for these crystallites is the formation of molecules CaO.

With further heating up of the sample to a temperature of 1300 K, as seen from the Auger spectrum of Fig.2, the surface is changed: such components as W, Sc and Sc2O3 became visible, and pollution in the form of carbon and sulphur disappeared.

Presence of the large amplitude of Auger peaks of tungsten and the absence of calcium components Auger peaks indicates the formation in this period of three-dimensional islands (crystallites) on the surface of the sample with typical sizes of several hundred nanometers, which are major emissive centers in MDE [3].

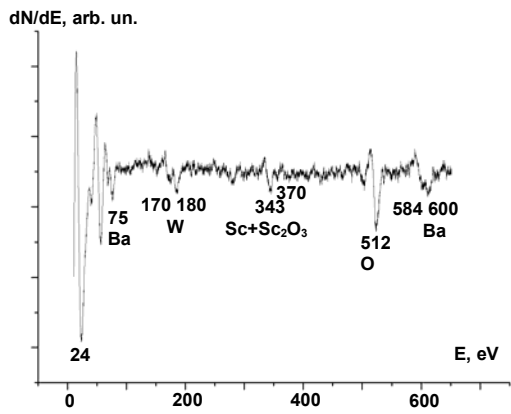


Fig. 2. Auger spectrum of MDE obtained at a temperature of 1300 K

Indeed, checking the availability of emission showed that cathode became active: see. Fig.3.

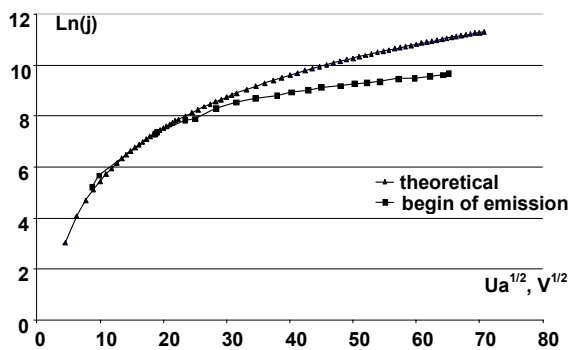


Fig. 3. Theoretical and experimental VAC of the MDE in Shotki coordinates obtained at a temperature of 1300 K

In Figure 3 draws the attention some differences between theoretical Chayld-Langmuir law and experimental VAC: with anodic voltage under 200 V experimental curve deviates from the law of 3 / 2. This deviation is even more noticeable after MDE heating up to T = 1400 K, that is clearly visible in Figure 4. Analysis of this picture shows

that the deviation from the law of 3 / 2 exists in the whole temperature range from 1200 K to 1400 K.

The comparison of the Auger spectra from Fig. 2 and Fig. 5 can answer the questions about the reason of such behavior of VAC. It is clearly visible – the work of MDE at T= 400 K led to the increasing of the Sc-component on the surface of the cathode regarding tungsten , and therefore more clearly expressed specific of Sc-Ba emitters, which manifests itself in significantly increasing of the influence of an electric field on the emission.

During the experiment it was also observed that in the measurements of VAC at the temperature T=1400 K it is impossible to increase the voltage above 3000 V due to electrical flashover in the anode-cathode gap. Likely, it is associated with increased flow of the Ba component, which evaporates when MDE and further ionizes by its own electrons.

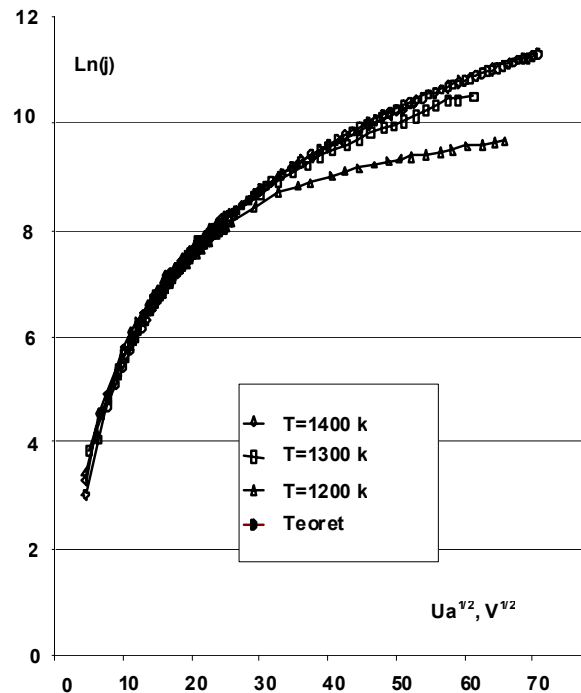


Fig. 4. VAC of the MDE in Shotki coordinates obtained at different temperature after heat up at 1400 K

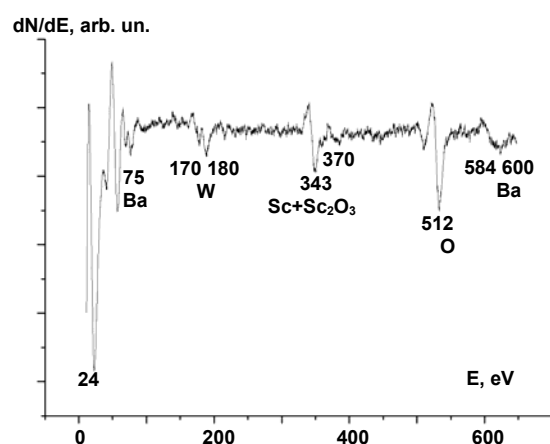


Fig. 5. Auger spectra of MDE obtained after heat up at 1400 K

The matter is that the sample is composed of active substance where the amounts of barium oxide in 9 times

more than the amounts of calcium oxide, and it reduce the heat of evaporation of the Ba component.

Due to the fact that the emission ability of the sample after several hours at $T=1400$ K practically did not changed, a higher temperature activation was made: cathode worked one hour at $T=1500$ K. Such process caused only the redistribution of the amounts of components relative to tungsten on the work surface.

Analysis of Auger spectra recorded during this period showed a substantial reduction relations of amplitudes of Auger peaks of Sc-component, oxygen, Ba and BaO to W. This fact and fact of noticeable increasing of the emission activity of the cathode in the entire temperature range (see Figure 6) clearly indicates the formation of additional crystallites of barium-calcium with adding of scandium oxides on the MDE surface. The comparison of the results from previous work [2], which studied scandium-barium emitters based on W-matrix, and results obtained from this work, allows to argue that there are much more crystallites on the working surface of the sample after such thermo-vacuum processing. It is also possible that crystallites could change their form: they have become more needle-shaped. This is a marked VAC deviation from the law of $3/2$ in the range of the space charge limitation of the anodic current for all temperatures of the experiment. The role of temperature in this period is reduced only to the formation of micro-nanogeometry of emission-active centers on the tungsten grains, which usually produce an anodic current.

Figure 6 also implies that heating up to temperature $T = 1300$ K is sufficient to create such structures. Indeed, the anodic current increases with voltage increasing and practically the same at $T = 1300$ K and $T = 1400$ K at the anode voltage from 0 to 1500 V. When a voltage is above 1500 V this VAC became different. This may be referred to a significant influence of an electric field on the process of evaporation of active cathode material, and hence on the composition and possibly form of emission centers.

In analysis of all the aggregate data obtained in the work one should also pay attention to:

1) the disproportional growth of the anodic current density of MDE with increasing temperature in the region of it's possible saturation;

2) small deviations of experimental VAC from the law of "3/2" in the region of limitation of anodic current by space charge at the beginning of activation when the amount of Sc-components on the surface is very small, and to significant deviation from this law in the end of activation when the amount of Sc-components is large. The experimental characteristics crossing the theoretical curve with the larger anodic voltage, the higher temperature is.

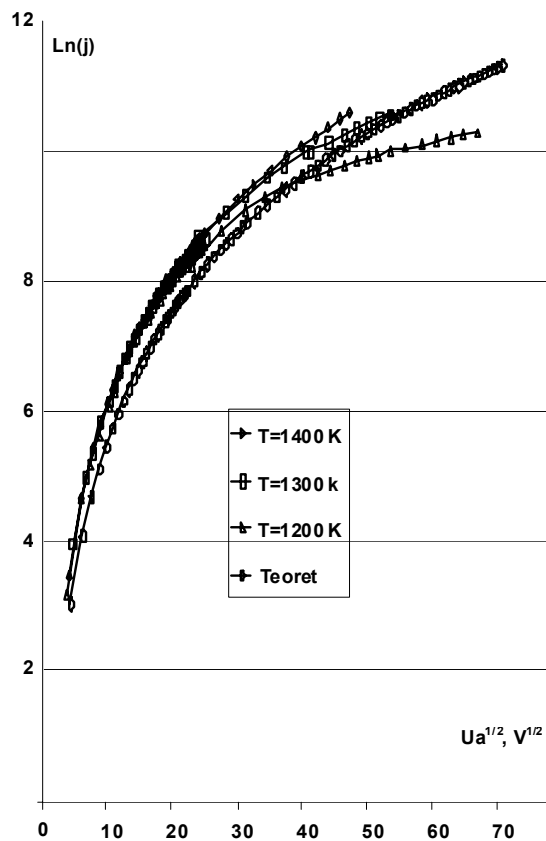


Fig. 6. VAC of the MDE in Shotki coordinates obtained at different temperature after heat up at 1500 K

Described features of the behaviour of experimental VAC give us grounds for assuming that the studied sample is working in the mode in which space charge near the sample surface is so small that it does not limits the anodic current.

Conclusions. Analyzing all the above set forth mentioned, you can make the following conclusions.

There is a microstructure of an emission-active substance, including scandium component, formed on the surface of Sc-Ba MDE with tungsten matrix after activation of the working surface. This structure changes the character of the emission of porous metal cathodes from thermoelectronic to a more complicated: thermo- and autoelectronic emission.

Sc2O3 likely contributes to the formation on the surface MDE of more advanced emission-active microstructure, which provides high emission efficiency. The availability of Sc components in these bulk micro-formations does not allow MDE to work with a space charge limitation of anodic current even at anode voltage of several tens of volts.

The role of temperature in the Sc-Ba MDE – lies in supplying of active substances from the volume of the matrix to the surface for the formation of micro-geometry of emission-active centres with complicated emission character.

1. Yamamoto S., Taguchi S., Watanabe I. et all. Electron emission enhancement of a (W-Sc2O3) coated pregated cathode by oxidation of the coated thin film. //J. Journal Applied Physics. – 1988. – V.27. – N.8.
 2. Бех І.І. Фізико-хімічні та емісійні властивості гетерогенних систем на основі скандію. Канд. дисертація. – К. 2007. 3. Лушкін О.Є. Роль кристалітів оксидів лужноземельних металів в механізмі емісії металевопористих катодів. Канд. дисертація. – К. 1996.

UDC 537.311.322

A. Duhliy, eng., V. Il'chenko, Dr.Sc.,
V. Telega, PhD, A. Kravchenko, PhD,
D. Zatishnyi, stud.

INVESTIGATION OF THE ELEMENTAL STRUCTURE OF SnO_2 FILMS DOPPED WITH PT HETEROSTRUCTURE SnO_2/SI

В роботі представлені результати дослідження розподілу елементів по товщині плівок гетероструктур SnO_2/Si легованих Pt та не легованих із застосуванням методики електронної оже-спектроскопії та методики іонного пошарового розпорощення. Товщина плівок, напорошених на кремнієву підкладку, складала 30 нм.

Ключові слова: плівка, гетероструктура, Оже-спектроскопія, іонна очистка.

In this work we present results of study of elements' distribution in films SnO_2/Si heterostructure undoped and doped with Pt thickness. The electronic Auger spectroscopy and method of ion layer sputtering were used. The thickness of films, sputtered on the silicon pad, was 30nm.

Keywords: film, heterostructures, Auger spectroscopy, ion sputtering.

Introduction The present development and application of nanotechnology stimulate the intensive study of characteristics of such materials, that can be used as sensitive elements in sensors and sensor systems creation. The main reason is that such systems open new possibilities of such materials applications in various fields of human activity. In medicine they can be used for disease early stages testing and remote analysis of the obtained results, or as converters in biosensors. In environmental protection these system can be used for small concentrations of injurious and toxic substances formed during the incineration of different materials indication [1, 2, 3].

The study of possibilities of silicon-based heterostructures as primary transmitters of signals, depending on gas environment, recently excites many researchers' interest. Such structures are sensitive high enough and don't need high operating temperatures. Besides, they are the cheapest among all semiconductor structures. Searching of the materials with electrophysical parameters depending on gas environment is the important problem for creation of gas-sensible devices, including devices based on contact structures nanofilm of metal oxide – silicon. In this case the volume of parameter changes is very important. It is known that thin films can be used as sensitive element in the sensor system. The sensitivity of such heterostructures depends on the type of active adsorption layer and its elemental composition. The doping of these structures with metals can result to elemental composition changing, which affects the electrophysical characteristics that basically are determined by the behavior of the heteroborder during the gas absorption [1, 2, 4].

The aim of this work was to study elemental composition of SnO_2 films, unalloyed and alloyed with Pt (1%), during the layer etching, and the influence of Pt alloying on behavior of elements in samples.

The experimental samples. During the study two heterostructure samples based on SnO_2 films were used, the first one was doped with Pt (1%), and the second one was undoped. The thickness of the samples was 30 nm. The samples were applied on the silicon pad by pyrolytic sedimentation method. Their structure is presented on the Fig. 1

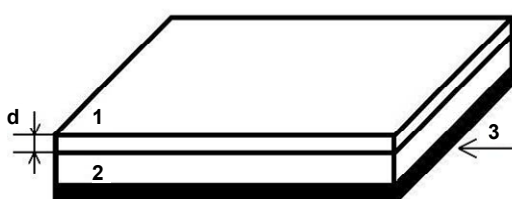


Fig. 1. Structure of the experimental sample:
1 – SnO_2 film, 2 – Si, 3 – Al (ohmic contact)

Experimental equipment and results The experiment was carried out in a working chamber of high-vacuum system made of stainless steel 1X18H9T. The elements distribution in heterostructure film's thickness was obtained using the electronic Auger spectroscopy and method of ion layer sputtering. The measuring was carried out using the serial device 09ИОС-3. The "cylindrical mirror" was used as the energy analyzer. After thermal degassing the pressure in the working chamber was $P=1 \cdot 10^{-9}$ torr.

The ion gun, made as a built-in module on the flange ДУ-50, was used for the ion sputtering. The argon gas was used as the ion source, because it is chemically passive and has small factor of surface adhesion.

Composition of residual gases was controlled by the monopolistic mass-spectrometer of MX-7304 type.

Mutual allocation of the manipulators with the investigated samples relatively to the Auger spectrometer's sensor, ion gun and mass-spectrometer is presented on Fig. 2. Samples were settled on the high-vacuum manipulator M1 so as they could be carried in turn to the ion gun for the layer sputtering of the heterostructure film and to the Auger spectrometer's sensor for the elemental composition of the surface investigation.

On the side manipulator M2 the probe for heterostructure's volt-ampere characteristic measurement was placed.

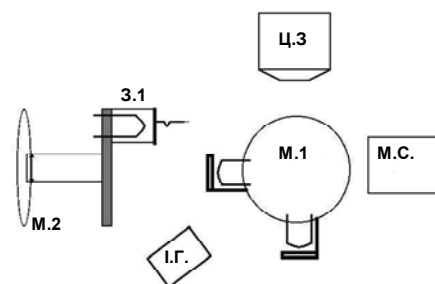


Fig. 2 Experimental equipment scheme

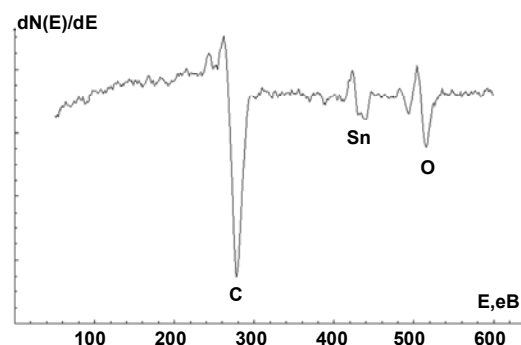


Fig. 3. Auger spectrum of the sample before the process of spraying, film SnO_2

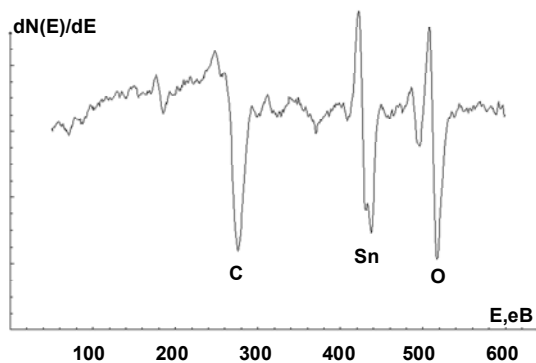


Fig. 4. Auger spectrum of the sample before the process of spraying, film $\text{SnO}_2 + 1\% \text{ Pt}$

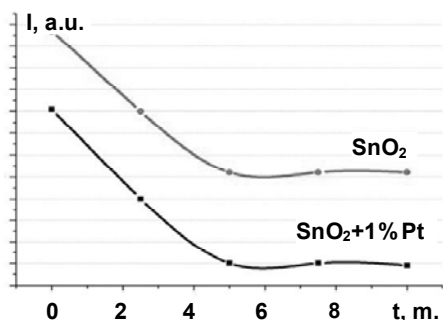


Fig. 5. The dependence of relative intensity changing of C Auger peaks on the time of etching

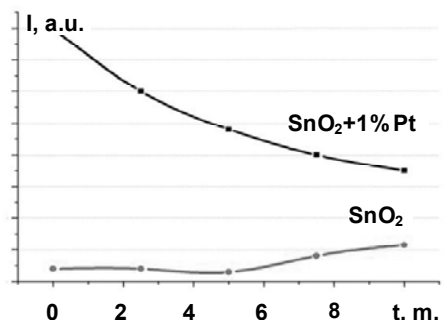


Fig. 7. The dependence of relative intensity changing of O Auger peaks on the time of etching

The Auger spectra, obtained for the initial surface structures are presented on Fig. 3 and Fig. 4. There's an essential peak of the absorbed C along with the primary elements (Sn and O) on Fig. 3-4. During film sputtering the peak of C decreases with the time of sputtering for both of the samples, it can be seen on Fig. 5. The study of the surface composition in thickness revealed that in the samples, doped with Pt, the presence of C in thickness is three times less in comparison with the undoped sample. This can be explained by the weaker stability of Pt-C compounds [6], and so carbon doesn't stay too long on the film's surface. As the experiments show, the elemental composition of doped and undoped samples is different. The absolute values show that the change of Sn quantity

on the film's surface proceeds in different ways for the both samples: in the undoped sample it monotonically increases in thickness of the near-surface layer, instead in the doped sample it increases in first, reaches it's maximum and then decreases (Fig. 6). It is also worth of noticing that the intensity of the Auger peaks in the doped sample is much larger in comparison with the Auger peaks of the undoped sample.

In the undoped sample the quantity of O in the beginning of etching is much larger then in the sample doped with Pt. The quantity of O decreases with thickness in the doped sample, while in the undoped sample it practically stays unchanged. After 5 minutes of etching the quantity of O is in 2 times less then in the doped sample (Fig. 7). Therefore, the quantity of O in this case results to the current passing character change because of change of the zone relief on nanocrystal border.

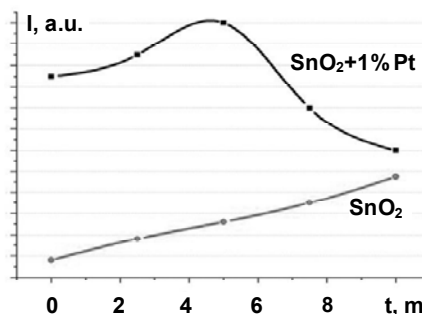


Fig. 6. The dependence of relative intensity changing of Sn Auger peaks on the time of etching.

It may be assumed that in the absence of doping the sedimentation of C is a uniform monolayer of atoms, that cover all the surface of the sample, and the Auger peaks of other elements (except of C) are small. During the doping with Pt the quantity of C accumulates in some regions of the film. Therefore on the Auger spectrum not only C-peak is visible, but the peaks of other elements, which are comparable with the value of C-peak.

Conclusions The basic elements of the films (C, Sn and O) dispersed heterogeneous in the sample's thickness. The energetic locations of basic elements' peaks in Auger spectra changed during study films in thickness. Such displacement can be the result of energetic bond change with the change of distance to hetero-transition. In turn, it can result to the change of film's sensitiveness on the environment.

1. Ilchenko V.V., Kravchenko A.I., Telega V.N., Chekhun V.P., Skryhyn I.V. On the possibility of the use of nonlinear properties heteroperehodov on the basis of nanorazmernaya films SnO_2 -silicon analysis for atmosphere. – Nanosistemy, nanomateryaly, nanotechnology. Collected Works T2., B.2. Publishing House "Akadempriodyka" K. 2004. 2. Vashpanov Y.A., Smytnyna V.A. Affinity sensitivity semiconductors: Monograph. – Odessa: Astroprint, 2005. – 216 pp. 3. Arnold C., Harms M., and Goschnik J., IEEE Sensors Journal, No.3: (2002). 4. Bomk O. I., Ilchenko L. G., Ilchenko V. V., and Kuznetsov G. V., Abstr.Int. Conf. 'Eurosensor 2000' (June 2000) (Copenhagen, Denmark: 2000), p. 189. 5. Korotchenkov G., Brinzari V., DiBattista M., Schwank J., Vasilien A. Peculiarities of SnO_2 thin films deposition by spray pyrolysis for gas sensors applications // Sensors and Actuators. — 2001. – B77. 6. Nekrasov B.V., Fundamentals of General Chemistry. Vol I Ed. 3rd, corr. and add. Publishing House "Chemistry", 1973, 656 p.

Submitted on 20.06.09

UDC 535.36

O. Isaienko, stud, A. Ivanisik, Ph. D.

MODIFICATION OF THE DYNAMIC LIGHT SCATTERING FOR NANOPARTICLES SIZE MEASUREMENT

Описано модифікацію методу динамічного розсіяння світла. Запропоновано вимірювати час когерентності розсіяного зразком світла для визначення розмірів наночастинок, що знижує апаратні вимоги до установки, оскільки дозволяє не використовувати в ній швидкісний корелятор.

Ключові слова: динамічне розсіяння світла, час когерентності, розмір частинок.

The modified method of Dynamic light scattering is discussed. Measuring the coherence time instead of correlation time of scattered light intensity makes it possible to avoid usage of correlator in the device that is used to measure particle sizes.

Key Words: Dynamic light scattering, coherence time, particle sizes.

Introduction. Nanoparticle materials are used in various fields. In particular, silver nanoparticles are used in medicine as an antiseptic, in optics – to achieve the effect of surface-enhanced Raman scattering.

During optical experiments, it is important to control the average size of nanoparticles, and there are many different methods for this [1]. However, each of them has both merits and drawbacks. For example, a very precise method of measuring the size using an atomic force microscope requires considerable investments, while only gives information about the size of a small finite number of particles on the surface only. Optical microscopy does not allow measuring the particle sizes smaller than the wavelength of visible light. Laser-diffraction techniques are limited to the minimum size of a few micrometers. However, there is a method for measuring the size of particles scattered in liquid from the nanometer up to several micrometers range, termed dynamic light scattering. This study is devoted to it.

Autocorrelation function of the intensity of scattered light. The essence of the method is based on determining the diffusion coefficient D of particles, and further calculation of the radius of spherical particles. Determination of D becomes possible due to Brownian motion of particles under study. Chaotic Brownian motion causes the microscopic fluctuations of the local concentration of particles, which results in fluctuations of intensity of light scattered on them. The diffusion coefficient depends on the time correlation function of light intensity fluctuations [2]. Temporary autocorrelation function is defined by expression:

$$G(\tau) = \langle I(0) \cdot I(t - \tau) \rangle = \lim_{t_m \rightarrow \infty} \frac{1}{t_m} \int_0^{t_m} I(t) I(t - \tau) dt, \quad (1)$$

where the intensity I has different values at time t and, t_m – time measurement of the correlation function. Relaxation of the concentration of microscopic fluctuations to the equilibrium state can be described by Fick law (diffusion equation):

$$\frac{\partial c(r, t)}{\partial t} = -D \nabla^2 c(r, t), \quad (2)$$

where $c(r, t)$ is the concentration and D – diffusion coefficient of particles. Autocorrelation function of the scattered light intensity decays exponentially over time, and the characteristic relaxation time is associated with diffusion coefficient D . Correlation function of intensity of scattered light is given by:

$$G(\tau) = a \exp\left(-\frac{2\tau}{t_c}\right) + b \quad (3)$$

In accordance with the solution of the diffusion equation, inverse correlation time is equal to:

$$\frac{1}{t_c} = Dq^2 \quad (4)$$

Fluctuations wave vector q is described by the expression:

$$q = \frac{4\pi n}{\lambda} \sin \frac{\theta}{2}, \quad (5)$$

where n is the refractive index of liquid, λ is the wavelength of laser light, θ is the scattering angle.

Constants t_c , a and b are determined by approximation of the measured correlation function with the theoretical exponential curve. Defining correlation time t_c in such a way, it becomes possible to determine the diffusion coefficient, and then, on a formula determined by the Stokes-Einstein, radius of spherical particles can be calculated:

$$R = \frac{4k_B T \pi n^2}{3\eta \lambda^2} t_c, \quad (6)$$

where k_B is the Boltzmann constant, T in this equation is the absolute temperature of the liquid, η is the viscosity coefficient.

However, in this case, the experiment requires a high-speed correlator – a reading system for measuring the fluctuations of scattered light intensity in a very small time interval. And the time between these intervals should be even smaller and be constant with great precision. Technical realization of such devices is rather difficult, so it is important to find methods to determine the correlation time in a more accessible way.

The coherence time of chaotic light. Chaotic radiation of scattered light has a certain time of coherence, and it has the order of several microseconds. This light is described by the coherence function, the general form of it is described by the equation:

$$g(r_1 t_1, r_2 t_2) = g_{12} = \frac{|\langle E^*(r_1 t_1) E(r_2 t_2) \rangle|}{(\langle |E(r_1 t_1)|^2 \rangle \langle |E(r_2 t_2)|^2 \rangle)^{1/2}}, \quad (7)$$

where $r_1 t_1$ and $r_2 t_2$ are two space-time points, and the angular brackets indicate averaging over the ensemble. In the case of the Lorentz frequency distribution (Lorentz line), and for $r_1 = r_2$ (one point of space), g_{12} takes the form:

$$g(\tau) = a \exp\left(-\frac{2\tau}{\tau_{coh}}\right) + b, \quad (8)$$

(τ_{coh} is the coherence time) which coincides with the autocorrelation function of scattered light, but instead of correla-

tion time, the coherence time is used in this case. Since the correlation time coincides with the time of coherence, it is possible to change the method of measurement, and do not use the correlator.

One of the ways of measuring the coherence time uses the photon-counting mode of light intensity registration [3]. In this case, the dependence of variance (σ^2) from the time of photocounts accumulation (T) is measured. Theoretical dependence is:

$$\sigma^2(T) = \bar{n} + \frac{\bar{n}^2 \tau_{coh}}{2T^2} \left\{ \exp\left(-2\frac{T}{\tau_{coh}}\right) - 1 + 2\frac{T}{\tau_{coh}} \right\}, \quad (9)$$

where \bar{n} is the average number of photocounts during measuring time T . In practice, the average number will grow with the increase in T , so it is convenient to use variance, normalized by the average number of counts:

$$\sigma_n^2 = \frac{\sigma^2}{\bar{n}} \quad (10)$$

Graph of this dependence is shown in Fig. 1 using following parameters: $\bar{n} = 2$ counts per $1\mu s$, $\tau_{coh} = 1\mu s$.

In this case the correlator is replaced by a counting system, which will summarize the photocounts from photoelec-

tron multiplier during a fixed time T . It is no longer necessary to control the time intervals between the summation, and in addition this time can be much bigger than T .

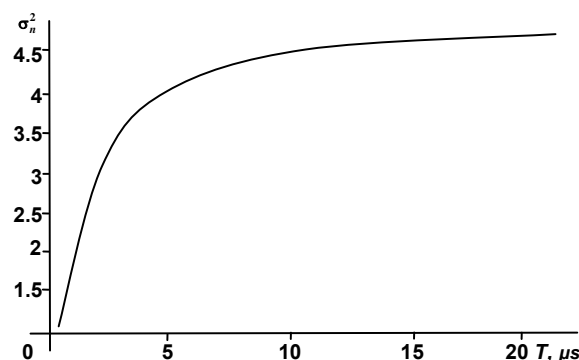


Fig. 1. The dependence of the normalized variance on the measurement time

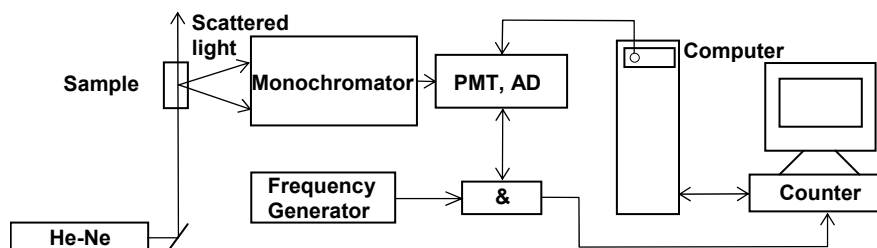


Fig. 2. The block diagram of the experimental setup

Implementation of the methodology. The block diagram of the experimental setup for measuring the size of nanoparticles is shown in Fig. 2.

Light from the He-Ne laser passes through a cuvette with a solution of the studied nanoparticles. The intensity of scattered light is measured by the system of photon counting, constructed of the spectrometer-monochromator, photoelectron multiplier tube (PMT) and analog discriminator (AD).

The generator of rectangular pulses is added to actualize the summation of pulses from the discriminator during time T only. It is combined with the AD and connected to the scheme of logical multiplication. As a result, photocounts are sent to the counter during periods of time T and they are summarized in the packages. Management of the system occurs in automatic mode using a computer.

It should be noted that the discriminator is used with a pulse shaping scheme, which inverts signals from PMT. In this case logical "0" is obtained when the photopulse is detected, and the logical "1" when there is no pulse.

Measurement cycle is as follows:

- the generator's pulse duration of T (the photocounts summation time) is set;
- the number of photocounts in each package is summarized and saved;
- after a large number of pulses from the generator (which means a large number of photocount packages), the time T changes and the cycle repeats.

As a result, the pulses arriving at the counter after the scheme of logical multiplication are as shown in Fig. 3, and

we obtain a set of measurement values of the photocounts for different times T .

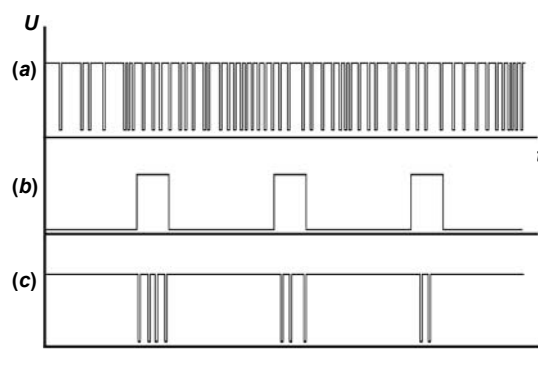


Fig. 3. Pulses from AD (a), frequency generator (b) and the resulting pulses at the counter input (c)

The mean value and normalized variance are calculated for each set, and by approximation the normalized $\sigma_n^2(T)$ by the theoretical curve shown in Fig. 1, the coherence time is obtained. Knowing that time, it becomes possible to calculate the radius of spherical particles.

However, it is important to carefully setup all devices before the actual experiment:

- He-Ne laser beam intensity should be controlled, as it can fluctuate over time and this may become an additional source of errors;

- the generator pulses of time T must be as stable, as possible, therefore a control device, such as an oscilloscope, can be added to the site;

- the PMT must satisfy several requirements, such as the low response time, ability to work with intense light.

Experimental results. Using this method, the size of the two types of particles was measured in testing purposes. The first one was the colloidal solution of silver nanoparticles produced by Nature Sunshine Products and used as active food additives (code 4074-4). Obtained dependence $\sigma_n^2(T)$ and the approximation with the theoretical curve are shown in fig. 4.

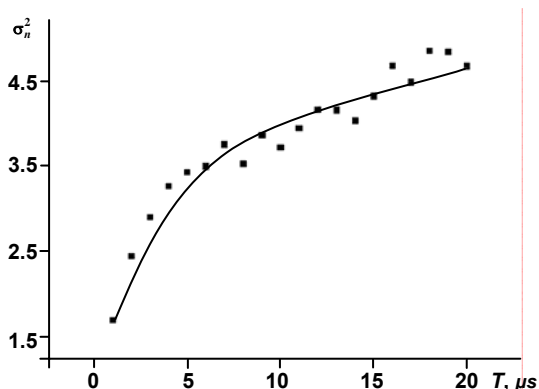


Fig. 4. Approximation of the normalized variance by the theoretical curve for colloidal solution of the silver nanoparticles in water

After approximation, the time of coherence was determined and equal to $(66,8 \pm 7,3)$ ms. Assuming that these particles are spherical, their radius can be calculated and it is 9 nm. Declared by a manufacturer, the range of nanoparticle sizes is 1 .. 50 nm. The approximation relative error of 11% in this case indicates a rather large variability in sizes, which is confirmed and specified by the range of values.

The second sample was a solution of fullerene molecules C60 in toluene. The result is depicted in Fig. 5.

After approximation, the coherence time was determined and equal to (2.09 ± 0.07) ms, which corresponds to

the radius of spherical particles of 0.40 nm. It is known that the radius of a spherical fullerene molecule is 0.375 nm. Given that the technique of dynamic light scattering determines not the geometric radius of a specific particle, but its hydrodynamic radius, which is associated with the diffusion coefficient, the result may be higher than actual size. Therefore, in this case, the excess of the known size of 7% can be considered valid. Also the fact that the relative error is 3% shows a high uniformity of particle size.

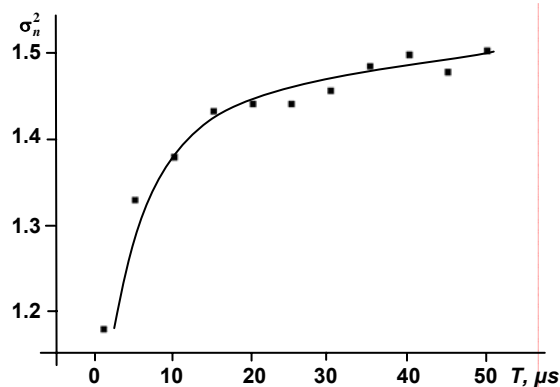


Fig. 5. Approximation of the normalized variance by the theoretical curve for solution of the fullerene C60 in toluene

Conclusions. The described method of measuring the size of nanoparticles in solutions using coherence time of scattered light, makes it possible to avoid usage of the complex correlator. This means that hardware costs of the device used for measuring the size of particles are reduced. The experimental results showed in this article prove the possibility of applying this method of measurement in practice.

1. Berne B.J., Pecora R. Dynamic Light Scattering with Applications to Chemistry, Biology and Physics. Wiley-Interscience. – N.Y., 1976. 2. Measuring Nanoparticle Size Distributions in Real-Time: Key Factors for Accuracy: Nanotech conference, Santa Clara, 20-24 may 2007. 3. Лоудон Р. Квантовая теория света. – М., 1976.

Article submitted on Oct 22, 2009

UDC 5681.325.5:533.9.082.5

M. Kleshich, stud., V. Boretskij, post grad. stud.,
A. Veklich, Ph. D.

CONTROL SYSTEM OF MONOCHROMATORS MDR 12/23

В даній роботі розроблено пристрій дистанційного керування монохроматорами МДР-12/23 на основі двох мікроконтролерів АТіпну 2313. Створена схема керування кроковим двигуном ШДР-711, що забезпечує струм в обмотках до 2,5А. Розроблені програмні алгоритми на мові асемблера дозволяють: – змінювати швидкість крокового двигуна дискретно на 9 позицій; – виводити на світлодіодний індикатор значення довжини хвилі спектральної лінії та швидкість сканування спектру.

In this paper the results of development of remote control system of monochromator MDR 12/23 at the base of two universal Atmel microcontrollers ATtiny2313 are shown. The control scheme of the ШДР-711 step motor is realized. The current in each winding is up to 2,5 A. The special original software algorithms of controllers are designed to provide: – the discrete change (9 positions) of motor scanning rate in the both directions; – the dynamical indication of wavelength and rate of spectrum scanning.

Keywords: remote control, step motor, microcontroller, dynamical indication.

Introduction

In the optical emission as well as absorption spectroscopy such spectral system as LOMO KSVU still are widely used. Depending on the current problem or version of such system the monochromator MDR-12 or MDR-23 as a spectral device can be utilized. The step motor ШДР-711 is used in both models of monochromators to provide the spectrum scanning by the rotation of the diffraction grating. The manufacturer developed initially in this system an addi-

tional control unit in the aim of such scanning or choosing of required in the investigations fixed spectral wave length. Nowadays this unit is unsuitable for applications. The matter is that the resource base of electronic components are now out of date in this unit. It leads to unreliable performance over a long period of the operating time. Therefore, in the recent scientific studies such units must be improved in the purpose of the experiment automatization.

The main aim of this paper is the development of the remote control system on the base of two Atmel microcontrollers ATtiny 2313. This device is dedicated to the spectrum scanning of monochromators by the step motor ШДР-711. The principal performance availability of the seven segment light emitting diode (LED) indicator for the purpose of the current position indication of the diffraction grating is considered.

Development and discussion

The application of unconditional logic on the base of JK triggers and logic functions [4] is a prototype of systems of step motor control. The principal feature of this approach is the determination of triggers truth tables, which define the required pulses sequence. The micrologic are used with the aim to switch the direction of motor rotation. As a variant of such systems on the base of unconditional logic is an application of Erasable Programmable Logic Device (EPLD) [1, 2]. It enclosed the counters, summarizers, triggers, multiplexors, registers etc. The distinctive feature in a comparison with a previous control approach is an application of programmable chip as logic unit. It provides the required switching of step motor windings on the base of software algorithm. The application of special-purpose Pulse-Duration Modulation (PMD) controllers [9] is a next one another approach in a step motor control. In this case the software algorithm of individual model or type motor is designed. Whole technical features and performance specification of this motor are taken into account in such algorithm to form control signals. But a complicity, a specificity, relatively high cost and limitation of functional capabilities are principal disadvantages in such control system. Therefore an application of universal microcontrollers, in particular PIC16F84 [8] or HT46R47 [7], is a most optimal variant of control system development. The design of software algorithm by assembler language is a principal advantage in this case. It gives by-turn the possibility to perform the adjustment of motor

operating parameters. Moreover, it is possible to enhance the functional capabilities of algorithm by new additionally parameters. Herewith the universality of developed algorithm is provided. But such controllers have essential disadvantage. All instructions are executed per four clock cycles. It caused the considerably decrease of performance during program execution. This problem is solved in Atmel general-purpose microcontrollers AVR [9]. About appropriateness and effectiveness of such microcontrollers application indicates such list of advantages: inexpensive, more than 100 instructions to developing of the software algorithm, accessibility of large amount of the built-in peripheral equipment as well as system of serial input-output ports and interfaces as well [3].

We developed the remote control system on the base of such controllers. In Fig. 1 the block diagram of suggested system is shown.

Two Atmel microcontrollers ATtiny 2313 are used as the base elements of this system. The microcontroller (1) (MC1) is destined for the control of the step motor ШДР 711 and the rate of rotation (9 values). This rate can be graded in the range 0,2 nm/s – 80 nm/s. The microcontroller (2) (MC2) is destined for the processing of control monochromators signals and the indication of the current position of the diffraction grating in spectrum as well. The next control signals of monochromators are used: limit sensors (3, 4) of the diffraction grating and the benchmark units (5, 6) – calibration signals in grating passage through wavelength 0,1 nm and 1 nm. The serial interface USI is used to provide the communication between both microcontrollers. The information about scanning rate is transferred from (1) to (2) in the reload mode. Motor stoppage signals in the operating mode and acquisition signals of current spectrum value for the purpose of the monochromator adjustment in the reload mode as well are transmitted from (2) to (1).

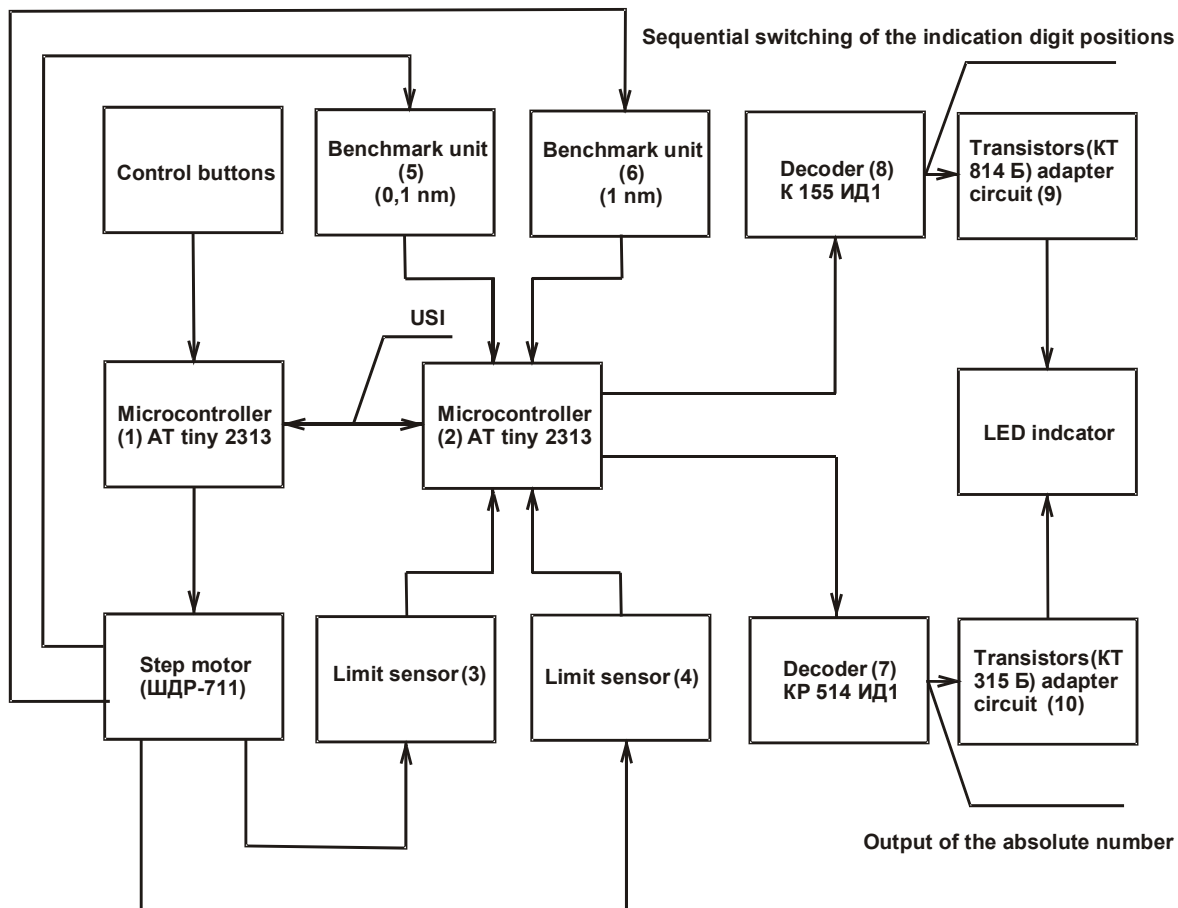


Fig. 1. The remote control system of monochromators MDR 12/23

The connected to MC1 control buttons are used to set the appropriate rate and the direction of scanning and to start-stop motor as well. The indication of the value of the scanning rate (1 digit position) and of the position of the diffraction grating in spectrum (4 digit positions and 1 light-emitting diode as well) is realized on the light-emitting diode display (LED indicator).

The software multiplex mode is used in the indication scheme. It realized on the controller (2). There are two decoders in this scheme: decoder (8) is destined for the sequential switching of the indication digit positions; decoder (7) is destined for the output of the absolute number to the active LED indicator. As soon as the output power of decoders is insignificant, the transistors adapter circuits are used for the connection to LED indicator unit.

The software algorithm of microcontroller (1) (MC1) (the control of the step motor)

Let us mark out the base functional levels of the software algorithm of microcontroller (1) (see Fig.2). The main program is the base element in the block diagram. It performs such functions:

- 1) the configuration of performance parameters of the built-in peripheral equipment;
- 2) processing of signals which are inputted to the controller from the buttons unit;
- 3) the subprograms call and coordination of their performance.

The subprograms are as a separate program modules which are destined for the execution of the separate functions of algorithm:

- 1) the control of the step motor;
- 2) data exchange by interface USI;
- 3) the operation with memory EEPROM (data write and read).

The next built-in peripheral equipment and registers are used in program operation

- 1) general-purpose registers R16-R24;
- 2) registers of 8-bit timer/counter T0:
 - a. coincidence registers OCR0A, OCR0B;
 - b. counter register TCNT0;
 - c. control registers TCCR0A, TCCR0B;
 - d. register of interrupts mask TIMSK;
- 3) input-output ports:
 - a. data registers PORTB (8-bit port B) and PORTD (7-bit port D);
 - b. registers of data direction DDRB (port B) and DDRD (port D);
- 4) 8-bit register of stack pointer SPL;
- 5) Random Access Memory (RAM): addresses of storage (memory) cells 0x60, 0x61;

During the process of program loading the configuration of performance parameters of the built-in peripheral equipment is realized:

- 1) the initialization of general-purpose registers (R16-R24);

- 2) the backup of storage cells of memory RAM;
- 3) the configuration of stack;
- 4) the configuration of input-output ports;
- 5) the configuration of timer T0;

The main task of MC1 program is the control of the step motor. The last one is operated in a two-phase winding switching mode. The timer T0 is used for this purpose. There are two coincidence registers OCR0A and OCR0B in this timer.

The timer T0 is operated as a counter [5]. If its count of pulses, which are inputted from the clock oscillator of MC1, coincides with the content of one of two registers OCR0A or OCR0B then the interrupt is generated. In this case the value of number in OCR0A is always more than in OCR0B.

In our case the register OCR0A is used to specify the frequency of control signal pulses of the step motor. And the register OCR0B is used to change their phase. The interrupts themselves are destined to call the subprogram which specifies according leads of port B (PB0-PB3) to binary one ("1") or binary zero ("0").

After the specifying of performance parameters of the built-in peripheral equipment the entry of signals from the buttons unit is testified:

1) *depressed button S1*: the rate of rotation (9 values) of motor performance is specified by variation of generated signals frequency (phase is stationary). Two parameters, which will be loaded into registers OCR0A and OCR0B, are sequentially read out from storage cell of memory EEPROM. These are two constants which values are fitted in such a way that fixed phase quadrature between control pulses is provided. If the rotation direction is changed then the loading order of constants into coincidence registers will be backward;

2) *depressed button S2*: the direction of motor rotation is specified. This parameter is able to take two values (1 – clockwise motor rotation, and 0 – counterclockwise motor rotation);

3) *depressed button S3*: interrupt enable of timer T0. The motor starts to rotate in the specified direction and at re-depressed button S3 – motor's stop is realized (interrupts are disable).

The motor phases are separated on the program level. If the interrupt is caused by the coincidence in register OCR0A, then the leads PB0 and PB2 of port B are set to "1" and to "0", accordingly (on repeated interrupt the swapping of 1 and 0 is realised). If the interrupt is caused by the coincidence in register OCR0B, then the leads PB1 and PB3 of port B are set to "1" and to "0" (on repeated interrupt the swapping of 1 and 0 is realized as well). So, two motor windings are simultaneously enclosed, which are sequential switching.

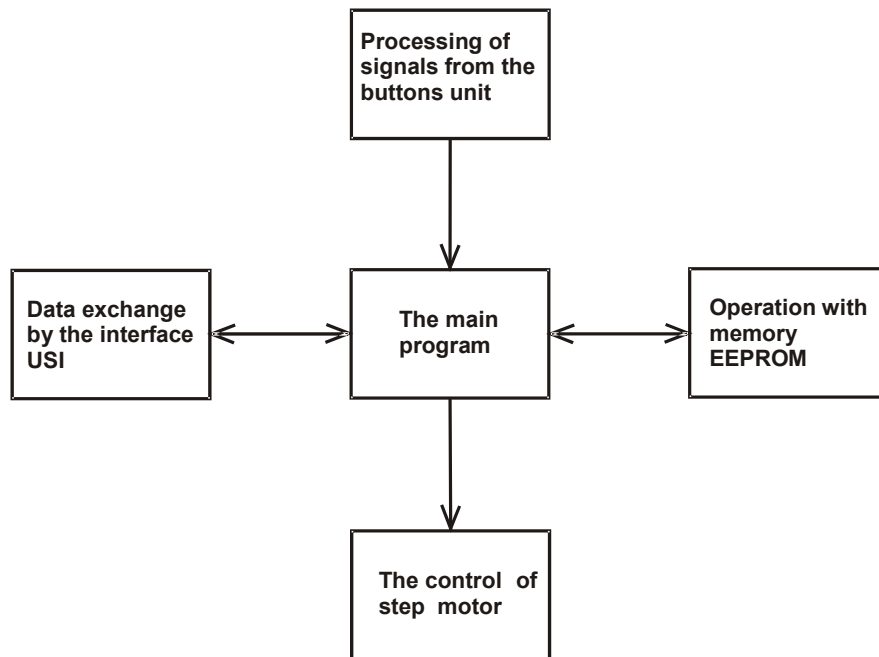


Fig. 2. Function levels of software algorithm of the microcontroller 1 (control of the step motor)

The software algorithm of microcontroller (2) (MC2) (information signal processing and indication) (Fig. 3)

The next built-in peripheral equipment and registers are used in the controller operation:

- 1) general-purpose registers R16-R25, R30;
- 2) registers of 8-bit timer/counter T0:
 - a. coincidence register OCR0A;
 - b. counter register TCNT0;
 - c. control registers TCCR0A, TCCR0B;
 - d. register of interrupts mask TIMSK;
- 3) input-output ports:
 - a. data registers PORTB (8-bit port B) and PORTD (7-bit port D);
 - b. registers of data direction DDRB (port B) and DDRD (port D);
- 4) 8-bit register of stack pointer SPL;
- 5) Random Access Memory (RAM): addresses of storage (memory) cells 0x60-0x67;
- 6) registers of external interrupts:
 - a. main register of interrupts mask GIMSK;
 - b. register of mask interrupts on sweep at the arbitrary contacts – PCMSK;

The main tasks of MC2 program are next:

- 1) to perform the processing of signals from limit sensors;
- 2) to perform the processing of signals from benchmark units;
- 3) to perform the output of the absolute number to the LED indicators.

Initially the adjustment of monochromator is performed. The signal from one of two limit sensors (the leads PB2-PB3 of port B) is waiting to realize it. In so doing the setting of program counter of benchmark unit pulses (channel 0,1 nm) to 200 or 2000 (according to the wavelength in nm) is performed. The output of the absolute number to the LED indicators is enabling after this procedure.

Signals from the benchmark unit (accurate within 0,1 nm) are used to pulses count by program counter. If the logical level is low at the lead PBO, then value of counter is incremented. But sometimes in this benchmark unit operation the error can be realized. The last one will cause the incorrect pulses count. As the results the obtained number can be more (or less) than it is in real situation. To

solve this problem the additional benchmark unit with step of 1 nm is used. At moments, when the logical level is low at the lead PB1, the program is testing of the counter's content. If its value is other than ten, then the correction is performed.

The pulses count is performed in the order of digit-to-digit operation:

- 1) if lower order digit has nine value (in a result of addition), then it sets to zero and high-order digit is incremented etc.;
- 2) if high-order digit has unit value (in a result of subtraction), then it sets to zero and lower order digit is set to nine etc.

To store the every value of number the one-dimensional array is used. It is formed by storage cells of memory RAM (every address of cell corresponds to single digit of result number).

The value of the rotation rate is stored in the separate cell of memory RAM (in the next cell after wavelength).

With the aim of software realization of dynamical indication mode it is necessary to form at the output of port B the special binary code. It will be provide simultaneously such functions:

- 1) switching of digit positions of indication unit;
- 2) output of digit to the necessary indicator.

For this purpose only register OCR0A of timer T0 is used. The content of this register will define the frequency of switching of indication unit digits (100 Hz). During the every process of interrupt the sequentially reading of storage cells of memory RAM (according to addresses) is realized. The content of these cells will be inputted to the leads PD0-PD3 of port D. The high-order bits (PD4-PD6) of this port are responsible for the switching of digit positions of indication unit. The values of numbers from 0 to 4 are sequentially inputted to these leads (accordingly to the number of used digit positions).

The forming of resulting binary code is realized in the next manner:

- 1) the separate program counter is counting from 0 to 4 (the content of this counter is stored as single byte);
- 2) then tetrads of this byte are swapped;
- 3) new (obtained) value of this byte is logically added with a number from the storage cell of memory RAM.

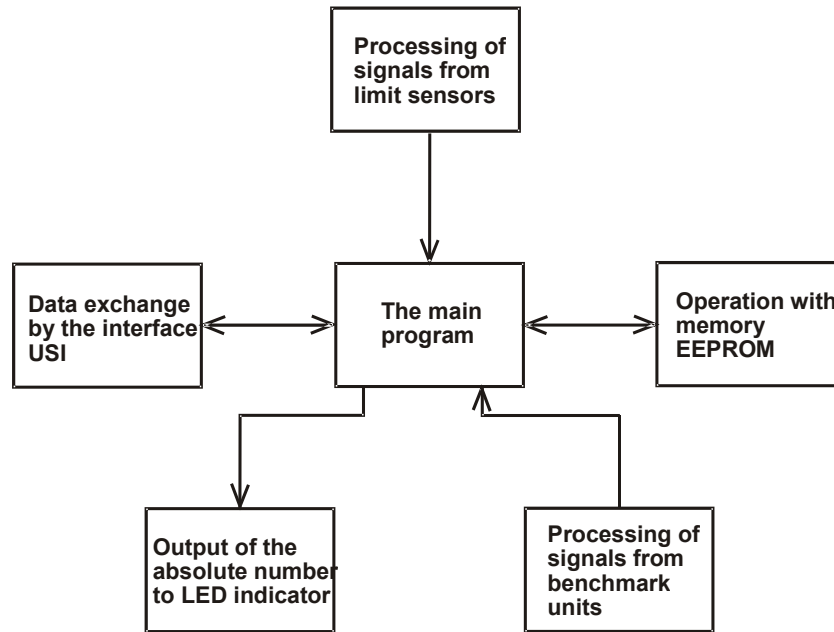


Fig. 3. Function levels of software algorithm of the microcontroller 2 (processing of monochromator signals and indication)

Let us consider, as an example, the outputting of absolute numbers 1468 (the wavelength in angstroms without of fifth high-order digit position, which is outputted by the light-emitting diode) and 7 (the rate of scanning) to LED indicator array by assistance of port B of microcontroller 2. The leads

PORTB0 – PORTB3 are destined to outputting of the digit to a single digit position; the leads PORTB4 – PORTB6 are used to switch of digit positions of indication unit. These values will correspond to absolute number 14687 (5 digit positions) in a case of dynamical indication (see Fig.4).

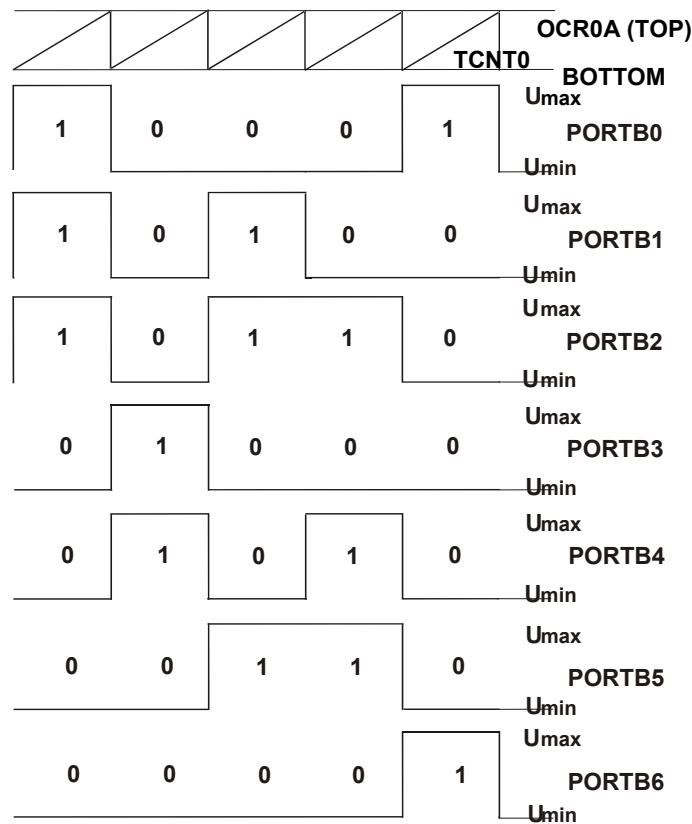


Fig. 4. The forming of resulting binary code for the indication

Conclusions

The remote control system of monochromator MDR 12/23 at the base of two universal Atmel microcontrollers ATtiny2313 was developed. The special original software

algorithms of these controllers are designed to provide the next functional capabilities:

the control of the step motor of type ШДР-711. The current in each winding is up to 2,5 A. It is sufficient for this type motors operation;

the discrete change (9 positions) of scanning rate in the both directions (the step frequency is up to 400 Hz);

the dynamical indication of wavelength (four decimal digit positions) and rate of spectrum scanning (single decimal digit position).

1. Вычужанин В. В. Устройства для управления шаговым двигателем на ПЛИС // Технология и конструирование в электронной аппаратуре. – 2006. – №3. – С. 17–20. 2. Вычужанин. В. В. Шаговый двигатель, управляемый на ПЛИС // Современная электроника. – 2007. – № 9. – С. 22–25. 3. Евстифеев А. В. Микроконтроллеры AVR семейств Тiny и Mega фирмы "Atmel". – М., Издательский дом "Додэка-XXI". – 2004. 4. Ке-

ню. Т. Шаговые двигатели и их микропроцессорные системы управления. – М., Энергоатомиздат, 1987. 5. Клещик М. М., Фесенко С. О., Борецкий В. Ф., Веклич А. М. Використання мікроконтролера ATtiny 2313 для розгортки спектру монохроматора // Вісник Київського університету, Серія: фізико-математичні науки. – 2009 (надіслано до друку). 6. Пушкарёв О. Драйверы шаговых двигателей фирмы Allegro // Современная электроника. – 2004. – № 12. – С. 22-25. 7. Чиа В. Ш. Компоненты и технологи. – 2004. – № 9. – С. 136-139. 8. Яценков. В.С. Микроконтроллеры MicroChip. Практическое руководство. – М., Горячая линия-телеком. – 2002. 9. Application Example and Algorithm AVR360: Step Motor Controller. – http://www.atmel.com/dyn/resources/prod_documents/doc1181.pdf.

Manuscript received June 20, 2009

UDC 533.932

A. Knurenko, postgraduate stud.
E. Martysh, as. prof.

COMPARISON OF PLANETARY MAGNETOSPHERES

В роботі представлені результати порівняльного аналізу магнітосфер таких планет: Меркурій, Земля, Уран, Юпітер. Розглянуто особливості поведінки магнітосферної плазми в залежності від величини магнітного поля. Показано механізми і роль перезамикання магнітних ліній у плазмових процесах.

Ключові слова: плазма, магнітосфера, перезамикання, магнітне поле.

In this work we present the results of comparative analysis of magnetospheres of the following planets: Mercury, Earth, Uranus, and Jupiter. Features of magnetosphere plasma behavior depending on the strength of magnetic field are reviewed. Mechanisms of the magnetic lines reconnection and its role in plasma processed are described.

Keywords: plasma, magnetosphere, reconnection, magnetic field.

Introduction. The study of the solar wind interaction with planetary magnetospheres basically is the investigation of the physics of flowing magnetized plasmas. Thus the Mercury, the Earth, the Uranus, and the Jupiter might all interact in much the same way except for some differences in the shapes of the magnetosphere obstacles to the flow. There are major differences however. Some of these are due to the varied driving forces and boundary conditions at each planet. Some of these are due to differences caused by their varied sizes relative to gyroradius of the ions [1]. Microscale process on both the ion and the electron scale matter greatly. It is clearly seen obvious that reconnection must be influenced by electron kinetics, and just as clearly reconnection influences the flow patterns throughout planetary magnetospheres. It is also evident from the controversies surrounding its functional dependences that reconnection is poorly understood.

Reconnection is the process whereby magnetic field lines from different magnetic domains are spliced to one another, changing their patterns of connectivity with respect to the sources. It is a violation of an approximate conservation law in plasma physics. The most common type of magnetic reconnection is separator reconnection, in which four separate magnetic domains exchange magnetic field lines. Reconnection plays an important role in the energetics of the magnetospheres of both magnetized and unmagnetized planets, but it seems to play the most dominant role in the dynamics of the magnetized planets. Most of our observations of magnetized planets have been obtained at the Jupiter and the Earth. The magnetospheres of the Earth and the Jupiter both undergo substorm-like cycles as part of an unsteady magnetosphere-wide circulation despite the fact that they are driven by quite different processes: the solar wind interaction in the case of the Earth and mass loading by the moon I_0 in the case of Jupiter. Each magnetosphere provides lessons for the other and together they give a clearer insight as to how reconnection works at a magnetized planet.

Mercury. The Planet Mercury is the closest planet to our Sun and is the smallest planet in the solar system. It has no natural satellites and no substantial atmosphere.

Despite its small size and slow 59-day-long rotation, Mercury has a significant, and apparently global, magnetic field. The magnetic field strength at the Mercurian equator is about 320 nT. Like that of Earth, Mercury's magnetic field is dipolar in nature. Mercury's magnetosphere is the smallest. The body of this planet occupies much of the volume of the magnetosphere. Fig. 1 shows the magnetosphere of the Mercury.

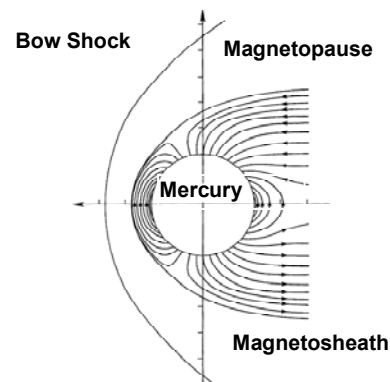


Fig. 1. The magnetosphere of Mercury

Its field lines are anchored in the electrically conducting interior of Mercury and not in a conducting ionosphere. In contrast to other planetary magnetospheres this magnetosphere is very sensitive to the force of the solar wind dynamic pressure that controls the size of the magnetosphere.

The substorm example illustrates how we can start to understand Mercury's magnetosphere from understanding of terrestrial processes but does not show how we learn more about processes by their intercomparison at the two bodies. To do this we turn to another process if do it, the creation of flux transfer events on the dayside magnetopause.

The Earth. While Mercury provides us with new goals and objectives in planetary research to which we should send our next generation of exploratory vehicles, we also can explore new goals in a complementary dimension at

the Earth. Terrestrial exploration enables us to investigate magnetosphere's processes in much greater detail because more resources can be invested in the payload and less in the vehicle and spacecraft launch when the destination is the Earth's orbit. With few exceptions the phenomenology of the terrestrial magnetosphere is well explored.

The most important poorly understood mechanism is reconnection that allows topological changes in the magnetized plasma leading to energy and mass transfer with the solar wind.

The Earth's magnetosphere is over an order of magnitude larger than Mercury's. The body of the Earth occupies small part of the volume of the magnetosphere. Fig. 2 shows the Earth's magnetosphere.

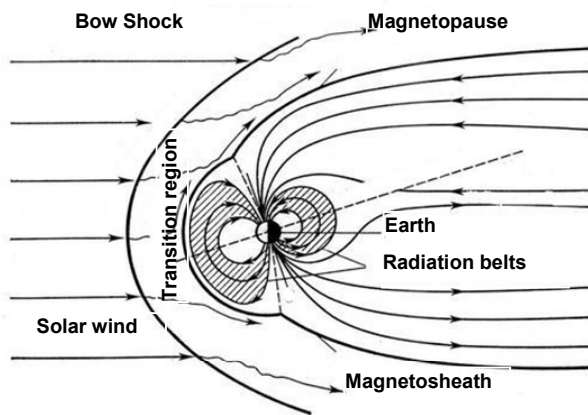


Fig. 2. The magnetosphere of the Earth

The Earth has a magnetic field with north and south poles. As the Earth rotates, its hot core generates strong electric currents that produce the magnetic field. This field reaches 70,000 km (which varies with solar wind intensity) or 10-12 Earth radii into space to the border of interaction with solar wind. The magnetosphere prevents most of the particles carried in solar wind, from impacting the Earth. The solar wind distorts the shape of the magnetosphere by compressing it at the front and forming a long tail on the side away from the Sun. This long tail is called the magnetosphere tail. Some particles from the solar wind can enter the magnetosphere. The particles that enter from the magnetosphere tail travel toward the Earth and create the auroral oval light shows.

Uranus. The magnetosphere of Uranus is medium sized. It holds all of Uranus' moons. The magnetosphere of Uranus has a very strange tilt. Fig. 3 shows the tilt of the magnetosphere of Uranus.

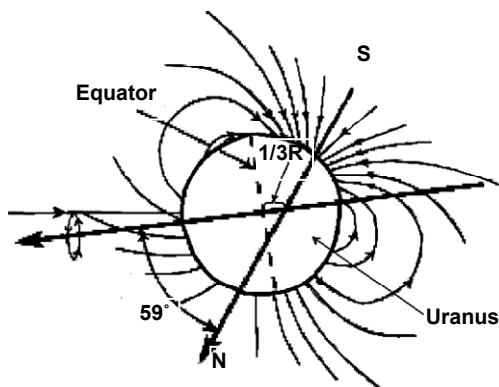


Fig. 3. The tilt of the magnetosphere of Uranus

The axis of the field (an imaginary line connecting its north and south poles) is tilted 59 degrees from the planet's axis of rotation. The extreme tilt, combined with the extreme tilt of Uranus itself, makes for a completely strange magnetosphere. The body of this planet occupies not much and not little of the magnetosphere's volume.

The Jupiter. The Jupiter's magnetosphere is the largest and most powerful of any planetary magnetosphere in the Solar System. The Jupiter's magnetic field is stronger than that of the Earth by an order of magnitude. It is a synchronous orbit, where gravity and centrifugal force balance. It lies deep inside the magnetosphere, about 2% of the way to the magnetopause. Most important is that Jupiter's magnetosphere has a strong source of ions deep in the magnetosphere, but well outside of synchronous orbit, that are accelerated to high velocities. The body of this planet occupies just a bit of the volume of the magnetosphere. Fig. 4 shows the magnetosphere of the Jupiter.

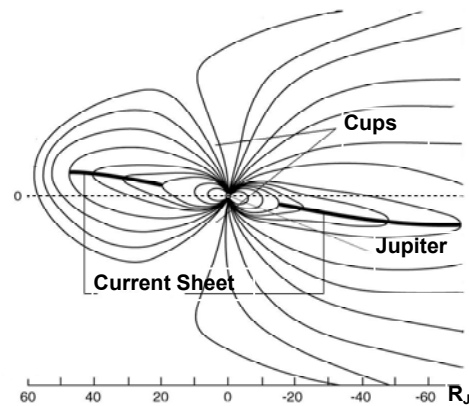


Fig. 4. The magnetosphere of Jupiter

The effect of Jupiter's rapid rotation is a disk-like distortion of the magnetic field that occurs because of an intense 1000 kg/s ion source at Io. Centrifugal force is important because Jupiter rotates 2.5 times faster than the Earth and because the length scale of the Jupiter's magnetosphere is 100 times larger than that of the Earth.

The mass source is well beyond the Jupiter's synchronous orbit where corotating particles have a net outward force in the rotating frame but still very far from the magnetopause. The maintenance of a steady state requires an existence a mechanism to separate the mass-loaded ions from their flux tubes. This requirement in turn forces a circulation pattern in which plasma moves radially outward from Jupiter.

When the mass-laden flux tubes reach the tail, reconnection produces plasma islands with circular field lines and empty flux tubes that are buoyant. The plasma islands can be lost and the buoyant flux tubes can return to the inner magnetosphere to become mass-loaded again.

Io is the engine that drives this magnetosphere's circulation and powers the magnetosphere by tapping the rotational energy of the planet. Ultimately the rate of volcanism on Io controls the mass loading rate and therefore the power flowing into the processes of magnetosphere. The way Io accomplishes this is very interesting and provides some insight into working of astrophysical rotators, even though certain details may differ from the Jupiter's situation.

Reconnection in the Jupiter's and the Earth's magnetosphere. The most common type of magnetic reconnection is separator reconnection, in which four separate magnetic domains exchange magnetic field lines. Do-

mains in a magnetic plasma are separated by separatrix surfaces: curved surfaces in space that divide different bundles of flux. The reconnection mechanism itself depends on the processes that take place on the smallest scales conceivable in a plasma, on the electron inertial length, but everything we need to know to understand the dynamics of the magnetosphere can be determined from the macroscale [2]. This occurs because the system evolves to the microphysical state required to enable reconnection. This is not to say that reconnection is independent of plasma conditions but that a planetary magnetosphere can create reconnection when it is required to complete its plasma circulation patterns. Locations and rates may be controlled by the plasma and field configurations but reconnection happens at least at some rate quite readily. The magnetic field at JO is very strong but the density builds up in the torus until a circulation patterns are established that transports ions outward so that they can be lost from the magnetosphere. In the Earth's magnetosphere ions are lost from the dayside magnetosphere but at Jupiter, partially because of the inefficiency of reconnection on the magnetopause, the ion loss process occurs on the nightside of the planet Jupiter. The result of this rapidly spinning, outwardly convecting magnetosphere is the Jupiter's magnetosheath sketched in Figure 4. Beyond about 25 R_J a thin current sheet is formed with almost vacuum conditions above and below the field reversing current sheet. This is an ideal situation for the occurrence of reconnection and indeed the correlated flows and reversed normal component of the magnetic field expected for reconnection have been seen.

Conclusions. This comparison of the Earth's magnetosphere and two extrema, the Mercury's magnetosphere and the Jupiter's magnetosphere teaches us much about how magnetospheres work and how the controlling processes behave. Table 1 lists what we believe are the important processes at each planet.

Table 1. Important processes in planetary magnetospheres

	Reconnection	Energy Storage		Magnetosphere- ionosphere coupling	Fast neutral transport
		Mag fields	Particles		
The Mercury	+	?	-	-	+
The Earth	+	+	+	+	-
The Uranus	+	+	+	+	+
The Jupiter	+	+	+	+	+

At the Mercury reconnection is clearly the dominant mechanism for driving the circulation of the magnetosphere and energizing the particles. Fast neutral transport is im-

portant at Mercury because its tenuous atmosphere may be greatly affected by this mechanism and because of the diagnostic ability of certain trace neutral gases such as sodium and potassium, whose motion and spatial extent can be imaged from the Earth. The magnetosphere of Uranus is medium sized.

At Jupiter all processes listed in Table 1 are important. Reconnection at the magnetopause appears to allow the tail to be at least partially open and becomes very important in dumping ions down the tail. The magnetodisk stores energy in the corotating plasma and the stretched field. The acceleration of the Io-genic ions occurs via field-aligned currents closing in the ionosphere and fast neutrals from Io transport mass throughout the Io torus. Table 2 lists what we believe are the important parameters at each planet.

Table 2. Important parameters in planetary magnetospheres

Planetary Parameter	The Mercury	The Earth	The Uranus	The Jupiter
Rotation period	58.65d	23 ^h 56 ^m	17 ^h 14 ^m	9.925 ^h
Mass, kg	3.3022 × 10 ²³	5.9736 × 10 ²⁴	8.6810 × 10 ²⁵	1.8986 × 10 ²⁷
Characteristic time IMF	-----	8m	-----	30s
Mean density, g/cm ³	5.427	5.5153	1.27	1.326
Equatorial rotation velocity, km/h	10.892	1674.4	9320	45300
Mean radius, km	2439.7	6371.0	25559	71492

Reconnection plays a fundamental role in circulation of the plasma in both the terrestrial and Jupiter's magnetospheres even though the engines that drive the circulation are quite different. In both magnetospheres time varying reconnection causes substorm-like behavior. While the behavior of the Earth's magnetotail can often appear very puzzling, the appreciation that the Earth's magnetotail can contain two (or more) neutral points helps explain these phenomena. In particular the reconnection rate associated with the nearest neutral point can be controlled by the more distant one. At the Earth reconnection is also important leading to the storage of energy the magnetotail and to the circulation and energization of the plasma well inside the magnetosphere leading to the buildup of the ring current, the signature of the geomagnetic storms.

1. Russell C.T., New horizons in planetary magneto-spheres // Advances in Space Research – 2006, Vol. 37, 2. Russell C.T., Reconnection in planetary magneto-spheres // A& Space Res. – 2002, Vol. 29, No. 7, 3. Russell C.T., How northward turning of the IMF can lead to substorm expansion onsets // Geophys. Res. Lett. – 2000, Vol. 27.

Submitted on 20.06.09

UDC 537.86 / 87

V. Kobeliatskyi, stud., G. Melkov, D.Sci.,
V. Moiseienko, stud., O. Prokopenko, Ph.D.**CORRELATION RECEIVER WITH WAVE FRONT REVERSAL OF MAGNETOSTATIC WAVES**

The method of correlation signal processing, based on nonlinear interaction of signal magnetostatic waves (MSW) of the frequency ω_s with an electromagnetic pumping of double signal frequency in yttrium-iron garnet (YIG) films, is presented. The output nonlinear correlation signal appears at the frequency of input signal and the signal-to-noise ratio enhanced by frequency and power of the electromagnetic pumping. The case of rectangular MSW pulses correlation in 6-cm band is considered.

Key words: spin waves, parametric interaction, correlation.

В роботі представлено метод кореляційної обробки інформації, який базується на нелінійній взаємодії сигналів магнітостатичних хвиль частотою ω_s з електромагнітною накачкою на подвійній частоті в плівках залізо-ітрієвого гранату. Потужність вихідного сигналу кореляції залежить від частоти та тривалості накачки. Дослідження проводились в шести сантиметровому діапазоні довжин хвиль.

Ключові слова: спінові хвилі, параметрична взаємодія, кореляція.

Introduction. There is a problem of how to extract a weak useful signal from the noise level in communication systems. A low-level noise (accordingly to the signal level) typically can be eliminated by the use of amplitude discriminator with threshold greater than the noise level [2]. But often noise signal have the amplitude greater than the amplitude of useful signal. In such case the increase of the discriminator threshold level can increase the probability of "cut" the useful signal. And so the question "How to select the useful signal from a set of other signals (noise) with maximum precision?" remains actual for the modern communication systems. In that case the use of correlation signal processing is very effective [1–2]. In paper the method of correlation signal processing based on nonlinear interaction of signal magnetostatic waves (MSW) of the frequency ω_s with an electromagnetic pumping of double signal frequency $\omega_p = 2\omega_s$ in yttrium-iron garnet (YIG) films, is presented. The case of rectangular MSW pulses correlation in YIG films is considered.

One of the most effective methods of detection and reception of a useful signal $S(t)$ dependent on time t and buried in noise $N(t)$ is the method based on the measurement of the signal correlation function $B(\tau)$:

$$B(\tau) = \int_{-\infty}^{+\infty} [S(t) + N(t)] F(t + \tau) dt \equiv \int_{-\infty}^{+\infty} \eta(t) F(t + \tau) dt, \quad (1)$$

where τ is the signal time delay. The signal-to-noise ratio (SNR) at the input can be evaluated as $SNR = S^2(t) / \langle N^2(t) \rangle$. It is clear from (1) that the process of correlation reception is based on the operation of multiplication of the received signal $\eta(t) = S(t) + N(t)$ (consisting of the sum of useful signal and noise) by the reference time-delayed signal $F(t + \tau)$ and the following integration of the product in the time domain. Thus, the resulting correlation function (1) is a sum of the auto-correlation function of the signal $S(t)$ and the cross-correlation function of the signal $S(t)$ and noise $N(t)$. It is known that the influence of noise on the correlation function $B(\tau)$ is decreased exponentially with the increase of the delay time τ , and when $\tau \rightarrow \infty$ there is a theoretical possibility to receive a weak harmonic signal on the background of an arbitrarily strong noise [1].

Main part. If at the moment of time $t = 0$ the microwave signal with frequency ω_s is applied to the input antenna, it will excite spin waves in the film with group velocity $\approx 3 \text{ cm}/\mu\text{s}$; these waves propagates toward the output antenna (see Fig. 1). At the moment of time $t = T_p$ a pulse of an electromagnetic pumping with double frequency $\omega_p = 2\omega_s$ is applied to the open dielectric resonator (ODR). As the result of interaction of input and pumping signals, photon corresponded to an electromagnetic pumping is decayed to the two magnons of half frequency. So the energy and impulse conservation laws can be written as:

$$\begin{aligned} \omega_p &= \omega_s + \omega_r, \\ \vec{k}_p &= \vec{k}_s + \vec{k}_r, \end{aligned} \quad (2)$$

where $\vec{k}_r = -\vec{k}_s$. Anyone can see the wave with frequency ω_r , formed due the interaction process, propagates back to the input antenna. It is almost identical to the amplified by pumping input wave, but inverted in time in respect of input wave; so the wave with frequency ω_r is phase-conjugated wave.

Amplitude of wave-front reversal (WFR) signal can be regulated by power of the pumping; the increase of power lead to the increase of amplitude of WFR signal, but this dependence is not linear. For relatively small pumping power the WFR signal has a rectangular form and it is wider in time than the input signal by 2 times. This specialty was used for time dilatation of MSW pulses [6]. The further increase of pumping power will lead to the conversion of WFR signal to the "bell-like" form due to the better amplification of frequency components near $\omega_p / 2 = \omega_s$ by pumping than other spectral components of input signal. Further increase of pumping power will lead to the parametric excitation of spin waves with high amplitudes. These waves will do influence on the quality factor of the resonator and will lead to the reduction of the Q-factor. This process limits the effectiveness of energy pumping in YIG film by the resonator. This process becomes significant when a "chip" on a pumping pulse appears. This effect is deleterious for the application of magnetostatic waves, so the operating in the power band, where the amplitude of WFR signal linearly depends on power is more convenient.

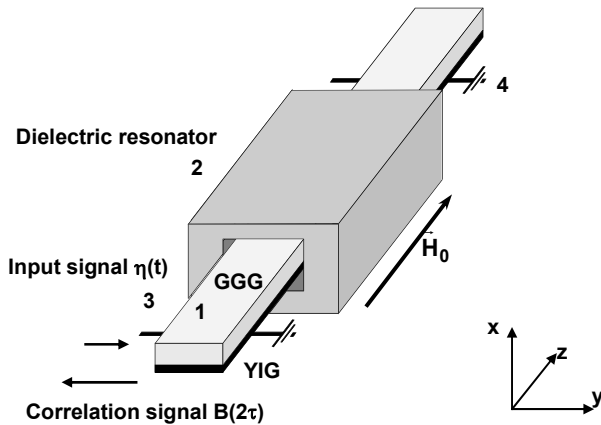


Fig. 1. Layout of the microwave convolver.
 1 – YIG film waveguide grown on gallium-gadolinium garnet (GGG) substrate; 2 – open dielectric resonator; 3 and 4 – wire antennas supplying input signal

The matching YIG film and microstrip transmission line (antennas) is an important factor. Typically only 30% of microwave energy transmitted into the film, the other 70% of energy is reflected. Due to this effect the performance of correlation receiver is greatly decreases, so the precise matching technique was used to achieve good performance results.

If a sum of rectangular form useful signal and noise is applied at the input of the correlator, shown in Fig. 1, and $SNR < 1$, then, first of all, the film will operate as a microwave filter and will eliminate all spectral components out of its pass band for the given magnetic field. So the output signal, received from the film, will be rectangular signal with low noise level; after that some threshold device can register this signal. If a pumping signal will also be applied to the ODR, the WFR signal and a, that is the correlation signal, can be registered. In this case the WFR signal is the correlation signal. In that case the input correlation signal is integrated by the output antenna. While more magnons incoming to the antenna, than higher current is excited in the antenna, and so the higher power of correlator output gained from a square detector. The power of this signal depends on pumping power and the frequency of input signal (nonresonant WFR [5]). The main principle of operation of such correlation receiver is the parametric interaction of magnetostatic spin waves in YIG films. It is known similar systems based on parametric interaction of acoustic and spin waves [4, 7].

$$\omega_k^2 \equiv \omega_H \left[\omega_H + \omega_M \left(1 - e^{-kd} \right) / kd \right]$$

of the lowest width mode of backward volume MSW (BVMSW) (or dipolar spin waves) in the YIG waveguide, τ is the delay time of the reference signal, l is the distance between the two input antennae 3 and 4 in Fig.1, $z = 0$ and $z = l$ are positions of the antennae along the length of the YIG waveguide, d is the thickness of the YIG film, $\omega_H = \gamma H_0$, H_0 is the external bias magnetic field, $\omega_M = 4\pi\gamma M_0$, M_0 is the static magnetization of YIG, and γ is the modulus of the gyromagnetic ratio for the electron spin.

For the experimental realization of the correlation operation (1) on the signals $\eta(t)$ and $F(t + \tau)$ we used the ferrite microwave convolver developed in our earlier work [3]. This convolver is based on the YIG film waveguide having dimensions $5.1 \mu\text{m} \times 1 \text{mm} \times 10 \text{mm}$, magnetized along its longest

side by the external bias magnetic field $H_0 = 967 \text{ Oe}$, and placed inside an ODR (see Fig.1). This geometry corresponds to the excitation of BVMSW propagating along the bias field direction in the YIG waveguide. Two wire antennae of the diameter of $25 \mu\text{m}$ are situated near the opposite ends of the waveguide at a distance of 6 mm between them.

In our experiments the input signal $\eta(t) \exp(j\omega_s t)$ was supplied to the first input antenna 3 and created a microwave magnetic field $h_s(t) = f(\eta(t))$, which excited in the YIG film waveguide BVMSW wave packet $a_s(t, z) = L\eta(t) \exp(j\omega_s t - k_s z)$ having carrier frequency ω_s and carrier wave number k_s . The coefficient L describes the efficiency of transformation of the input electromagnetic signal $\eta(t)$ into the BVMSW packet $a_s(t, z)$ propagating along the waveguide length z . Due to the parametric interaction of signal wave with pumping a time reversal signal $F(t) \exp(j\omega_r t)$ is generated; it creates a microwave magnetic field $h_r(t) = f(F(t))$, which excited in the YIG film waveguide BVMSW wave packet $a_r(t, z) = LF(t) \exp(j\omega_r t + k_r z)$ having carrier frequency ω_r and carrier wave number k_r , which propagated along the axis z in the opposite direction.

Although wide band signals were used in the work, it is interesting to evaluate the pass band of proposed correlator. To do that we measure the device amplitude-frequency curve by using scalar network analyzer (Fig.2). The pass band is approximately 200 MHz at the level of 3 dB. Thus the signals with duration 10-100 ns, we have used, pass the system without significant losses, but the noise signals losses the major part of power. So, the correlator do a preliminary signal filtration. This effect exists due to the spin wave dispersion in YIG film. The waves with group velocity less than $3 \text{ cm}/\mu\text{s}$ decayed before the coming the antenna.

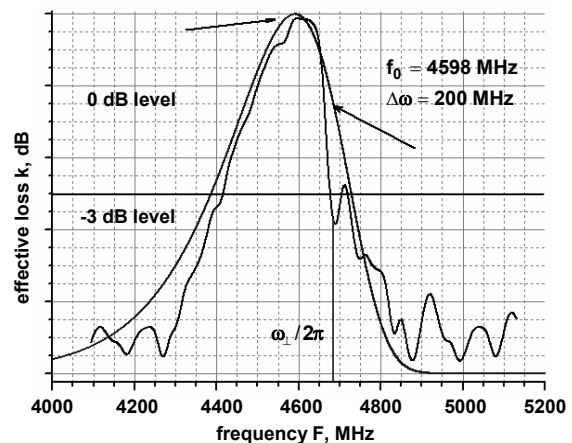


Fig. 2. Amplitude-frequency characteristics of correlator based on YIG film with thickness $5.1 \mu\text{m}$. The external dc magnetic field is $H_0 = 996 \text{ Oe}$

For theoretical description of correlator amplitude-frequency curve the approximate function

$$f(\omega) = \frac{1}{2\pi\Delta\omega} \exp\left(\frac{\omega - \omega_0}{2\pi\Delta\omega}\right) \exp\left(-\exp\left(\frac{\omega - \omega_0}{2\pi\Delta\omega}\right)\right), \quad (3)$$

has been chosen, where ω_0 – central angular frequency, $\Delta\omega$ – pass band width.

Theoretical expression for the correlation signal in the case the pumping is the reference signal, can be written from the system of parametric interaction of two spin waves:

$$\begin{cases} \frac{dC_k}{dt} = i\omega_k C_k + \Gamma_k C_k + iV_k h_p e^{i\omega_p t} C_{-k}^* \\ \frac{dC_{-k}^*}{dt} = -i\omega_k C_{-k}^* + \Gamma_k C_{-k}^* - iV_k h_p e^{-i\omega_p t} C_k \end{cases}, \quad (4)$$

where V_k – coefficient of parametric interaction of two spin waves (accounts as the constant), h_p – pumping field.

Correlation signal $B(2\tau)$ is phase-conjugated to the input signal in that case. It is the BVMSW wave front reversal signal and has a form:

$$B(2\tau) = C_{-k} = I(\omega_k) \exp\left(i\omega_k(t - \tau_p) + \frac{i\omega_p}{2}\tau_p - ik(z - 2l)\right) \times \exp\left(-\Gamma t + V_k h_p \tau_p - \frac{(\omega_k - \omega_p/2)^2}{2V_k h_p} \tau_p\right), \quad (5)$$

where τ_p – pumping duration. Input signal spectrum is

$$I(\omega_k) = \int_{-\infty}^{\infty} I(t) \exp\{i\omega_k t\} dt = \frac{2 \sin((\omega_k - \omega_s) \cdot \tau_s / 2)}{(\omega_k - \omega_s)}$$

The experimental envelopes of the input pulsed signal and reference pumping signal shown in Fig.3 were obtained using quadratic detectors connected to the input antenna 3 and to the ODR. The carrier frequencies f_s, f_p and powers P_s, P_p of the signals were: $f_s = 4700$ MHz, $f_p = 9400$ MHz, and $P_s = 1$ mW, $P_p = 5$ W.

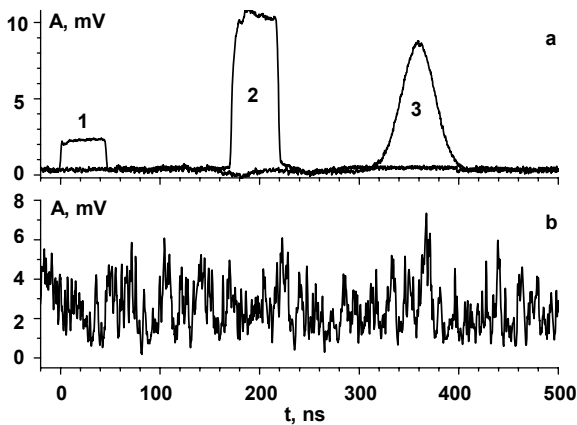


Fig. 3. Experimentally measured envelopes (solid lines) of the input and output signals of the correlation receiver shown in Fig.1 in the case of strong external noise: (a) input signal (1), pumping (2), output correlation signal (3) (SNR=10); (b) input pulsed signal mixed with strong external noise (SNR =0.1)

The main aim of our work was the demonstration of successful operation of correlation receiver on magnetostatic waves with WFR in YIG films and the receiving of signals with SNR less than 1. To demonstrate this we apply a microwave signal with rectangular form and power $P_s = 1$ mW (see Fig. 3a input signal (1)) and a noise signal with power $P_N = 10$ mW to the input antenna 3. The SNR was 0.1.

The noise signal had Gaussian profile with the central frequency ~ 4.7 GHz and its spectral width was exceeding 200 MHz. The total created signal is shown in Fig. 3b. When the signal propagating along the film reached the center of the ODR a pulse of longitudinal parametric pumping with power 5 W was applied (see Fig. 3a pumping (2)). As a result of interaction a WFR signal, the correlation signal, was generated. It was registered by input antenna and was amplified by 40 dB. The envelope of this signal, measured by a quadratic detector, is shown in Fig. 3a (output correlation signal (3)). After such manipulations with the input signal, the SNR is increased up to 10. So it is possible to increase the SNR of input signal of more than 20 dB using proposed method of correlation processing.

Although the device principles of operations are based on the nonlinear interaction, but its output may be linear in a wide range of input signal power. Thus, nonlinear decrease of correlation signal amplitude appears at the pumping power greater than 5,5 W. This effect is related to the spin wave saturation when the evidence of high order nonlinearities appears. This threshold can be regulated by the input signal power and input signal off-duty factor.

Conclusion. In conclusion, we have demonstrated experimentally that using the correlation receiver, shown in Fig.1, based on parametric interaction of spin waves in a ferrite film waveguide it is possible to receive pulsed microwave signals with amplitudes substantially below the noise level and to enhance the signal-to-noise ration in such signals by at least 20 dB. The proposed method of signal extraction from the noise level is enough attractive, because the correlator with only one input antenna can be used.

1. Akhmanov S.A., Dyakov Yu.E., Chirkin A.S. Statistical RadioPhysics and Optics. – M., 1981 (in Russian). 2. Kay S. M. Fundamentals of statistical signal processing. – Boston, 1993. 3. Kobljansky Yu.V., Melkov G.A., Serga A.A., Tiberkevich V.S., Slavin A.N., Effective microwave ferrite convolver using a dielectric resonator // Applied Physics Letters. – 2002. – Vol. 81. 4. Luukkala M., Kino G.S., Convolution and time inversion using parametric interaction of acoustic surface waves // Applied Physics Letters. – 1971. – Vol. 18, No 9. 5. Melkov G.A. et al. Using active delay line for correlation of magnetostatic waves pulses // Proceedings of XVII International Crimea Conference "Microwave & Telecommunication Technology", Sevastopol, Ukraine, 10-14 Sep., 2007. 6. Melkov G.A. et al. Nonresonant wave front reversal of microwave spin waves // Proceedings of 52-nd Annual Conference on Magnetism and Magnetic Materials, Tampa, Florida, USA, 5-9 Nov, 2007. 7. Schulz M., Spin-wave correlator // Journal of Applied Physic. – 1972. – Vol. 43, No 11.

Submitted 19.06.09

TWO-DIMENSIONAL SIMULATION OF DUST CLOUDS IN THE ELECTROSTATIC SHEATH

В роботі представлені результати комп'ютерного моделювання впливу пилового згустку на приелектродний шар. Для визначення параметрів плазми в приелектродному шарі поблизу пилового згустка використовувалась дво-вимірною осе-симетричною гідродинамічною моделлю. Пилова компонента вважалася нерухомою однорідною, зі змінним зарядом. Результати моделювання показують, що іонна густина зменшується всередині пилового згустку і має піки на його границях. Пиловий згусток змінює профіль потенціалу плазми так, що мінімум в розподілі з'являється біля границі пилового згустку з боку плазми. Ця потенціальна яма прискорює іони в напрямку пилового згустку а також є потенціальним бар'єром для негативно заряджених пилових частинок.

Ключові слова: Плазма, моделювання, приелектродний шар, пил, пиловий згусток.

It is carried the computer simulation of the dust cloud influence on the sheath. We used the two-dimensional axially-symmetrical fluid model and self-consistently variable dust charge to study the plasma sheath structure and obtained spatial distributions of plasma parameters in the sheath near the dust cloud. Results show that ion density is increased in the dust cloud and has peaks on the boundaries of the dust cloud. Dust clouds modify potential spatial profiles thus that minimum of electric potential is appeared near the dust cloud boundary from the direction of plasma. This potential drop is accelerate ions toward the dust cloud and it is potential barrier for negative dust particles.

Key words: Plasma, computer simulation, sheath, dust, dust cloud.

Introduction. The problem of the plasma-wall boundary has been known in physics. The specific feature of the non-linear sheath, which is formed near the conducting wall, is the existence of flows of plasma particles towards the wall. Usually the electrodes or walls disturb plasmas far from sheaths creating quasineutral non-uniform plasma regions with slow electric fields and slow gradients of the plasma density which are called presheaths [1, 4]. The presheaths provide boundary conditions for the sheaths and therefore the sheaths have to be considered together with the self-consistent presheaths. In the case of electron-ion collisionless plasma without a magnetic field, the presheath provides the well known Bohm criterion according to which ions have to be accelerated in a presheath to the velocity more or equal to the ion sound speed. In many practical cases, including etching, deposition and sputter plasmas, dust particles have been observed at the plasma-sheath boundary [5, 6]. These microparticles result from sputtering of the electrode and wall surfaces, gas phase nucleation, and polymerization. The observation of the microparticles has shown that those particles are trapped inside the sheath region, close to the plasma-sheath boundary. Dust particles can strongly influence on sheaths [2, 3] due to the selective adsorption of background electrons and ions (penetrating through sheaths) by dust particles. In the result, dust particles create the space electric charge influencing on the sheath structure. In the early studies, most of the plasma sheath models considered that the spatial variation of the sheath takes place in one dimension, usually assuming the underlying electrode to be an infinite plane, so that the sheath profile was uniform in the direction parallel to the electrode. However, such assumptions break down in cases when the dust cloud is formed near the electrode. In such cases, the sheath profile is drastically distorted. Such situations are commonly encountered in plasma-source ion implantation, fabrication of microelectromechanical systems, and in many recent experiments in dusty plasma [7].

In this paper we use the two-dimensional fluid model and self-consistently variable dust charge to study the plasma sheath structure near dust clouds.

Model. We consider a plasma-wall interaction and the sheath forming in presence of a dust cloud. In our model the plasma consist of electrons and ions with densities n_e , n_i . Dust particles are immobile and form a cloud, which is

located at the edge of the sheath. Dust particles are charged after their appearance in the plasma due to the selective collection of electrons and ions so that a change of plasma parameters starts inside the dust layer. This change propagates into plasma due to the self-consistent electric field.

An evolution of the sheath with the dust cloud can be considered in the hydrodynamic approach with the self-consistent electric potential φ described by the following Poisson equation

$$\frac{\partial^2 \varphi}{\partial x^2} + \frac{1}{r} \cdot \frac{\partial}{\partial r} \left(r \cdot \frac{\partial \varphi}{\partial r} \right) = - \frac{e}{\xi_0} \cdot (n_i - n_e - z_d \cdot n_d). \quad (1)$$

The change of the dust charge is described by equation

$$\frac{dq_d}{dt} = I_e + I_i, \quad (2)$$

where electron and ion currents I_e and I_i flowing into dust particle are defined by relations:

$$I_e = -\pi a^2 e \left(\frac{8kT_e}{\pi m_e} \right)^{1/2} n_e \exp \left(\frac{eq_d}{akT_e} \right), \quad (3)$$

$$I_i = \pi a^2 e n_i \left(\frac{8kT_i}{\pi m_i} + v_i^2 \right)^{1/2} \left(1 - \frac{eq_d}{a(kT_i + m_i v_i^2 / 2)} \right). \quad (4)$$

The electrons are assumed to be in thermal equilibrium, therefore the density n_e satisfies the Boltzmann relation

$$n_e = n_0 \exp \left(\frac{e\varphi}{kT_e} \right), \quad (5)$$

where n_0 is the electron (ion) density in unperturbed plasma.

The ions are described by the fluid equations

$$\frac{\partial n_i}{\partial t} + \nabla \cdot (n_i \cdot \vec{w}) = \frac{I_i}{e} n_d, \quad (6)$$

$$\frac{\partial n_i u}{\partial t} + \text{div}(n_i \cdot u \cdot \vec{w}) + \frac{e}{m_i} n_i \frac{\partial \varphi}{\partial r} = 0, \quad (7)$$

$$\frac{\partial n_i v}{\partial t} + \text{div}(n_i \cdot v \cdot \vec{w}) + \frac{e}{m_i} n_i \frac{\partial \varphi}{\partial z} = 0, \quad (8)$$

where \vec{w} , e , m_i are the vector of drift velocity, charge, mass of the ions, u, v are ion velocity components along axes r and z .

Boundary and initial conditions can be written for these equations as:

$$\frac{\partial \phi}{\partial x} = 0, n_i = n_0, v_i = 0 \text{ at } x \rightarrow \infty,$$

$$\frac{\partial \phi}{\partial y} = 0, \frac{\partial v}{\partial y} = 0, \frac{\partial u}{\partial y} = 0, \frac{\partial n_i}{\partial y} = 0 \text{ at } r = 0 \text{ and } r \rightarrow \infty,$$

$$v = 0, u = 0, n_i = n_0, q_d = 0 \text{ at } t = 0.$$

Results and Discussion. Typical results of computer simulations are shown in Fig.1-4. The spatial coordinates r and z are divided here by the initial electron Debye length λ_{d0} , the ion density n_i is divided by the ion concentration in the undisturbed plasma n_0 , the potential ϕ is divided by the characteristic value $\phi_0 = kT_e / e$, the ion drift velocities u, v are divided by the ion sound velocity $c_s = \sqrt{kT_e / m_i}$.

In all variants of calculations dust particles are distributed in the region $12.5 \leq z \leq 17.5, 0 \leq r \leq 10$ uniformly with density n_{d0} .

The influence of dust particles on the sheath illustrates spatial distributions of the electric potential (fig.1). As can be seen, the potential is decreased not only in the region of dust cloud, but near boundaries of the cloud too. The potential profiles along a perpendicular direction to the wall are presented on the fig.1b for $n_d = 0.005$ and $n_d = 0$. We can see that potential is decreased towards the wall monotonically if a dust cloud is absent. At the dust cloud boundaries potential jumps are formed that indicate about appearance of double layers. An electric force in these layers push dust particles if we took account of their movement. Note, the potential changes are different at boundaries of the dust cloud due to an ion flow towards the wall.

Consider potential dependences of radius at different distance from the wall (fig.1c). One can see that the electric potential is changed in area $0 \leq r \leq 10$ before and after the dust cloud, as well as inside the one. It should be noted that potential distribution has oscillations in the dust cloud region in radial direction. This means that there are potential wells for dust particles, which may prevent from the expansion of particles in radial direction. Besides, oscillations of the electric potential indicate the possibility of a plasma-dust crystal formation.

Figure 2 shows ion density as function z in a perpendicular direction to the wall for different values of dust density in the cloud. The dotted line corresponds to the case without dust particles.

We can see that in cloud region the ion density is been increased at the dust density increasing. Besides, it is observed the ion density increasing in the region between the wall and the dust cloud in the case $n_d = 0.01$, as well as ion density peaks are appeared at dust cloud boundaries.

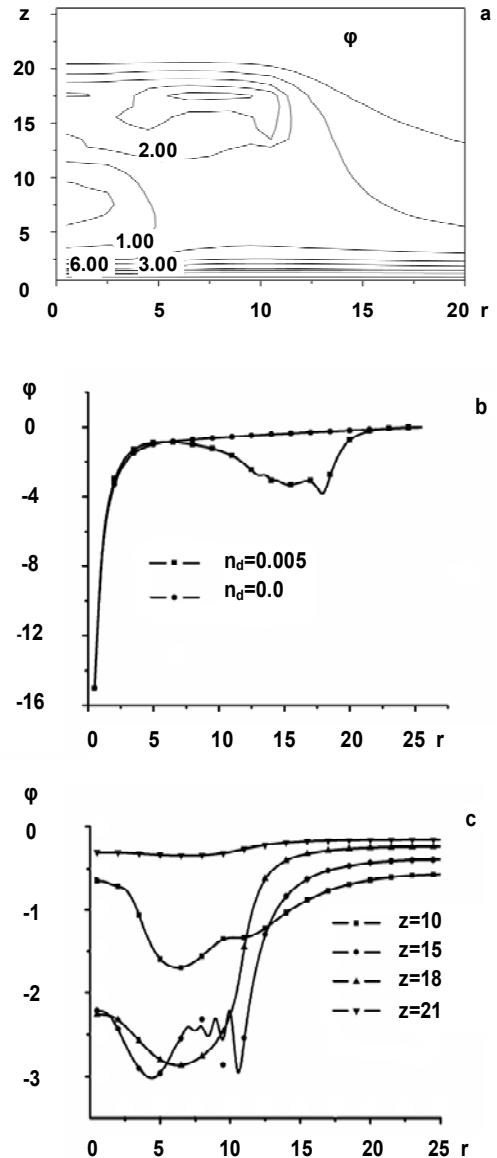


Fig. 1. The potential distribution in the sheath near the dust cloud at $n_d = 0.005$ (a), potential distributions along the perpendicular direction to the wall at $n_d = 0.01$ (b), potential distributions along axis r at different z at $n_d = 0.01$ (c)

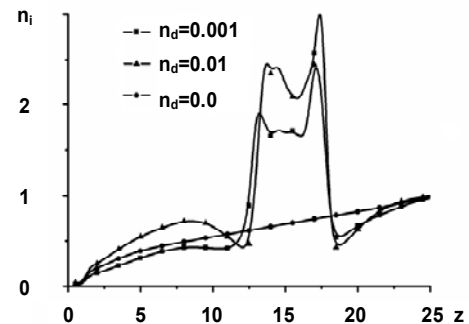


Fig. 2. The spatial distribution of the ion density along the perpendicular direction to the wall through the cloud

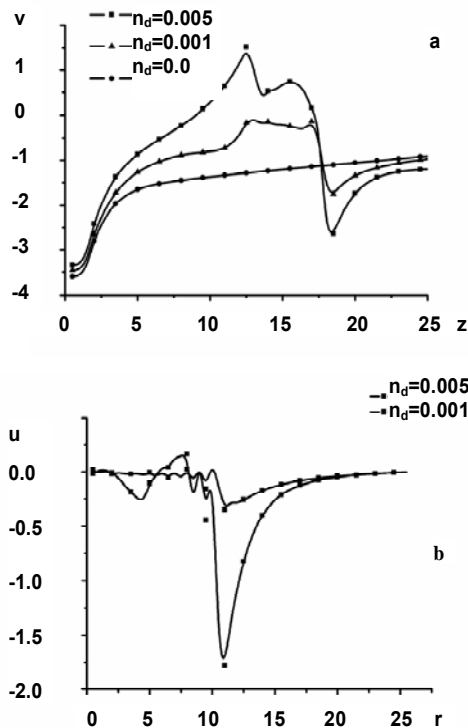


Fig. 3. Spatial distributions of the ion velocity along axe z (a), spatial distributions of the ion velocity along axe r (b)

Spatial distributions of the ion velocity are shown in fig.3. We can see that ions are accelerated on all the way to the wall in the case without a dust cloud. While the ion drift velocity is changed significantly at the boundaries of the dust cloud. It is observed an essential acceleration of

УДК 533.9

ions to dust cloud boundaries which is associated with an electric field in double layers. Despite the strong disturbance of potential near the dust cloud the ion velocities at the wall are almost identical in all calculations.

Note, that the ion flow is formed in radial direction to the dust cloud. At the cloud boundary an ion velocity depends of a dust density. The ion flow is subsonic at $n_d = 0.001$ and the one is supersonic at $n_d = 0.005$. In the latter case oscillations are appeared in distributions of plasma parameters. This may be due to the drift instability in plasma.

Conclusions. Two-dimension computer simulations have been performed to investigate the dust cloud near the plasma-sheath boundary.

We obtained spatial distributions of plasma parameters in the sheath near the dust cloud. Results show that ion density is increased in the dust cloud and has peaks on the boundaries of dust cloud. Dust clouds modify potential spatial profiles thus that minimum of electric potential is appeared near the dust cloud boundary from the direction of plasma. This potential drop is accelerate ions toward the dust cloud and it is potential barrier for negative dust particles.

1. Cipolla W., Silevitch M.B. On the temporal development of a plasma sheath // Plasma Physics. 1981. – V.25, N.6.
2. Chutov Yu., Kravchenko O., Schram P., Yakovetsky V. Non-linear sheaths with dust particles // Physica. – 1999. – V. B262, N.3-4.
3. Jin-Xiu Ma, M.Y.Yu. Electrostatic sheath at the boundary of a dusty plasma // Phys. Plasmas. – 1995. V.2, N.4.
4. Riemann K.U. The Bohm criterion and sheath formation // J. Phys. D: Appl. Phys. -1991. – V. 24, N.4.
5. Selwyn G. S., Singh J., Bennett R. S. In situ laser diagnostic studies of plasma-generated particulate contamination // J. Vac. Sci. Technol. – V. 7, N.4.
6. Spears K.G., Kampf R.P., Robinson T.J. Particle densities in radio-frequency discharges of silane // J. Phys. Chem. – 1988. – V.92. N. 5. – P.5297-5302.
7. Thomas E. Potential profiles obtained from applied dust cloud perturbations //Physics of plasmas. – 2002. – V.9, N.1.

Submitted 19.10.09

O. Kravchenko, Ph. D., O. Pyankova, master

SIMULATION OF UNIPOLAR ARC FORMATION IN SHEATH BETWEEN PLASMA AND ISOLATED WALLS

Проведено двохвимірне моделювання еволюції приелектродного шару, що виникає між плазмою та ізольованою стінкою, під впливом вибухової емісії електронів з мікроплями поверхні, використовуючи PIC/MCC метод. Приведено розрахунки для різних значень густини електронного струму та тиску.

Отримано ефект того, що під дією вибухової емісії електричне поле поблизу центру емісії змінює свій знак. За рахунок цього ефекту продемонстровано виникнення уніполярної дуги.

Ключові слова: приелектродний шар, уніполярна дуга, вибухова емісія електронів, метод частинок в комірках, метод Монте-Карло.

It is carried the two-dimensional computer simulation of evolution of the sheath that arises between plasma and isolated wall under the influence of an explosive emission of electrons from the microspot of the surface using the PIC/MCC method. Calculations are performed for different electron current densities and gas pressures.

One of the obtained effects is the direction changing of the electric field under the influence of explosive emission near the center of the electrons emission. Due to this effect the unipolar arc ignition is shown.

Key words: sheath, unipolar arc, explosive emission of electron, particle-in-cell method, Monte-Carlo method.

Introduction. Plasma is separated from the plasma reactor's walls by a space charge sheath (Langmuir–Debye sheath) because of the mobility difference between ions and electrons. The phenomena in sheath play a considerable role in the various plasma technologies of solid surfaces processing and controlled thermonuclear power production. Due to essentially nonlinear character of the sheath it seems topical to study its properties by means of the computer modeling.

One of the most interesting phenomena bound up with the sheath is formation of an unipolar arc. According to

modern representations unipolar arcs cause the reactor's walls corruption. Particularly, the unipolar arc is the emission source of heavy ions which are sources of the increased Bremsstrahlung radiation losses of energy.

Essential for this kind of discharges is that single electrode serves as both the cathode and the anode. The cathode is the region of the explosive electron emission; the anode is ring-like area surrounding the cathode. Explosive electron emission can appear on some cathode surface defects and is caused by the increased electric fields near them, followed by the thermal and secondary

electron emission. In some conditions, that should be determined, the return flow of electrons appears around the emitting spot. This return flow closes the current loop of the unipolar arc.

Most of qualitative theoretical unipolar arc models are based on the Bohm sheath theory [2]. According to this theory, if the metal plate placed into the plasma doesn't let out any charged particles (there are no emission centers on its surface), the balance of electronic and ionic currents from plasma is set.

The plate accepts floating potential which shields the plate from all electrons except the high-energy ones in Maxwell distribution. The value of the floating potential satisfies the relation:

$$V_f \gg \frac{T_e}{2e} \ln \left(\frac{m_i}{2m_e} \right)$$

e , m_e are electron charge and mass, respectively, m_i is plasma ions mass, T_e is electron temperature of plasma in energy units. If there is an electron emission centre on a plate, the value of the plate potential should be defined taking into account the emission current J_{em} and plate square S according to the following expression:

$$V_f^* \gg \frac{T_e}{e} \ln \left(\frac{en_e u_e S}{J_{em}} + en_i u_i S \right).$$

A circulating current that appears between plasma and plate is called an unipolar arc: "hot" electrons from plasma overcome detaining potential V_f^* , transfer current on a plate, and from a plate "cold" emitted electrons transfer a current to plasma. The value of the circulating current is possible to estimate by the following equation:

$$\begin{aligned} J_c &= j_e - j_i = eS \left(n_e u_e \exp \left(-\frac{V_f^*}{T_e} \right) - n_i u_i \right) = \\ &= en_e \left(\frac{T_e}{2m_e} \right)^{1/2} \left(\exp \left(-\frac{V_f^*}{T_e} \right) - \exp \left(-\frac{V_f}{T_e} \right) \right) \end{aligned}$$

Numerical experiments of the explosive emission influence on the sheath were carried by the Gielen G., Shram D. [1] and Roshansky V. et al [3]. Both scientists' groups carried out the calculations within the hydrodynamic plasma description in the presence of a magnetic field, but a electron friction with neutral atoms were neglected. Hydrodynamic models assume Maxwellian velocity distribution, but its justice needs to be proven under the conditions of the explosive emission.

But mentioned and other [4] theoretical and numerical models are just qualitative, and there are no detailed theory based on self-consistent model.

In this article we present simulation results of the sheath evolution under the influence of the explosive emission near a wall at a floating potential.

Model. A two-dimensional model of sheath is considered. One boundary of modeling area is a wall at a floating potential. The ion flow with directed Bohm velocity and the thermal electron flow are defined at the opposite boundary. The area between boundaries is filled with the argon plasma. It is supposed that electrons and ions recombine on the wall. The secondary electron emission with coefficient $\gamma = 0.3$ is taken into account.

The high-density electron flow is defined from central small area of wall ($0.0049 \text{ m} \leq y \leq 0.0051 \text{ m}$) to take into consideration the explosive electron emission.

Simulations were made by means of Particle-in-Cell and Monte-Carlo methods [5] to take into an account in our code the following reactions caused by electron and ion impacts:

- elastic electron-neutral collisions

$$Ar + e^- \rightarrow Ar + e^-;$$
- elastic ion-neutral collisions

$$Ar + Ar^+ \rightarrow Ar + Ar^+;$$
- ionization

$$Ar + e^- \rightarrow Ar^+ + 2e^-;$$
- neutral excitation by electron heat

$$Ar + e^- \rightarrow Ar^* + e^-;$$
- charge exchange between ions and atoms

$$Ar + Ar^+ \rightarrow Ar^+ + Ar.$$

Following parameters of the unperturbed plasma were used: electron and ion densities $n_{e,i} = 10^{15} \text{ m}^{-3}$, electron temperature $T_e = 2.5 \text{ eV}$, ion temperature $T_i = 0.03 \text{ eV}$. The explosive emission current density varies within $j_e = 10^3 - 10^5 \text{ A/m}^2$. In our case, the value of wall potential has been set $V_{fl} = 5 \text{ B}$ approximately corresponding to the floating wall potential for plasma, thus electronic and ionic streams on a wall are approximately equal. The width of the sheath is around $d = 0.1 \text{ cm}$.

Results and Discussion. The spatial potential distribution is shown on fig.1a for the case $j_e = 10^5 \text{ A/m}^2$. We can see that the electron emission essentially influences the potential of the electric self-consistent field in the sheath. The potential minimum is formed in front of the emission spot and the sheath width is greatly increased. The potential profiles along a perpendicular direction to the wall for different emission current densities are presented on the fig.1b. The solid line corresponds to the case without emission. Dotted, dashed and stroke dashed lines correspond to emission current densities $j_e = 10^3 \text{ A/m}^2$, $j_e = 10^4 \text{ A/m}^2$ and $j_e = 10^5 \text{ A/m}^2$ respectively.

These profiles are similar to potential profiles in the vacuum diode when the thermo- or autoelectronic emission is present. It is significant that the potential minimum is being increased when the electron current density from the wall is increasing.

In the sheath the electric field is directed only to a wall if an electron emission is absent. In this case ions are accelerated toward the wall and electrons are pushed away from the wall. In cases with an electron emission the potential falling near emission area, the formation of potential minimum, and its increase with a smaller gradient is being observed. The potential profile deformation brings to appearance of positive electric field in the vicinity of the emission region due to the electron emission. There is no formation of a dense plasma cloud over emission area, as ionization almost does not occur.

On fig. 2 the spatial allocation of an electric field vector near the emission spot is represented in case when the emission current density is $j_e = 10^3 \text{ A/m}^2$.

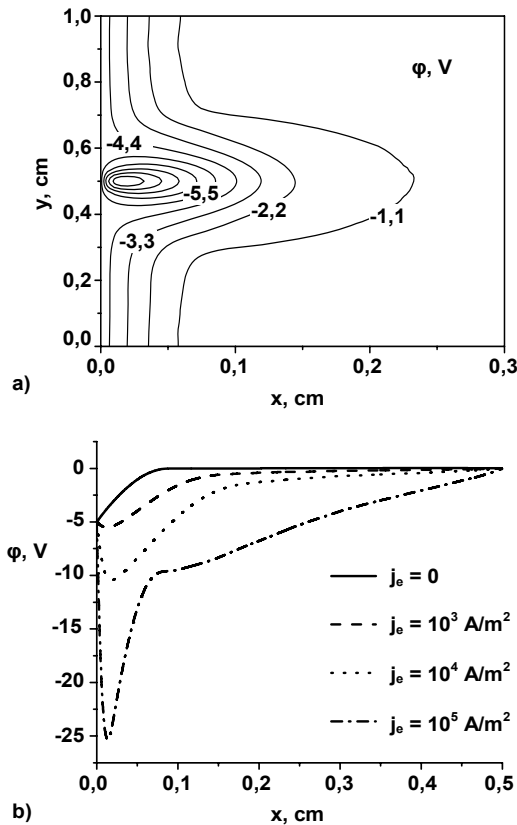


Fig. 1. The potential distribution near the emission centre

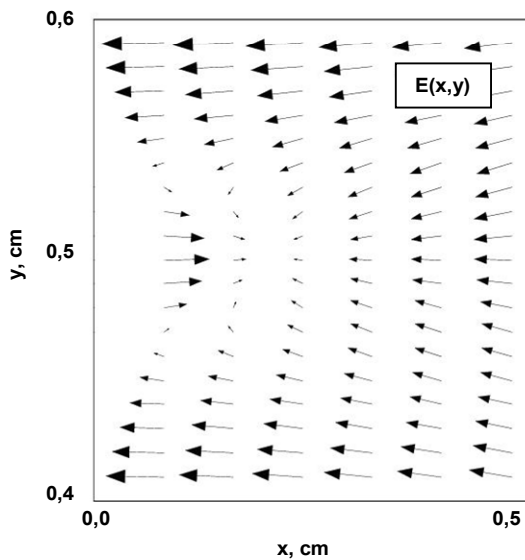


Fig. 2. The spatial distribution of the vector electric field in the case of the electron emission current $j_e = 10^3 \text{ A/m}^2$

It is obvious that electric field changes its direction in the area of width around 0.6 mm near the emission spot. This area is three times wider than the area of the emission spot. This result suggests that electrons move to the wall in the vicinity of the emission spot, i.e. the electron return current appears. This confirms fig.3, where distributions of current density to the wall are shown along the wall at different values of electron emission current densities. For comparison the current densities are normalized by the value of electron emission current density. The positive current peak corresponds to the emission current from the wall. It can be observed as the current density is negative in the vicinity of the

emission spot. It indicates that electrons move to the wall in this area. The current density value is being increased when the electron emission is increasing.

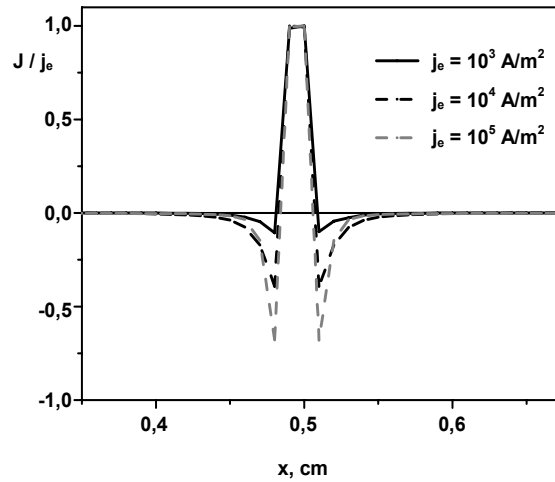


Fig. 3. Dependence of the current density on the coordinates y along the wall

It is visible that return current density on a wall has the same order, as a current which flows from the emission spot in case when $j_e = 10^5 \text{ A/m}^2$. On the basis of this result it is possible to confirm that the unipolar arc ignites in this case.

In order to confirm this fact we will consider the spatial distribution of macroelectrons (fig.4) in case when $j_e = 10^5 \text{ A/m}^2$. It can be seen from this figure that the areas of higher density of electrons are formed. The first one is located near the emission spot ($x = 0, 0.0049 \text{ m} \leq y \leq 0.0051 \text{ m}$) and is caused by the electron emission flow from the wall. The second one is arched form and located at the distance around 1 mm from the emission centre. The increase of electron density in front of the emission spot ($0.0075 \text{ m} \leq y \leq 0.001 \text{ m}$) is caused by a neutral gas ionization in this location, as electrons gain sufficient energy accelerated in the electric field. The electron movement is defined by the allocation of the electric field vector (fig.2). The analysis of macroelectron positions shows that they move to the wall mainly through the arched channel. Consequently, the electron density is increased in this channel. In fact, we have received the illustration of the unipolar arc formation based on self-consistent model.

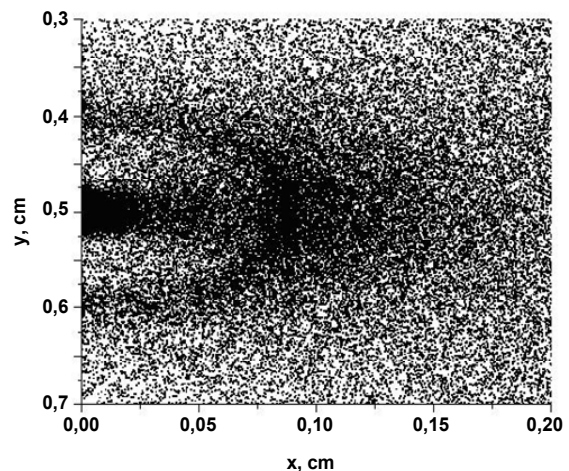


Fig. 4. Space distribution of macroelectrons at current density of explosive emission $j_e = 10^5 \text{ A/m}^2$

Conclusions. This article presents computer simulations of unipolar arc phenomena in the frame of a self-consistent physical model. The potential distribution near the surface emitting was calculated. It was shown that the region of the return current, where the potential is significantly perturbed with respect to the floating one, is much larger than the emitting channel width. When the reduced potential in front of the emitting surface is larger than the cathode voltage drop of the arc and the return current exceeds the minimal current typical for the arc, then ignition of the arc is possible. In our case the unipolar arc is ignited at a current density of emission more than 10^5 A/m².

UDC 621.317.2

O. Lushkin, Ph.D., V. Shcherban, stud.,
S. Teslenko, stud.

DEVELOPMENT OF AN AUTOMATED MEASURING UNIT FOR AUGER SPECTROMETER 09IOS-3

Проведено аналіз вимог до блоку спряження оже-спектрометра типу 09IOC-3 з персональним комп'ютером (ПК) з метою суттєвого прискорення швидкості реєстрації оже-спектрів. Обрано елементну базу, а також інтерфейс для зв'язку цього блоку з ПК. Розроблено схему блоку на основі мікроконтролера ATmega8 фірми ATMEL, "прошивку" для нього та програмне забезпечення для ПК. Результати контрольних вимірювань, проведених створеним блоком, свідчать про те, що блок не спотворює данні, які надходять з блоку реєстрації оже-спектрометра.

Ключові слова: автоматизація, оже-спектроскопія, вимірювальні прилади.

The analysis of requirements for the unit to conjugate Auger spectrometer 09IOS-3 with a personal computer (PC) to increase the rate of registration Auger spectra was made. Components and interface to connect the unit to a PC were selected. A block scheme was developed (on the basis of ATmega8 microcontroller), firmware for it and software for the PC. Results of control measurements for the developed unit indicate that the unit does not distort the data coming from registration unit of Auger spectrometer.

Key words: automatization, auger spectroscopy, measuring device.

A boule of lithium niobate (LiNbO₃), which is widely used in optical and acoustic electronics as waveguides deflectors, modulators of laser radiation in optical data recording devices is an interesting object for research. At this time, many phenomena that occur on the surface of the crystal under the influence of external factors, are unclear. Therefore, researching LiNbO₃ is of considerable scientific interest.

According to a high level of modern computer technology, the complexity of the information processing obtained as a result of studies using Auger spectrometer, and keen interest in the transient processes on the lithium-niobate caused by temperature changes or the influence of external electric field, there is a need to create device which will automate the research, providing high-speed recording of Auger spectra (tens volt per second) and a greater resistance to distortion and noise. Therefore, the aim of this work was to develop a conjugation block between the PC and Auger spectrometer 09IOS-3.

Introduction. Analog recorder is usually used to record the spectrum. It is connected to the rate unit and registration unit. However, this method has several disadvantages associated, first, with analog recorder inertia, second, with noises of the registration and amplifier units [2]. Overall, this leads to impossibility of Auger spectrum recording without distortion at rate greater than 2 volt per second (spectrum is recorded in 5-6 minutes). At the same time, study of fast processes on the surface of LiNbO₃ after effects of an electric field requires a much faster method of the spectrum recording.

The main ideas in automation of electronic spectrometer are in control and data recording using a PC. As industrial Auger spectrometer 09IOS-3 has no standard interface to exchange information with PCs, a conjugative unit is required.

There are several similar devices in other research laboratories, but they are not fast enough, have the external power source and are plugged to the PC through outdated currently interfaces. In addition, the development of its own device has a purely technical interest and provides the opportunity to improve not only the block conjugate components, but also a method of measurement.

1. Gielen H.G., Schram D.C. Unipolar Arc Model // IEEE Trans. Plasma Sci. – 1990. – Vol.18, №.1.
2. Robson A.E., Thonemann P.C. An arc maintained on an isolated metal plate exposed to a plasma // Proc. Phys. Soc. – 1959. – № 73.
3. Rozhanskij V.A., Ushakov A.A., Voskobojnikov S.P. Electric field near an emitting surface and unipolar arc formation // Nuclear Fusion. – 1996. – Vol.36, №.2.
4. Schwirzke F., Hallal M.P., Maruyama X.K. Onset of breakdown and formation of cathode spots // IEEE Trans. Plasma Sci. – 1993. – Vol. 21, № 5.
5. Vahedi V., DiPeso G., Birdsall C.K., Liemberman M.A., Rognlien T.D. Capacitive RF discharges modeled by particle-in cell Monte Carlo simulation. I: analysis of numerical techniques // Plasma Sources Sci. technol. – 1993. – Vol.2, №.4.

Submitted 18.10.09

Among all the possible options of information exchange between device and PC serial USB interface is the most acceptable (due to its wide spread occurrence, high data transfer rates and availability of bus power) [3].

An automated operation with Auger spectrometer requires sending commands and synchronization signals to scan unit, getting the analog signal in the range +5 ÷ -5 volts from registration unit. These signals have to be converted into digital code, and transferred to a PC.

Scheme development. The selected automation scheme is based on the programmable microcontroller ATmega8 [1]. It exchanges information with a PC via USB port using a transmission standard RS-232 [4]. Power for the device comes directly from the USB bus, which provides a simple and mobile system.

Features of ATmega8 by AVR [6]:

- High-performance, Low-power AVR® 8-bit Microcontroller
- Advanced RISC Architecture
 - 130 Powerful Instructions – Most Single-clock Cycle Execution
 - 32 x 8 General Purpose Working Registers
 - Fully Static Operation
 - Up to 16 MIPS Throughput at 16 MHz
 - On-chip 2-cycle Multiplier
- Nonvolatile Program and Data Memories
 - 8K Bytes of In-System Self-Programmable Flash
 - Endurance: 10,000 Write/Erase Cycles
 - Optional Boot Code Section with Independent Lock Bits
 - In-System Programming by On-chip Boot Program
 - True Read-While-Write Operation
 - 512 Bytes EEPROM
 - Endurance: 100,000 Write/Erase Cycles
 - 1K Byte Internal SRAM
 - Programming Lock for Software Security
- Peripheral Features
 - Two 8-bit Timer/Counters with Separate Prescaler, one Compare Mode

- One 16-bit Timer/Counter with Separate Prescaler, Compare Mode, and Capture Mode
- Real Time Counter with Separate Oscillator
- Three PWM Channels
- 8-channel ADC in TQFP and MLF package
- Six Channels 10-bit Accuracy
- Two Channels 8-bit Accuracy
- 6-channel ADC in PDIP package
- Four Channels 10-bit Accuracy
- Two Channels 8-bit Accuracy
- Byte-oriented Two-wire Serial Interface
- Programmable Serial USART
- Master/Slave SPI Serial Interface
- Programmable Watchdog Timer with Separate On-chip Oscillator
- On-chip Analog Comparator
- Special Microcontroller Features
- Power-on Reset and Programmable Brown-out Detection
- Internal Calibrated RC Oscillator
- External and Internal Interrupt Sources
- Five Sleep Modes: Idle, ADC Noise Reduction, Power-save, Power-down, and Standby
- I/O and Packages
- 23 Programmable I/O Lines
- 28-lead PDIP, 32-lead TQFP, and 32-pad MLF
- Operating Voltages
- 4.5 – 5.5V (ATmega8)
- Speed Grades
- 0 – 16 MHz (ATmega8)
- Power Consumption at 4 Mhz, 3V, 25°C
- Active: 3.6 mA
- Idle Mode: 1.0 mA
- Power-down Mode: 0.5 µA
- The main reasons for choosing the microcontroller are:
- Imbedded 10-bit ADC
- ADC conversion in ADC noise reduction mode
- Data transfer using USART
- Low price of the device

Signal with amplitude deviation in 10 V (-5 ÷ 5 V) comes from Auger spectrometer registration unit to the input line of device. It's scaled and shifted by AD8542 operational amplifiers to the range 0 ÷ 5 V (input range in microcontroller's ADC).

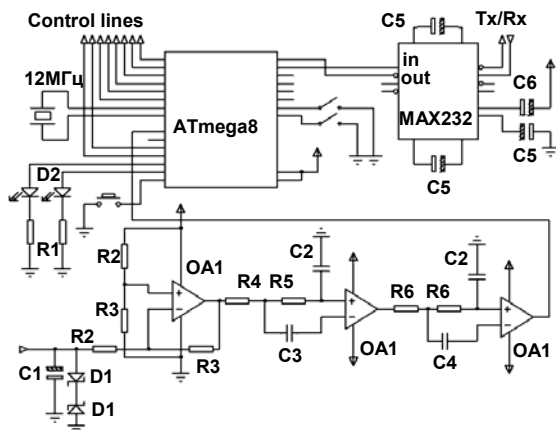


Fig. 1. Scheme of conjugative unit. Pins of ATmega8 up to down left to right: 14-19, 9, 10, 23-28, 1; 2-6, 11-13, 20, and 21. Control lines: NORMAL, HSPEED, DOWN, UP, RESET, STOP, START, Fosc. OA1 – AD8542; D1 – 1.5KE6V8CA; D2 – led; R1 – 300; R2 – 40k; R3 – 20k; R4 – 619k; R5 – 649k; R6 – 1.37m; C1 – 0.1µ; C2 – 12n; C3 – 82n; C4 – 15n; C5 – 1µ; C6 – 100n

Then the signal passes through the fourth order active filter to the two operational amplifiers AD8542 (Fcut = 6Hz;

attenuation of -22 dB on Fnoise = 15Hz [5]) and comes to the microcontroller's 10-bit ADC0 (Fig.1).

MAX232 chip enables signal level conversion from TTL (0 ÷ 5 V) to +/- 12 V used in COM port, providing the opportunity to connect the device directly to PC through COM port. FD232 chip provides data transfer via USB (Fig.2).

Table 1. Control lines

Signal	Spectrometer connector	Pin
START	BC	6
STOP	BC	7
RESET	BC	8
UP	BC	4
DOWN	BC	5
HSPEED	BC	2
NORMAL	BC	3
Fosc	BKY	20

Lines of control are plugged to Auger spectrometer according to the table 1.

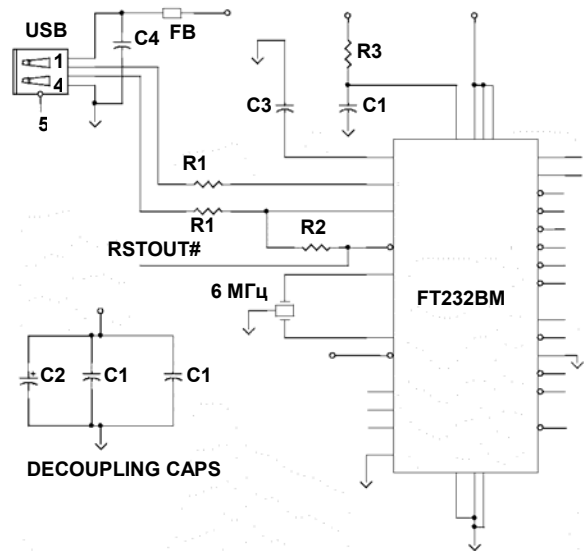


Fig. 2. Scheme of FT232BM plugged to USB. FT232BM pins counter-clockwise starting from top left: 6, 8, 7, 5, 27, 28, 4, 32, 1, 2, 31, 29, 9, 17, 10-12, 14-16, 18-25, 13, 26, 3, 30. FB – ferrite bead, R1 – 27, R2 – 1.5k, R3 – 470, C1 – 0.1µ, C2 – 10µ, C3 – 33n, C4 – 10n

Working principle. The conjugative unit works in the following way: it receives information about experiment settings (step voltage between measurements, the minimum and maximum voltage, the number of measurements at one point and time delay between measurements) and awaits for the command to start an experiment.

Upon receiving appropriate instruction microcontroller begins an experiment activating signal RESET (on the rate unit). After that signal START is given. Then the following steps are made:

- a specified number of ADC (voltage measurement) at the point performed, average value of the signal calculated;
- the result is transmitted to the PC via USART;
- sending to the Fosc pin corresponding number of pulses with a frequency of 1 MHz (100 pulses corresponds to the energy of 0.1 eV) voltage step on the rate unit is made;
- pause is made to reach corresponding time between measurements.

When the measurements are over, signal STOP is sent to the rate unit and the PC receives notification about the end of the experiment.

It should be noted that during the conversion of analog signal microcontroller is directed to "low noise" state to reduce the digital noise generated by the microcontroller in the process of ADC. Microcontroller firmware was written in high-level programming language C, using the compiler CodeVision of AVR. Convenient user interface written in Visual C++.

Results and discussion. Firstly were made design and calculation of the scheme. Then firmware for microcontroller ATmega8 was created. Completed verification test of developed firmware in simulator VMLab, found errors and inaccuracies corrected code. Made an assembly of elements and microcontroller firmware flashed using programming kit Kanda Systems STK 200, manufactured in advance, and firmware instrument Code Vision AVR. Device was plugged to the rate and registration units of Auger electron spectrometer O9IOS-3, connected to the PC.

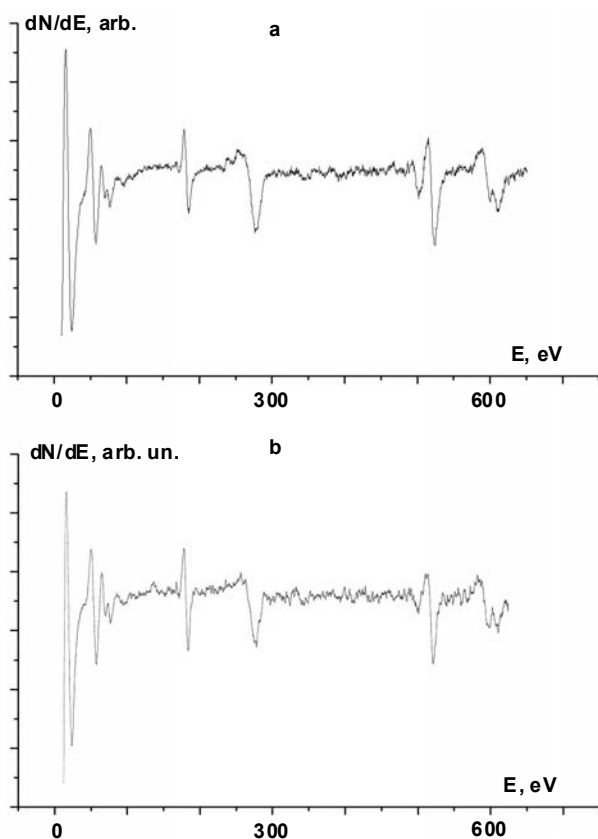


Fig. 3. Auger spectrum of scandium cathode:
a) wrote using conjugative unit at recording speed 20 V/sec;
b) wrote using analog recorder at recording speed 2 V/sec

The first verification test of the connected system was made in a "safe" mode with high voltage turned off and registration unit disconnected. Second verification test was made with already included units. Both checks were successful, so the next step was recording of Auger spectrum.

Samples for test spectra recording were selected so that the result can be easily compared with previously processed

data. Thus this allowed to test not only working unit, but that the recorded spectra correspond previous results.

The first sample was scandium cathode. Spectrum was recorded with a conjugation block at rate 20 V/s (Fig.3 a) and the results compared with the spectrum obtained with analog recorder at rate 2 V/s (Fig.3 b). Considering the results, we can make conclusion about their identity.

We can see that the noises of the both spectra are almost the same. In addition, the ratio of amplitudes of Auger peaks of barium and other components to the amplitude of Auger peak oxygen coincide with accuracy to 1/10, while the speed rate is increased 10 times.

The second tested sample was niobium crystal with adsorbed chlorine on its surface. Auger spectra recorded at rate 20 V/sec (Fig. 4) again verified that the data obtained using a conjugate device quite match the results obtained previously using the analog recorder.

In addition, Auger spectra are easy to analyze and can be processed by modern software packages (eg, Origin, Exel).

After reviewing the Auger spectra obtained at different rate (2, 5, 10, 20, 50 V/s), it must be noted that the best ratio recording speed / spectrum distortion amplitudes achieved with rate 20 volts per second.

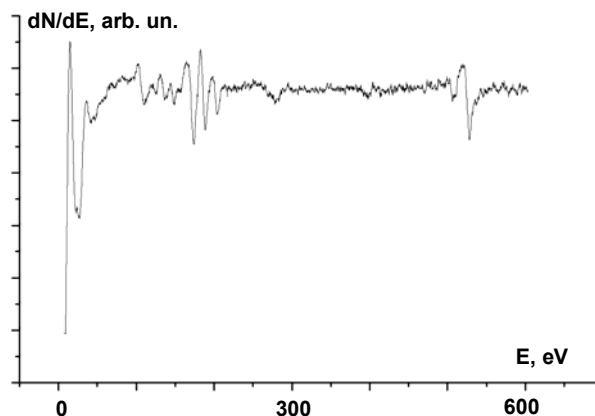


Fig. 4. Auger spectrum of niobium crystal with adsorbed chlorine on its surface recorded at rate 20 V/sec

Conclusions. Auger spectra of control samples were received using automated measuring to verify its efficiency. Analysis has shown that developed device does not distort the signals coming from Auger spectrometer registration unit even at rate 20 V/sec. This is 10 times faster then in O9IOS-3 spectrometer normal mode and allows exploring the fleeting processes on the surface of solids.

1. Баранов В.Н. Применение микроконтроллеров AVR: схемы, алгоритмы, программы. – М., 2004.
2. Козлов И.Г. Современные проблемы электронной спектроскопии. – М., 1978.
3. Новиков Ю.В., Калашников О.А. Разработка устройств сопряжения для персонального компьютера типа IBM PC. Под общей редакцией Новикова Ю.В.. Практ. Пособие. – М., 1998.
4. Трамперт В. Измерение, управление и регулировка с помощью AVR-микроконтроллеров. Пер. с нем. – К. 2006.
5. Угрюмов Е.П. Цифровая схемотехника: Учеб. Пособие для вузов. – 2-е изд., перераб. и доп. – СПб., 2004.
6. WWW.ATMEL.COM

Submitted 23.10.09

UDC 537.634

L. Masluk, stud., M. Matsishin, stud.,
M. Petrychuk, senior researcher, V. Kovalenko, prof.**FETURES OF MAGNETIC NANOPARTICLES INTERACTION ON SMALL DISTANCES**

Often magnetic liquid contains clusters of a few or more particles in condensed liquid phase, and also in a solid phase In case of interaction between nanoparticles on distances, considerably smaller than their sizes point dipoles is rough. The most suitable and adequately close to the reality in this case is a spherical model. It bases on the calculation of ball-shaped particles interaction as a sum of interaction between plenty enough their fragments. In this work a spherical model and point dipole model are compared and the limits of application are determined for each of them.

Keywords: nanoparticle, cluster, magnetic interaction.

Часто магнітна рідина містить кластери із декількох або більшої кількості частинок в концентрованій рідкій фазі, а також в твердій фазі. В разі взаємодії між наночастинками на відстанях, значно менших, ніж їх розмір, наближення точкових диполів являється досить грубим. Найбільш відповідною і адекватно близькою до дійсності в даному випадку є сферична модель. Вона базується на обчисленні взаємодії сферичних частинок як суми взаємодій між фрагментами, які повністю їх заповнюють. У цій роботі співставлені сферична модель і модель точкових диполів, а також визначені межі застосування кожної з них.

Ключові слова: наночастинка, кластер, магнітна взаємодія.

Introduction. Magnetic liquids are colloid solutions of small magnetic particles in a liquid-carrier. Particles hold back from sinking in due to small dimensions and interaction with the thermal vibrations of molecules of the liquid. Prevalence of particles kinetic energy over potential energy is necessary for this purpose. The critical size of nanoparticles calculated under this condition is approximately 10 nm [4].

Another condition of magnetic liquid existence as colloid solution is a requirement of absence of particles association in clusters as a result of dipole-dipole interaction or Van der Waals forces. This condition is more rigid and can't be taken off by the simple diminishing of particles size. An artificial method is used to exclude coupling forces – coverage of particles by the layer of nonmagnetic hydrophobic material. Usually this material is olein acid, which, for example, is provided to the magnetic liquid on the basis of kerosene as a transmitter and Fe₃O₄ on the stage of chemical synthesis.

A magnetic liquid with fully dissociated particles is not the unique possible variant of the nanoparticles system distributed in space. Often it contains clusters of a few or more particles as the condensed liquid phase [6], and also as a solid phase (so called "hard clusters") [1]. Theoretical ground of that or other type of clusters existence and magnetic liquid on the whole needs calculation methods of interaction between nanoparticles on distances, considerably smaller than their sizes. In this case an approach of the point dipole [1] that is usually used in calculations rough. Condition of point dipole fitting reality is a considerable exceeding of the distance between dipoles over the dipole length.

It is known that for clusters structure description, except for the point dipole model exists spherical [3], hexagonal [5], cylinder [2] and other models. The most suitable and adequately close to the reality is the spherical model. It bases on the calculation of interaction between ball-shaped particles as a sum of interactions between plenty enough their fragments. The fragments of interactive spherical particles are considered to be point dipole.

In this work a spherical model and point dipole model are compared and the limits of application are determined for each of them.

For the point dipole model energy of interaction between two dipoles with the magnetic moments m_1 and m_2 is determined as:

$$V_{12} = \frac{m_1 m_2}{|R_{12}|^3} - \frac{3(m_1 R_{12})(m_2 R_{21})}{|R_{12}|^5}, \quad (1)$$

where R_{12} and R_{21} – radius-vectors of distance between point dipoles [1].

The calculation has been conducted numerically.

A spherical model is described by the next list of properties.

1. A sphere parts on fragments.
2. Vectors of fragments magnetic moments have an identical value (except for surface fragments) and parallel between itself.
3. The value of fragment magnetic moment is proportional to its volume.
4. There is no deformation of spherical particles in the process of their interaction.

Choice of optimum quantity of particle laying out on fragments in calculations computation

The numeral calculation of spherical particles interaction energy has been conducted by calculation of total energy of fragments interaction between itself. The result depended on quantity of the fragments, namely: expected energy of interaction especially at small distances gradually diminished at the increase of fragments quantity, and monotonously approached to the defined asymptotic value, which was considered as . Obviously that number of fragments needs to be increased for diminishing of the error, however the expenses of machine time grow substantially with the increasing of fragments number. Therefore, it is needed to choose the optimum value of fragments number. On Fig.1 shown the expected dependence of energy from distance between interactive particles for two values of fragments quantity.

The analysis of data on Fig.1 shows that on distance between particles that is equal 1.05 of a double radius, there is divergence between the energy for 3375 and 8000 fragments, at a greater distance curves coincide. At the diameter of particles of 20 nm it corresponds distance between the surfaces of spherical particles of 1 nm, that is approximately equal the thickness of anticoagulant layer, that is smaller then minimum distance between particles in the real magnetic liquid. Thus optimum number of laying out fragments for a spherical particle isn't more than 3375. Future calculations are conducted with such particles laying out on fragments.

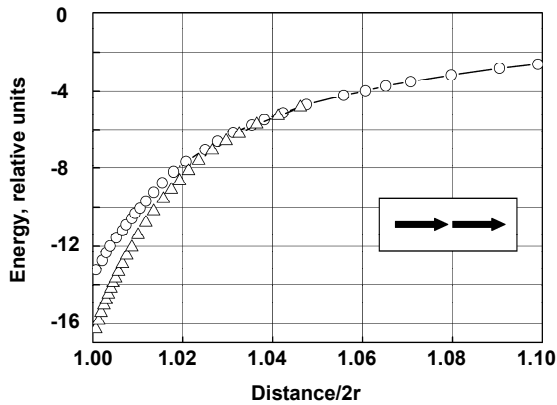


Fig. 1. Dependence of energy on distance between interacting spherical particles rationed on a double radius of a aid out into 3375 fragments (circles) and 8000 fragments (triangles). Configuration of interactive magnetic dipoles is on an inset

Calculation of particles interaction energy dependence on distance between them.

We analyzed the limits of fitness of point dipole model with respect to the spherical particles model in dependence on distance between particles. Configuration magnetic moments mutual orientation is the same as in previous calculation. The results of calculation are shown on Fig.2.

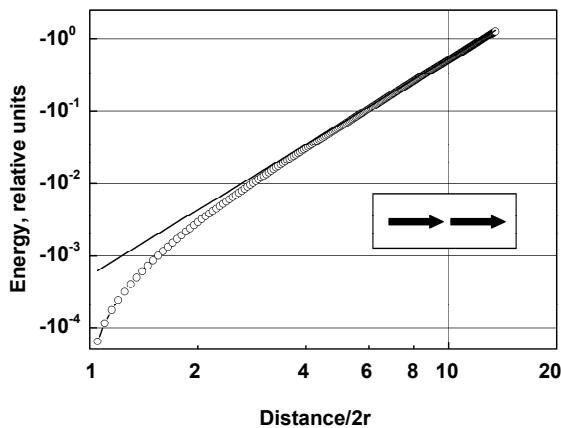


Fig. 2. Dependence of the spherical particles interaction energy from distance between particles rationed on a double radius of a particle. Continuous line corresponds point dipole model, opened circles correspond the spherical model

Minimum distance for which energy of interaction has been calculated is 1.05 diameters of a particle. On this distance the calculation of interaction energy for a spherical model gave a result, smaller on an order, than for the point dipole model. Difference diminishes with the increase of distance, and at distance 8 diameters of particle, it makes only 5%. This result shows limits of application of the point dipole model and also it shows presence of strong interaction between particles on small distances between them.

There is angular dependence of particles interaction energy. Configuration of interactive particles and magnetic moments at their parallel position is shown on Fig.3, and on Fig.4 we see angular dependence of interaction energy at distance between particles at of 1.1 their diameter.

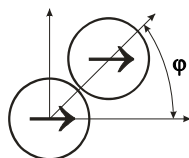


Fig. 3. Spherical particles orientation in the cylinder system of coordinates

It is characteristically, that, as evidently on Fig.4, energy of the mutual attracting between particles in the network of spherical model is substantially less than in point dipole model in all of range of angular positions as expected (see Fig.2). I a g difference is at placing of the particles in a row ($\phi = 0, \pi$).

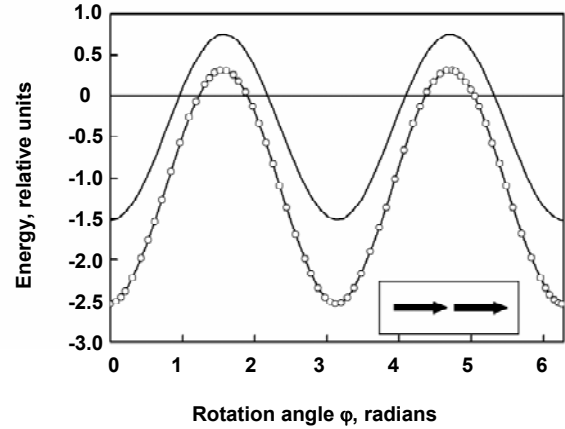


Fig. 4. Dependence of the spherical particles interaction energy on the rotation angle of one particle in relation to other. Continuous line corresponds point dipole model, opened circles – spherical model

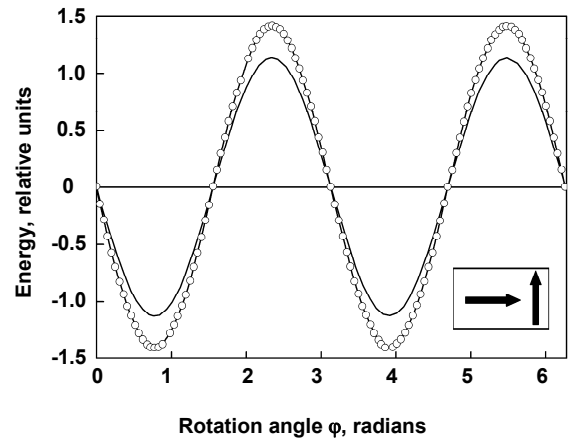


Fig. 5. Dependence of the spherical particles interaction energy on the rotation angle of one particle in relation to the other at mutually perpendicular position of magnetic moments. Continuous line corresponds point dipole model, opened circles – spherical model

On Fig.5 we have shown calculations for mutually perpendicular magnetic moments position of particles at distance between particles of 1.1 their diameters. Here the extremum values also are bigger for a spherical model. Thus, our calculation in accordance with the point dipole model shows that in case of mechanical contact between magnetic particles the magnetic interaction between particles is substantially underestimated.

1. Антонюк О.А., Коваленко В.Ф., Молдован Б.М., Петричук М.В. Голчасті магнітні кластери і їх поведінка в магнітному полі// Укр. фіз. журн. – 2004. – Т. 49. №12. 2. Beleggia M., Tandon S., Zhu Y., De Graef M. On the magnetostatic interactions between nanoparticles of arbitrary shape // J. Magnetism and Magnetic Materials. – 2004. – Vol. 278. 3. Duncan P., Camp P. Structure and dynamics in a monolayer of dipolar spheres // J. of chemical physics. – 2004. – Vol.8, №12. 4. Rosensweig R.E. Ferrohydrodynamic, Dover Publications, Incorporated, New York, 350 p. 5. Spoliansky D., Ponsinet V., Ferr J., Jamet J.-P. Magneto-optical study of the orientation con_nement of particles in ferrolyotropic systems // Eur. Phys. J. (E 1). – 2000. – Vol.227 (235). 6. Падалка В.В. Взаимодействие коллоидных магнитных частиц с электрическими и магнитными полями: дис. докт. физ.-мат. наук. – Ставрополь, 2004.

Наукове видання



ВІСНИК

КИЇВСЬКОГО НАЦІОНАЛЬНОГО УНІВЕРСИТЕТУ ІМЕНІ ТАРАСА ШЕВЧЕНКА

**РАДІОФІЗИКА
ТА ЕЛЕКТРОНІКА**

Випуск 13

Друкується за авторською редакцією

Оригінал-макет виготовлено Видавничо-поліграфічним центром "Київський університет"

Автори опублікованих матеріалів несуть повну відповідальність за підбір, точність наведених фактів, цитат, економіко-статистичних даних, власних імен та інших відомостей. Редколегія залишає за собою право скорочувати та редагувати подані матеріали. Рукописи та дискети не повертаються.



Підписано до друку 05.02.10. Формат 60x84^{1/8}. Вид. № 155. Гарнітура Arial. Папір офсетний.
Друк офсетний. Наклад 500. Ум. друк. арк. 7,2. Обл.-вид. арк. 10,0. Зам. № 210-5133.

Видавничо-поліграфічний центр "Київський університет"

01601, Київ, б-р Т. Шевченка, 14, кімн. 43

☎ (38044) 239 32 22; (38044) 239 31 72; (38044) 239 31 58; факс (38044) 239 31 28